COMPUTATIONAL STUDY OF PROTON-DISORDERED ICE IH

by

Xun Wang

B.S., China Pharmaceutical University, 2010

Submitted to the Graduate Faculty of

The Dietrich School of Arts and Science in partial fulfillment

of the requirements for the degree of

Doctor of Philosophy

University of Pittsburgh

2016

UNIVERSITY OF PITTSBURGH
THE DIETRICH SCHOOL OF ARTS AND SCIENCE

This dissertation was presented

by

Xun Wang

It was defended on

August 1st, 2016

and approved by

Daniel S. Lambrecht, Assistant Professor, Department of Chemistry

Sean A. Garrett-Roe, Assistant Professor, Department of Chemistry

John A. Keith, Assistant Professor, Department of Chemical Engineering

Dissertation Advisor: Kenneth D. Jordan, Professor, Department of Chemistry

COMPUTATIONAL STUDY OF PROTON-DISORDERED ICE IH

Xun Wang, PhD

University of Pittsburgh, 2016

Water is the most important liquid on the earth, yet the physics behind many properties of water is still poorly understood. Particular interesting are the condensed phases of water: ice and liquid water, that both possess anomalous properties. In this thesis, I focus on using different methods, including force fields as well as DFT calculations, to predict several key properties of proton-disordered ice Ih and liquid water.

The focus of my study of ice Ih is on its comparable dielectric constant ε_s with liquid water, which directly results from its proton-disorder nature. Predictions of the dielectric constant of ice Ih from pairwise additive force fields fall appreciably below than the experimental values, with significant improvement being achieved by polarizable force fields. I examined the performance of different force fields, and confirmed that the polarizable AMOEBA models with three polarizable sites per molecule[1] outperform polarizable models such as DC97 with a single polarizable site[2].

Since it is difficult to resolve the subtle energetic difference of different proton ordering arrangements in ice Ih with force fields, I studied the energetics of ice Ih, from DFT calculations using the BLYP functional as well as several dispersion-corrected BLYP functionals. As shown in my study, the dispersion-corrected functionals not only give better energy predictions but also get better lattice parameters and equilibrium volumes for the optimized ice Ih unit cells.

I also predicted the structural as well as dynamical properties of liquid water from *ab initio* molecular dynamics simulations with several dispersion-corrected BLYP functionals. The results of calculations all confirmed that including dispersion corrections in functionals is essential to get faster water rotational dynamics and a "softer" structure of liquid water.

Finally I parametrized a two-channel dispersion-corrected atom-centered pseudopotential (DCACP2) based on the BLYP functional to correct for the long-range dispersion force for three rare gas elements: helium, neon and argon. By fitting the interaction energy of three homonuclear dimers against CCSD(T) calculations, the resulting DCACP2-BLYP method performs significantly better than the one-channel DCACP approach for the two-body binding energies of the dimers. I also explore the factor responsible for the success of DCACP2 method.

TABLE OF CONTENTS

LIST OF TABLES

LIST OF FIGURES

LIST OF EQUATIONS

PREFACE

First of all, I am indebted to my Ph.D. advisor, Dr. Ken Jordan, for giving me the opportunity here to pursue my Ph.D. degree in theoretical chemistry in his research group over the past five years. It was extremely fortunate for me to have such an advisor, who taught me so much in every aspect of science. Ken's knowledge, insight, enthusiasm and serious attitude in science always motivated me to achieve better success and make faster progress. Ken taught me how to approach and solve a challenging scientific problem with his great kindness and patience. I always enjoyed the discussions with Ken, and felt inspired and encouraged each time. Ken was also giving me a lot of helpful advice and ideas on my independent proposal. Besides being my research advisor, Ken's integrity personality has influenced and will always influence me for the rest of my life.

I am grateful to Dr. Daniel Lambrecht, Dr. Sean Garrett-Roe, and Dr. John Keith for serving on my dissertation committee, spending time carefully reading my dissertation, and all of the help and assistance they have given to me over the years.

I would also like to thank the current and former staff in chemistry department at University of Pittsburgh, especially Mr. Jay Auses, Ms. Fran Nagy, Ms. Christie Hay, for all the help they provided during my graduate study at Pitt.

I would like to thank the computing resources provided by the Center for Simulation and Modeling (SAM), and current and former SAM faculties especially Dr. Akila Gothandaraman,

Dr. Kim Wong and Dr. Albert Defusco for providing constant, helpful, and on-time technical solutions.

I am grateful to former Jordan group colleagues for the helpful discussions about my projects at the beginning of my graduate study: Dr. Eric Kratz, Dr. Vamsee Voora, Dr. Zach Pozun, Dr. Ozan Karalti, Dr. Meysam Makaremi, Xiaoge Su, Dr. Guozhen Zhang, Dr. Jiawei Xu, Dr. Fangfang Wang, Dr. Wendy Lampart and Dr. Mary Shermann, as well as the current Jordan group members Togo, Kaye, Kevin, Abhijeet and Arailym.

I would like to thank all the friends I made at Pitt, for all the fun we had together, and my best friend Qianhui at Minnesota, for her help and suggestions in my graduate studies and life.

I would like to say special thanks to my boyfriend Victor. Whenever I felt frustrated in research or life, he was always there patiently listening to my gabbling and accompanying me and encouraging me to walk through the difficulties.

Also, I am grateful to my aunt Mrs. Huiqiu Wang, for her encouragement in my life.

Last but not the least, I would like to thank my parents Mr. Peng Wang and Mrs. Wei Shi who brought me to the world and allow me to explore anything that I found interesting. Without their constant financial and emotional support over these 29 years, I would never have been achieved so far. Thanks, mom and dad! This dissertation is dedicated to you!

1.0 INTRODUCTION

1.1 PROTON ORDERING IN DIFFERENT PHASES OF ICE

Water is one of the most special and widely studied substances in nature. While its properties have been widely investigated, its fundamental structure is still poorly understood theoretically. At low temperatures, water freezes into different forms of ice, with the polymorphism of which revealed by its rich phase diagram in **Figure 1.1**[3].

Figure 1.1 The phase diagram of liquid water and ice[3].

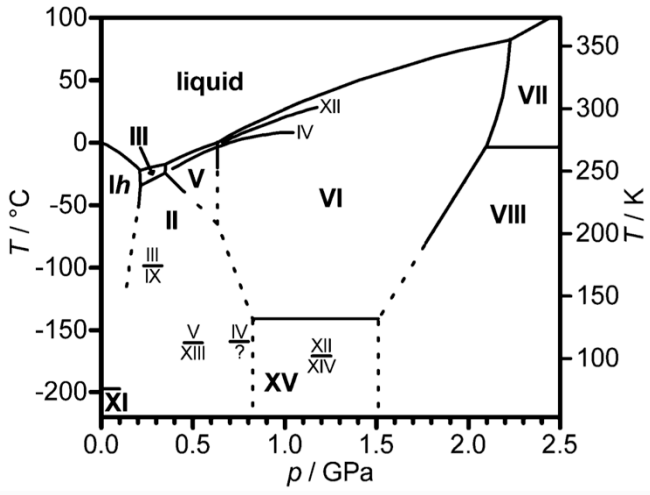

Some of the phases of ice are proton-ordered, with the infinite hydrogen-bonded crystal structure just being the replication of a single unit cell, which only involves one certain pattern of hydrogen bonds, such ice XI, ice IX or ice VIII. The positions of hydrogen atoms in the other phases of ice, however, can adopt different positions, as long as the "Bernal-Fowler" ice rules[4]

are satisfied, leading to an orientation disordered structure overall. **Figure 1.2** displays the possible orientations of a water molecule in a tetrahedral ice lattice.

Figure 1.2 The six possible orientation of water molecule in a tetrahedral ice lattice.

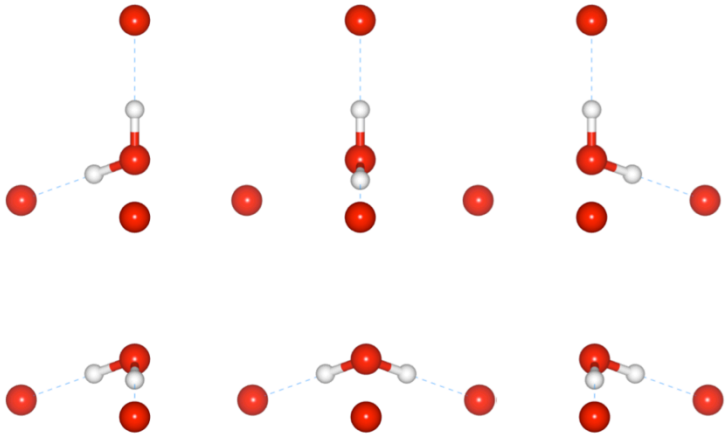

Since each single molecule can take one of six orientations, and according to Pauling[5], there is 25% chance that the adjacent molecules will permit this orientation, hence there are $(\frac{6}{4})^N$ ways of arranging N molecules. Therefore, the molar entropy S of proton-disordered ice at 0 K is given by,

$$S = RlnW = NRln\frac{3}{2} \qquad \text{Equation 1.1}$$

where R is the molar gas constant and W is the number of ways of arranging the molecules. Pauling

assumed these configurations would all be degenerate at low temperatures, and that all configurations contribute equally to the entropy. However, different proton orderings in fact differ in energy, making some configurations more favorable than others. Since the energy differences between proton ordered structures with the same underlying oxygen lattice can be small on an absolute scale, but large with respect to k_BT, their resolution requires the application of accurate modeling techniques. To date, there is a considerable body of computational work on

proton ordering in the bulk hexagonal ice Ih, as well as the other important phases of ice. I will elaborate more on the energetic study of phases of ice in chapter 3.

1.2 WHY STUDY ICE IH?

Among the fifteen different phases of ice, the most important and common one is the ordinary ice, or ice Ih, with *h* denoting the symmetry of its unit cell. The crystal structure of ice Ih is displayed in **Figure 1.3**. Each oxygen atom forms two covalent bonds and with two hydrogen atoms, and also form two hydrogen bonds with two hydrogens from neighboring water molecules.

Figure 1.3 The crystal structure of ice Ih[3b].

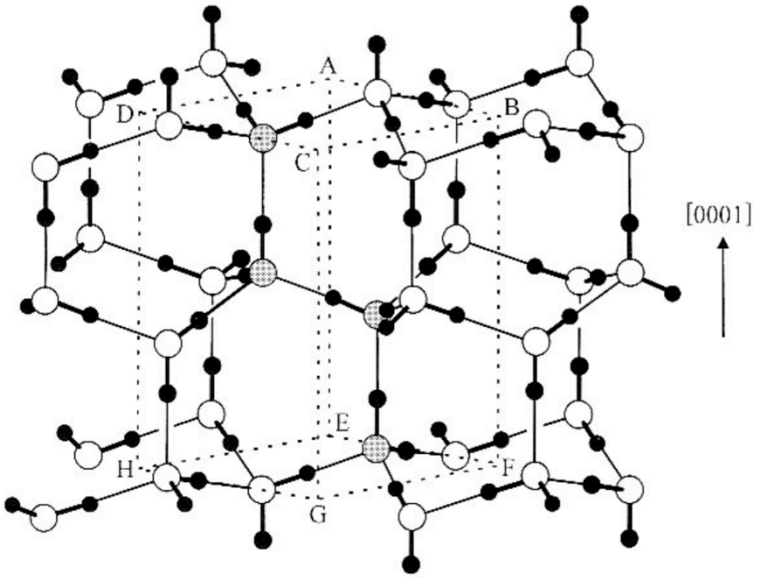

There are three main motivations for my study of proton-disordered ice Ih:

1) Ice Ih possesses several abnormal structural and thermal properties, such as the high dielectric constant at all temperatures compared to its proton-ordered counterparts[6].

The proton disorder of ice is responsible for its distinctive properties, and many of them such as the high dielectric constant ε_s, the anomalous volume isotope effects (VIE) are still not understood well from the theoretical viewpoint. The predictions of ε_s of ice Ih using different non-polarizable water models in previous studies (**Table 2.1**) are about 50% below experimental values.

2) The difficulty to model the proton hopping at low temperature (below 72K) for the disorder-order transition from Ih to XI calls for special techniques to sample ergodic phase space.

A glass transition occurs at around 100-110 K, diminishing the proton mobility and locking protons in their disordered positions, before they re-orient to form the proton-ordered ice XI structure. Doping ice Ih with KOH can overcome this issue, due to the formation of two types of proton defects, which are in very low concentrations in real ice. Protons rearrange in ice through mechanisms involving low-concentration orientational defects (the Bjerrum D and L defects[7]) and ionic defects. System sizes that are amenable to computer simulations generally do not include such defects. Also, the time scale for proton reorientation is much longer than what is possible in standard molecular dynamic simulations. At temperatures under 100K, the proton reorientation takes place on the millisecond time scale. Special techniques have been introduced to deal with this issue. The most common strategy is to use a Monte-Carlo technique that first identifies a hydrogen-bonded loop and then collectively shifts the hydrogens along the loop. The other approach is the electrostatic switching molecular dynamics (MD) procedure developed by Lindberg and Wang[8], which is adopted in our work.

3) Previous theoretical studies led to a large dispersion of relative energies and structural properties of the different proton order patterns.

A large literature is devoted to the study of the proton disorder and ordering in hexagonal ice, discussing the following two issues: i) the ordering nature in the low temperature phase, i.e. whether the ferroelectric or anti-ferroelectric ordered phase is more stable; ii) the theoretical prediction of the phase transition temperature from ice Ih to ice XI. Commonly used two-body force field models such as the TIP4P[9] variants and SPC/E[10] were shown to be unable for predicting the correct energetics ordering of proton ordering in ice, while a modified polarizable force field KW-pol model was successful in favoring ferroelectric ordering over disordered structure, which implies the importance of incorporating polarizability into the empirical force field for capturing the subtle energy difference between different proton configurations.

2.0 DIELECTRIC CONSTANT OF PROTON-DISORDERED ICE IH FROM MOLECULAR DYANMICS SIMULATIONS

2.1 INTRODUCTION

2.1.1 Overview of proton disorder and ε_s of ice Ih

The proton disorder of ice Ih is responsible for its distinctive dielectric constant ε_s, that is associated with the fluctuations of the dipole moment in the system. Surprisingly, ε_s of liquid water at T = 278 K (86) is close to that of ice Ih at the melting point T = 273 K is 96[11]. The experimental ε_s vs. T curve of ε_s of ice Ih is nearly a continuation of that of liquid water, as displayed in **Figure 2.1**.

Figure 2.1 The experimental curve of ε_s of proton-disordered ice Ih and liquid water.

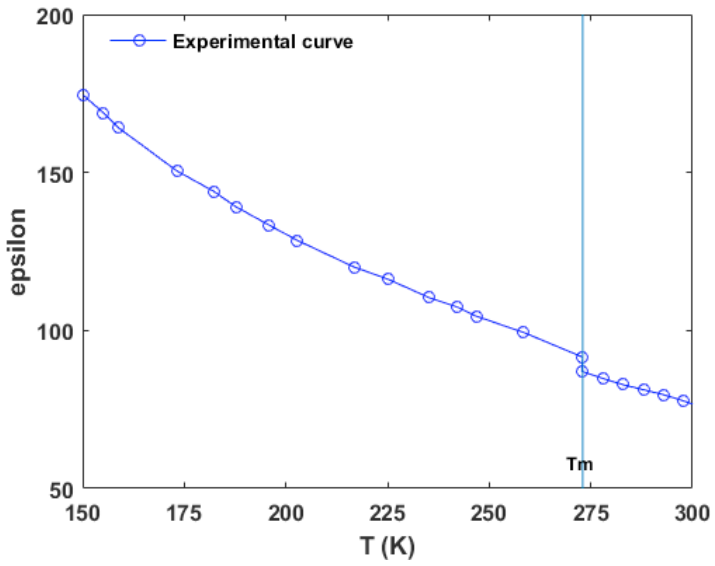

Debye explained the high dielectric constant of ice Ih in terms of monomer electric dipoles, that at equilibrium reorient under thermal movement[12]. Due to the existence of two types of defects in ice as shown in **Figure 2.2**, dipole reorientations in ice Ih are possible.

Figure 2.2 Two types of defects in ice Ih structure: a) orientational defects; b) ionic defects.

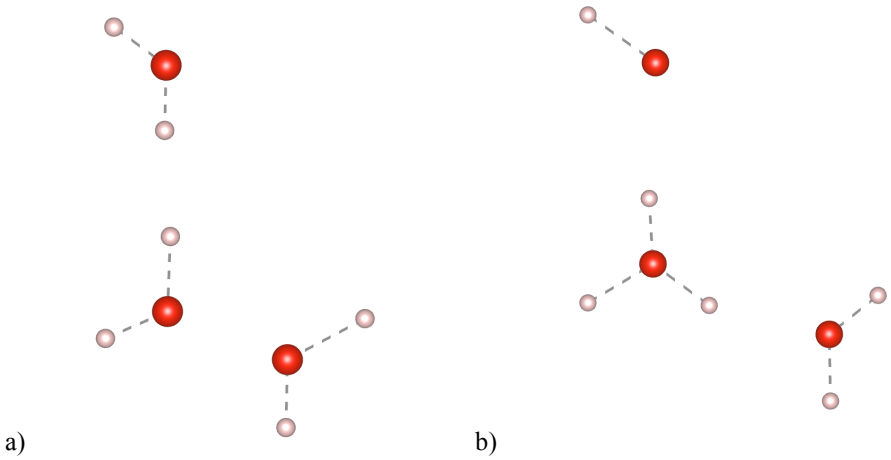

These dipole turns either 1) do not change the total system dipole, by turning all hydrogen bonds in a "closed loop" made of six water molecules (as displayed in Figure 2.3(a)) along the same direction; or 2) make a net change to the total dipole in the system by turning all hydrogen bonds crossing the periodic boundary in a simulation cell for computer simulations, which is represented as a "percolating loop" (as displayed in Figure 2.3(b)). However, the extreme low concentration of such defects make these proton reorientations hard to observe in simulation cells with sizes permitted by computer simulations. Also, the time scale for proton reorientation is much longer than that for standard molecular dynamic simulations. At temperatures under 100K, the proton reorientation takes place on the millisecond time scale[13]. Therefore, several techniques have been introduced to deal with this issue in computational studies, including the symmetry-based graph invariant algorithm sampling[14], the electrostatic switching MD procedure of Wang and coworkers[8], as well as several Monte-Carlo algorithms that incorporate the cooperative hydrogen bond moves[15].

Figure 2.3 A 2D-picture of ice-Ih structure with an intra-layer closed loop and percolating loop.

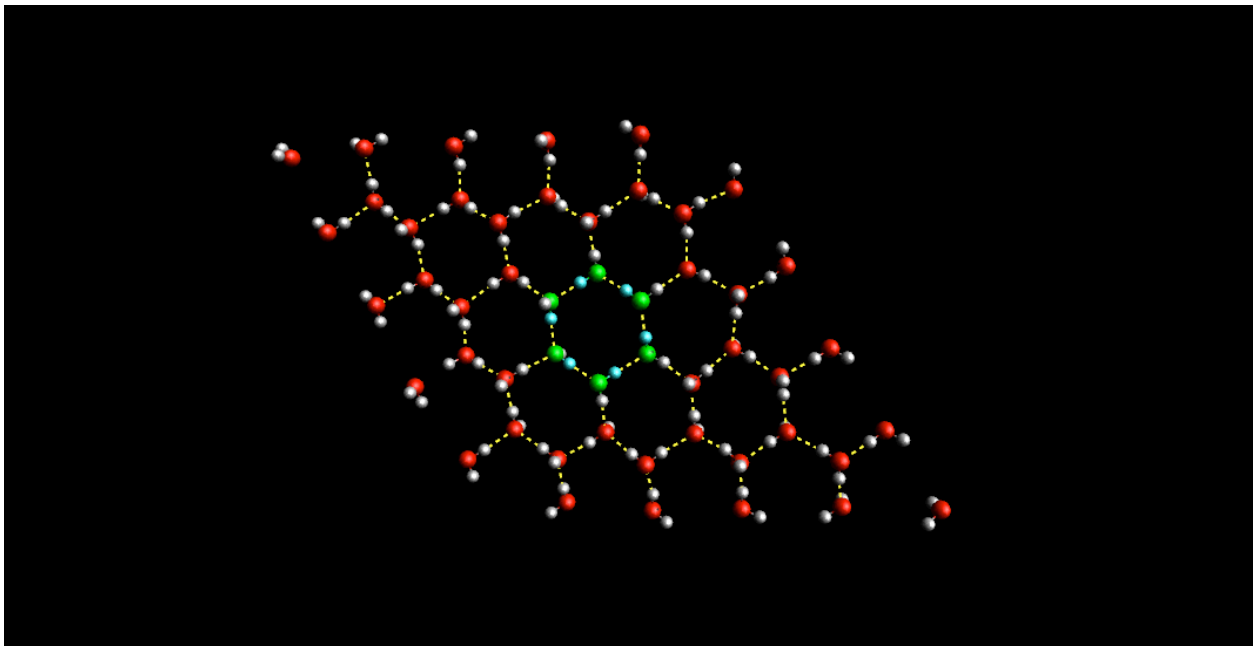

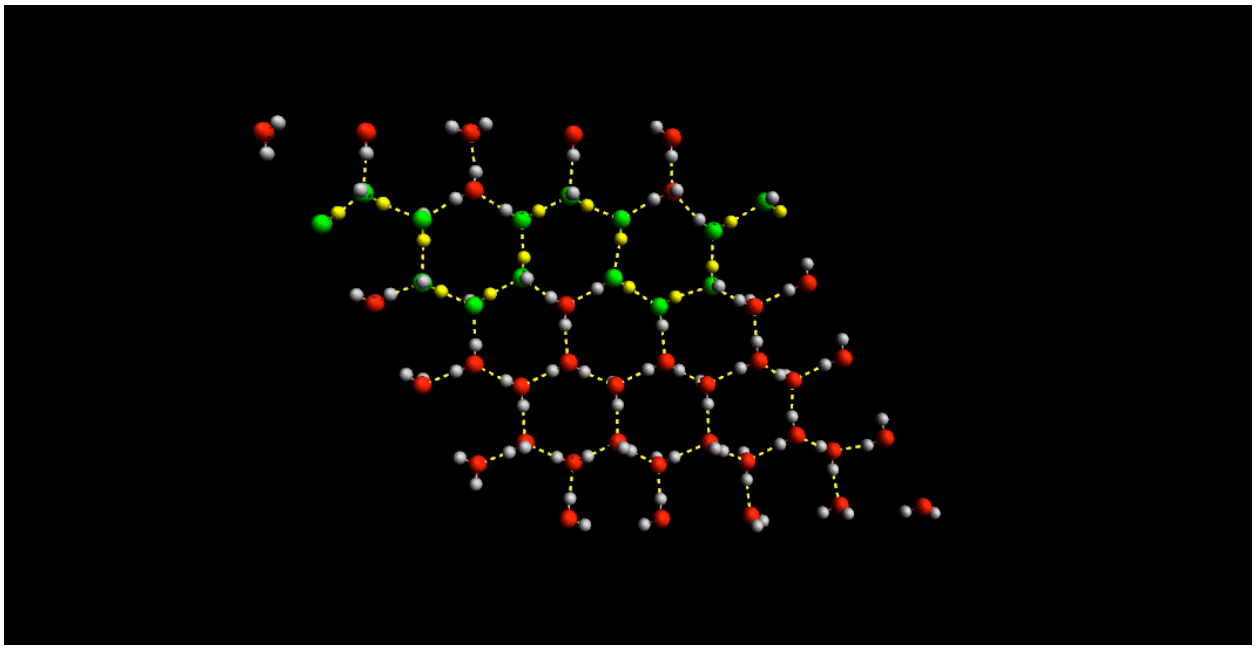

2.1.2 Calculation of ε_s

To determine dielectric constant ε_s from computer simulations, the following well-known fluctuation relation is used:

$$\varepsilon_s\text{-}\varepsilon_\infty = \frac{4\pi}{3k_BTV}\left(\langle\vec{M}^2\rangle\text{-}\langle\vec{M}\rangle\cdot\langle\vec{M}\rangle\right) \approx \frac{4\pi}{3k_BTV}\langle\vec{M}\cdot\vec{M}\rangle \qquad \text{Equation 2.1}$$

where ε_∞ is the high-frequency dielectric constant usually taken to be 1, k_B is the Boltzmann constant, T is temperature in Kelvin, V is the volume for the simulation system, and $\vec{M}$ is the polarization vector of the system defined as $\vec{M} = \sum_{i=1}^{N}\vec{\mu}_i$, and the angular brackets denote an ensemble average over independent configurations. By defining a polarization factor $G = \frac{\langle(\sum_{i=1}^{N}\vec{u}_i)^2\rangle}{N}$, where $\vec{u}_i$ is the unit vector along the direction of the dipole moment of each molecule in ice Ih, can be reduced to:

$$\varepsilon_s\text{-}\varepsilon_\infty = \frac{4\pi}{3k_BTV}(\langle(|\vec{\mu}_i|\text{-}\langle|\vec{\mu}|\rangle)^2\rangle + \langle|\vec{\mu}|\rangle^2 G) \qquad \text{Equation 2.2}$$

Based on the equations above, there are two factors that affect the result of calculated ε_s:

1) The *G* factor, that describes the relative orientations of dipole moments in the simulation system, which arises from the sampled equilibrated structures of proton-disordered ice Ih.
2) The magnitude of the molecular dipole moment $|\mu_i|$**,** as predicted by the computational method.

2.1.3 Motivation of this work

The initial motivation for this study was that the theoretical predictions of ε_s of ice Ih from pairwise additive non-polarizable force fields fall appreciably lower than the experimental curve, with improved results obtained with polarizable force fields. However, the failure of non-polarizable force fields were not found in the prediction of ε_s of liquid water[8] and of clathrate hydrates[16]. By including polarization explicitly in the force field as in polarizable force fields, the prediction of ε_s of ice Ih were much better in reproducing the experimental curve over temperatures. Therefore, we were motivated to examine the polarizable force fields in the prediction of ε_s of ice Ih.

The results of previous calculations of ε_s of ice Ih are summarized in **Table 2.1**. As demonstrated from the representative work using SPC/E[10] and TIP4P[9] models by Vega[16-17], Wang[8], and Rick[15a, 18], these models underestimate the ε_s of ice Ih by ~50% compared with the experimental values. Increasing the number of charged sites in a water model even worsens the results, as shown in the study from TIP5P model by Rick[18]. Noticeable are the values achieved by Laury and coworkers using the reparametrized AMOEBA model in 2014[1] (denoted as

AMOEBA14 model throughout this study). Skinner and coworkers used their E3B three-body potential and predicted the ε_s of ice Ih[19] in good reproduction of the experimental curve. Their calculation was based on the fitting the dipole of water in ice Ih to the experimental curve of ε_s of ice Ih. Recently, Liu and coworkers employed an *ab initio* dipole-moment-surface (DMS) from the Bowman group[20] together with the E3B potential, and obtained a good reproduction of the ε_s of ice Ih compared with experimental values over a range of temperature. The prediction of ε_s of ice Ih serves as a good test of a force field.

The dielectric constant of ice Ih has also been calculated by DFT methods. In 2012, Wang and coworkers calculated ε_s of ice Ih used projector-augmented-wave based PBE functional and sampled the ice Ih structures from the modified electrostatic switching procedure[21]. However, their study underestimated the ε_s of ice Ih and liquid water by about 35%[21]. They obtained the dipole moment for ice Ih of 2.5 Debye/monomer, compared with the value of 3.09 Debye from the self-consistent induction model[22]. In 2014, VandeVondele and coworkers calculated the dielectric anisotropy of ice Ih using several hybrid and semilocal density functionals and a Monte-Carlo sampling scheme[23]. Their study over-estimated the ε_s of ice Ih by 20 % - 40 % over temperatures.

Recently, the effect of nuclear quantum fluctuations to ε_s of ice Ih has been studied by Moreira and Koning[24] using DFT-based path integral[25] simulations, with the conclusion that both the hydrogen bond network in ice Ih, which is characterized by the *G* factor in Equation 2.2 and the molecular dipole moment $|\mu_i|$, are sensitive to protonic quantum fluctuations, and the average molecular dipole moment was increased by 5%, probably due to the elongation of the O-H bond in the quantum simulations.

Table 2.1 Representative results of static dielectric constant of ice Ih in as obtained from different models.

Model	Author	T(K)	ε_s
TIP4P[15a]	Rick, Haymet (2003)	240	48(1)
TIP4P[19]	Vega, MacDowell (2010)	240	47(1)
TIP4P[8]	F. Wang, Lindberg (2008)	240	51(1)
TIP4P/2005[16]	Vega, MacDowell (2010)	240	53
TIP4P/2005	Vega, Aragones (2011)	243	53(2)
TIP4P/Ice[16]	Vega, MacDowell (2010)	240	57
TIP5P[18]	Rick (2005)	240	30(3)
TIP5P[17]	Vega, Aragones (2011)	243	31
DC97[20]	F. Wang, Lindberg (2008)	240	78
SPC/E[16]	Vega, MacDowell (2010)	200	49
SPC/E[15a]	Rick, Haymet (2003)	240	50
E3B[19]	Skinner (2014)	240	106
E3B[19]	Skinner (2014)	200	130
TIP4P-FQ[15a]	Rick, Haymet (2003)	240	100(5)
AMOEBA03[26]	Ren, Ponder et al. (2003)	250	121
i-AMOEBA[27]	L.P. Wang et al. (2013)	240	107(5)
AMOEBA14[1]	Laury, Ponder et al. (2015)	250	98
Experiment[11]	Whalley (1981)	240	107
Experiment[11]	Whalley (1981)	200	130
PAW-PBE[21]	F. Wang, Rusnak (2012)	253	67(7)
PBE-D2[23]	Slater, VandeVondele (2014)	150	366

PBE0-D2[23]	Slater, VandeVondele (2014)	150	266
PIMD [24]	Moreira, Koning (2015)	100	308

In this study, we investigated the dielectric property of ice Ih from classical molecular dynamics simulations using both non-polarizable force fields and different polarizable force fields, to better understand the importance of polarizability for the correct prediction of ε_s of ice Ih from force fields. We also studied the different proton disorder patterns in ice Ih and correlate the different configurational potential energies with the dipole moment of different simulation boxes. Finally, we did an initial study of the effect of NQE on the molecular geometry from a path-integral molecular dynamics simulation.

2.2 COMPUTATIONAL METHODS

The rigid non-polarizable TIP4P[9] water model as well as its reparametrized variants TIP4P/Ice[28], TIP4P/Ewald[29], the polarizable Dang-Chang (DC97) model[2], the revised AMOEBA force field[1] (AMOEBA14) as well as the AMOEBA model that employs the Gaussian electrostatic model distributed multipoles (GEM-DM)[30] are considered in our calculations.

Classical MD simulations for all the non-polarizable force fields and the polarizable DC97 model were carried out using a modified version of the DL_POLY program[31] obtained from the Wang group[8]. A time step of 1.0 fs and a cutoff radius of 9.0 Å for van der Waals interactions were used. Long-range electrostatic interactions were treated with the Ewald summation method[32]. The parameters in the sampling procedure with the electrostatic switching

algorithm were kept the same as the original paper[8]. The scheme representing the sampling procedure is depicted in **Figure 2.4**.

Figure 2.4 The scheme for electrostatic switching procedure for sampling of proton-disordered ice Ih.

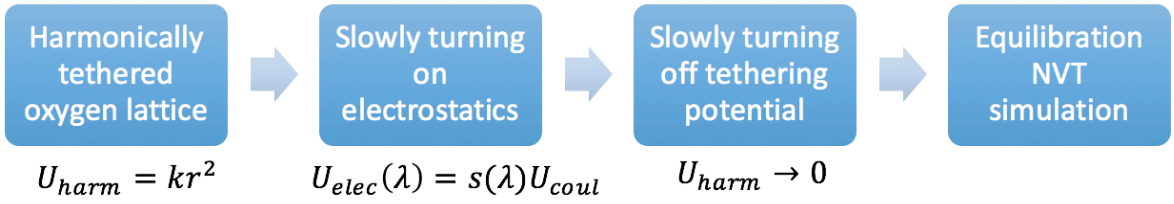

All the simulations were carried out NVT ensemble. Unless otherwise stated, for each set of calculations the ensemble generated consisted of 200 configurations, at temperatures of T =50, 100, 150, 200 and 240 K, for ice Ih. The dimension $\{L_x, L_y, L_z\}$ of the unit cells for ice Ih used in the simulations are listed in **Table 2.2,** and the lattice vectors $\{a, b, c\}$ of the fundamental cells crystallographically determined.

Table 2.2 Dimensions of simulation cells used in this study. a, b, c are the cell vectors of the primitive cell to be replicated for each simulation cell; L_x, L_y, L_z are the box dimensions of the final simulation cell; N_x, N_y, N_z are the replication factors in each dimension; N is the number of water molecules in the final simulation cell; Symm. is the symmetry of the final simulation cell.

a (Å)	*b* (Å)	*c* (Å)	L_x (Å)	L_y (Å)	L_z (Å)	N_x	N_y	N_z	*N*	*Symm.*
4.492	4.492	7.336	17.969	17.969	14.672	4	4	2	128	hexagonal
4.492	4.492	7.336	22.461	22.461	22.007	5	5	3	300	hexagonal
4.507	7.806	7.360	27.042	23.419	22.080	6	3	3	432	Orthorhombic

For the calculation of the dielectric constant of ice Ih using the polarizable AMOEBA models (AMOEBA14 and GEM-DM), the TINKER package version 7.1.2[33] was used, and simulation settings were kept the same as the sampling procedure above. An orthorhombic simulation cell with 432 water molecules was used for these simulations. For comparison, **Table**

3.3 tabulates the parameters of the different force fields used in this study, along with the respective values of molecular dipole moment for water.

For the path-integral MD simulations, AMBER package version 12[34] was used. We used the normal mode path-integral MD (NMPIMD) implementation in AMBER, and Nosé-Hoover chains were coupled to each bead in the system to accomplish thermostatting. The number of beads was chosen to be 24, which was shown to be large enough for the convergence of ice simulations at the same temperature[24]. The simulations were carried out at T = 100 K, which is close to the phase transition temperature of ice Ih to XI at 72 K, and converged PIMD results can be obtained under this temperature by using a moderate number of replicas[24]. The simple charge, flexible water force field q-spc/fw[35] specifically designed to investigate nuclear quantum effects in water was used in the PIMD simulation.

2.3 RESULTS AND DISCUSSION

2.3.1 Structural properties of proton-disordered ice Ih

We first considered the structural properties of different proton-disordered structures are compared. The radial distribution functions (RDF) that describe the local structures of hydrogen bond network in ice Ih are compared. As shown for the oxygen-oxygen ($g_{OO}(r)$), oxygen-hydrogen ($g_{OH}(r)$), and hydrogen-hydrogen ($g_{HH}(r)$) radial distribution functions (RDFs) in **Figure 2.5** for the TIP4P model, the RDFs are nearly identical for ten randomly selected proton-disordered configurations, sampled at T = 200 K. The height and shapes of the peaks are consistent with the previous study using the same sampling algorithm[8]. Based on the RDFs, all

the oxygen atoms in sampled ice Ih lattice are covalently bonded to two adjacent hydrogen atoms, and form hydrogen bonds with two other adjacent hydrogen atoms, satisfying the ice rules.

Figure 2.5 The oxygen-oxygen, oxygen-hydrogen and hydrogen-hydrogen radial distribution functions of 10 randomly chosen ice Ih configurations from TIP4P model at T = 200 K.

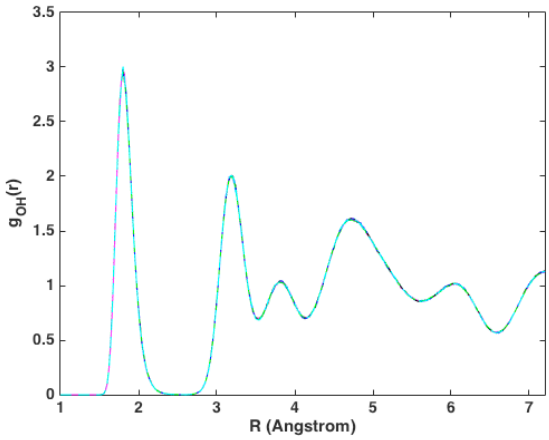

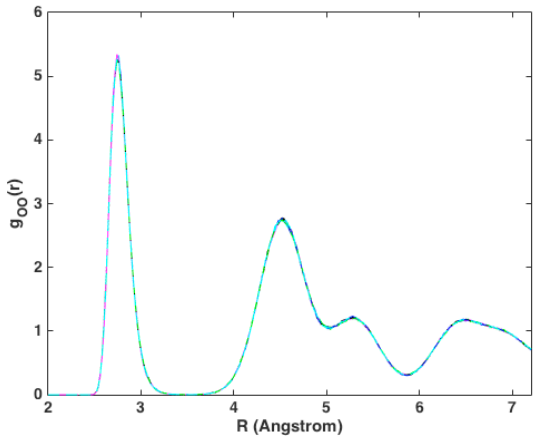

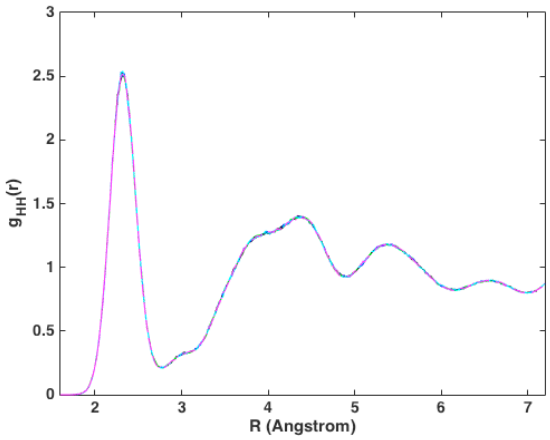

Figure 2.6 Vibrational density of states of 10 randomly chosen ice configurations from TIP4P model at T = 200 K, in the region of 0-1600 cm^{-1}, with two regions due to a) translational and b) librational motions, respectively.

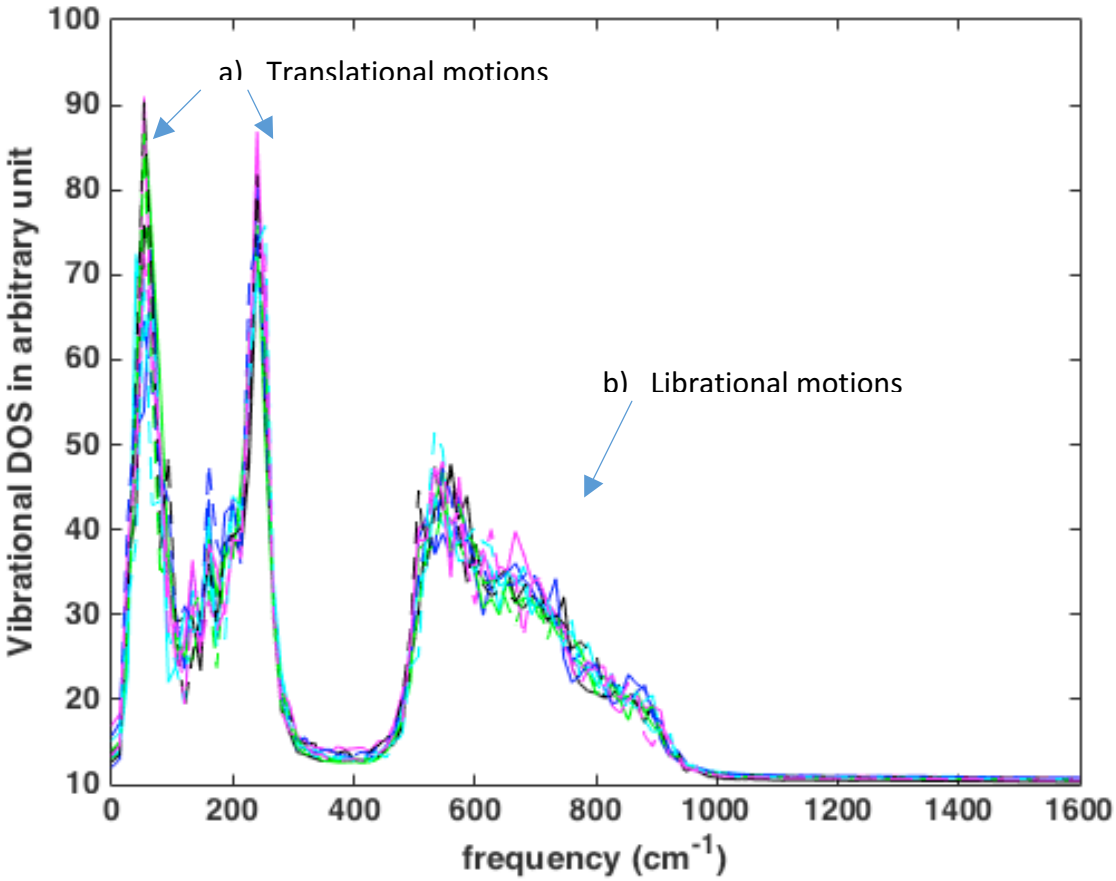

I also plotted the vibrational density of states (VDOS) of ten randomly chosen ice Ih structures sampled using the TIP4P model, calculated from the velocity auto-correlation function during an equilibrium MD simulation at T = 200 K. As shown in **Figure 2.6**, each VDOS in the region of 1-1000 cm^{-1} is separated into two parts: a) the lower frequency region due to translational motions, b) the higher frequency part due to librational motions. The ten DOSs were also shown to have peaks at the same frequencies for both regions that represent intermolecular hydrogen bonds, with only small variations of intensities.

Figure 2.7 Distribution of configurational energy of ice Ih sampled from TIP4P model, at different temperatures.

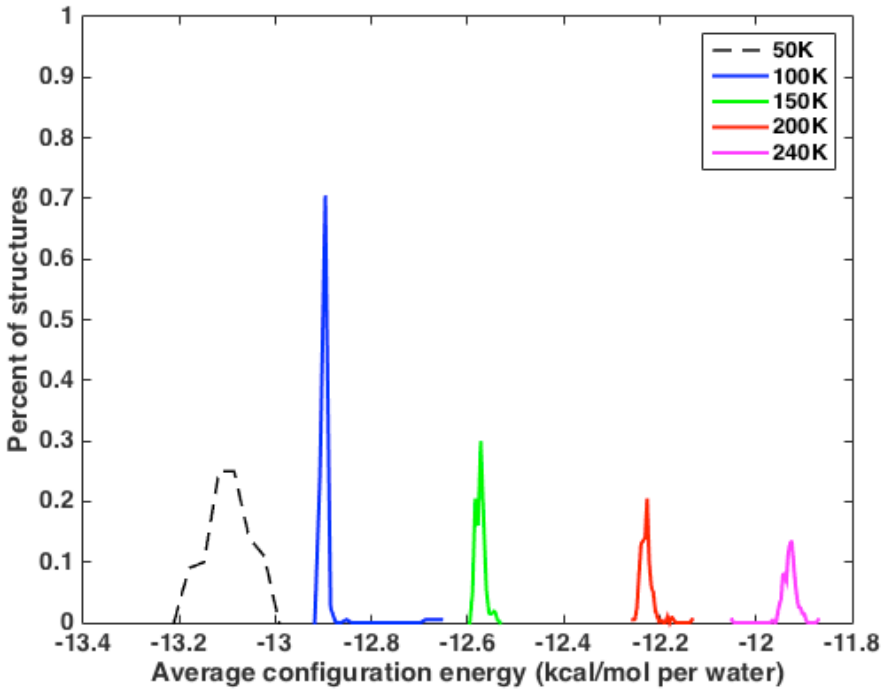

To confirm that the structures sampled are indeed equilibrium structures that satisfy the Boltzmann distribution, the configurational energy distributions were also plotted, as displayed in **Figure 2.7**. For T = 100, 150, 200 and 240K, the distribution range reproduces Wang's Figure[8]. At T = 50 K, there were observed "shoulders" for the energy distribution. This

difference was also shown in the dipole moment distributions of ice Ih at different temperatures in **Figure 2.8**.

Figure 2.8 Distributions of the box dipole moment along c-axis (M_c) of hexagonal ice Ih cells sampled from TIP4P model with 300 water molecules, at different temperatures.

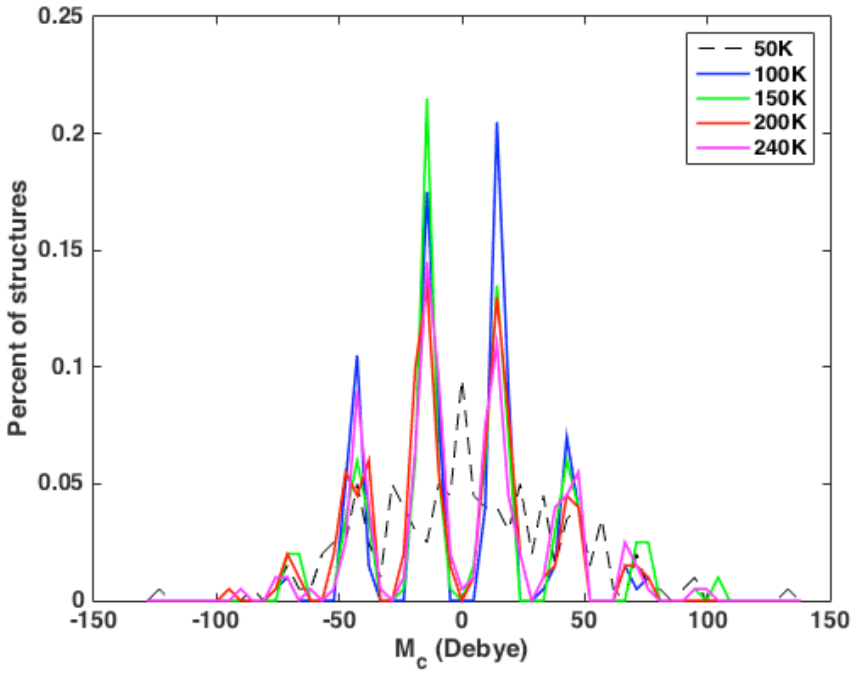

At T = 50 K, A continuous distribution of dipole moment was displayed in the dipole moment distributions, while higher-temperature results show clear dipole spacing as multiples of "percolating loops" in **Figure 2.3(B)**. (We refer to **Figure 2.9** and ref[18] for an interpretation of this spacing). The unphysical results of the simulations at T = 50 K are believed to be due to the simulation time not being long enough for the protons to overcome local minima and form to equilibrated structures during the second sampling step, when the switching function for electrostatic interaction is slowly being turned on.

Then, I calculated the average potential energy per water molecule in these boxes. The results shown as a function of the component along *c*-axis of the total dipole moment M_c, as

presented in **Figure 2.9**. For all the simulation cells, the potential energy varies by about 0.1 kcal/mol per water molecule with slight variances over cell sizes.

Figure 2.9 Configuration energy versus dipole along c-axis of ice Ih cell with 128, 300 and 432 waters.

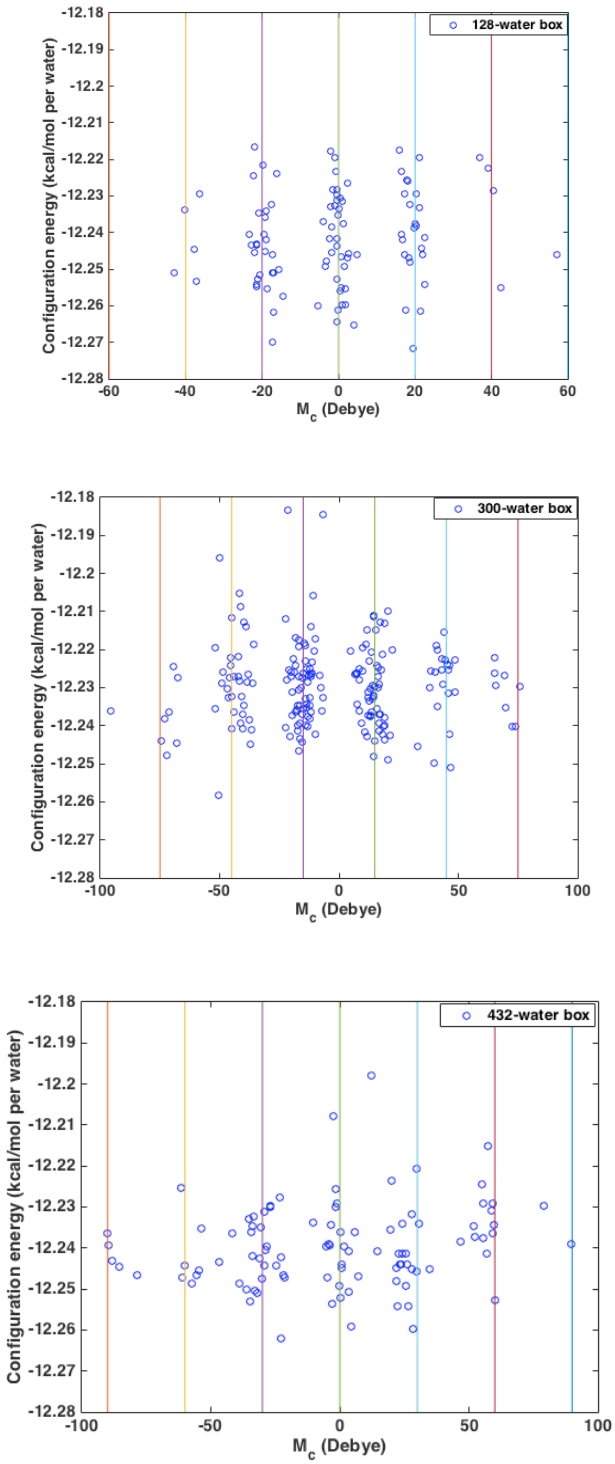

Figure 2.10 Interpretation of the dipole spacing in ice Ih: the two different proton disordered configurations a and b shown below differ in multiples of the orientation of one hydrogen bonds, which is seen as a flip of one O-H bond (O_2-H_1 in a) change the position from oblique to along the c-axis, to form configuration b. When the periodic boundary is being crossed, this single flip leads to the change of dipole moment along c-axis $\Delta\mu_c=2*\mu*\cos(109.47°/2)$, where μ is the molecular dipole moment. Depending on the size of simulation boxes, the spacing magnitudes are different.

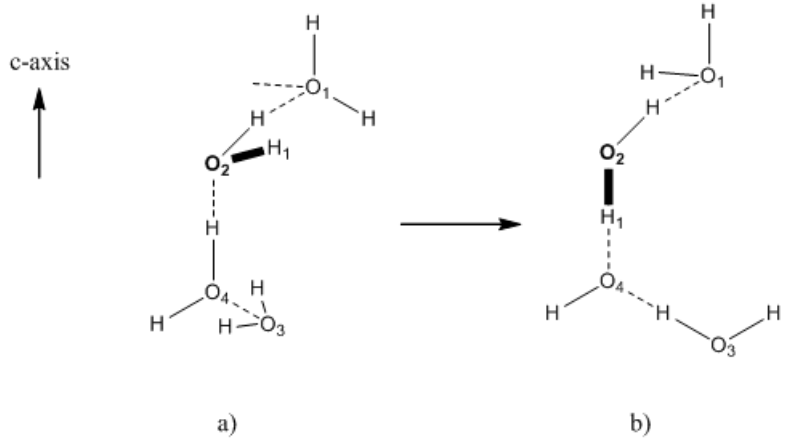

Besides the RDFs, VDOS and energy and dipole distributions, the microscopic structural properties of hydrogen-bonded proton-disordered ice Ih can be obtained and quantified from the relative projection of two adjacent water monomers with respect to the *c*-axis in the lattice can be either parallel or oblique[7]. Researchers have come up with several nomenclature schemes for these four types of hydrogen bonds, and here we adopt the one used by Bjerrum[7], namely oblique mirror (OM), oblique center (OC), inverse mirror (IM) and inverse center (IC). These parameters are based on the dihedral angle between the bisectors of the H-O-H angles of two adjacent water monomers. These torsional angles are distributed around four angles: 0°, 60°, 120° and 180°, with distribution widths of about ± 20° (varying with temperatures). Based on these angles, the hydrogen bond in ice Ih can be defined as inverse center (0°), oblique mirror (60°), oblique center (120°) and inverse mirror (180°). The orientations of oblique-mirror and inverse-mirror

type H-bonds are parallel to *c*-axis, and the oblique-center and inverse-center H-bonds are oblique to the *c*-axis of ice Ih, as shown in **Figure 2.11**.

Figure 2.11 Possible hydrogen-bonded water dimer arrangement in ice Ih.

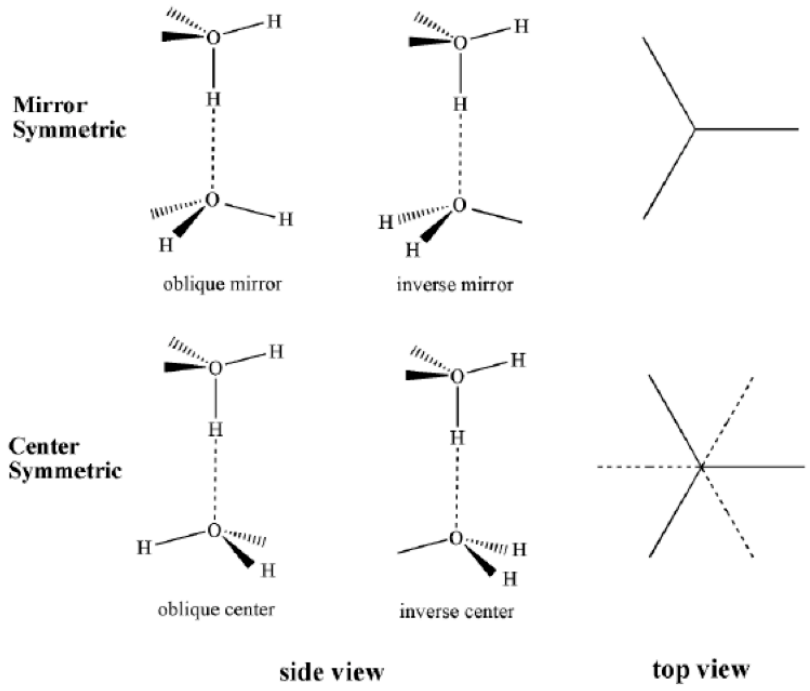

I then plotted the distribution of these dihedral angles under different temperatures in **Figure 2.12**, for sampled structures using TIP4P model. For the four hydrogen bonds per water molecule, one of them is along the c-axis, and three others oblique to c-axis, therefore the sum of percentage of IM (X_{IM}) and of OM (X_{OM}) for each water molecule is 1, and the sum of X_{IC} and X_{OC} is 3. For all the five temperatures considered, the OC type angles are mostly observed, with the relative height of X_{OC} comparing with other angles decrease. As calculated by Bjerrum in 1952 using a simple electrostatic model, the lattice energy difference between mirror symmetric (IM plus OM) and center symmetric (IC plus OC) at low temperatures is 0.42 kcal/mol with the latter being more stable, and the difference decreases as T increases[7]. Therefore, it would be very interesting to get the energetic difference of these proton ordering patterns in the future.

Figure 2.12 Distributions of the dihedral angle between the bisectors of two adjacent water molecules in ice Ih at T = 200 K, calculated from hexagonal simulations cells with 300 water molecules, sampled with TIP4P model.

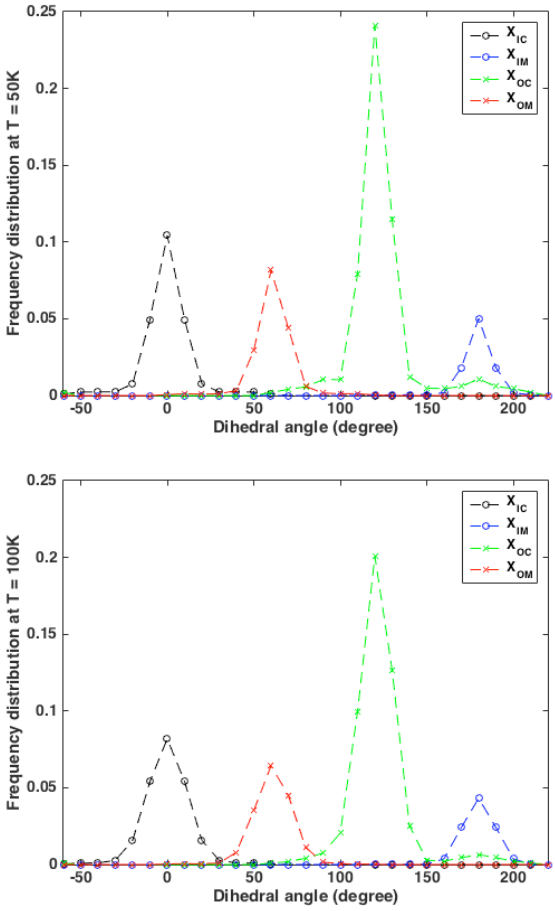

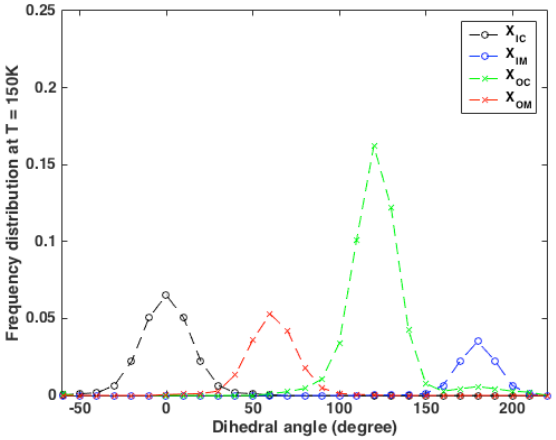
Frequency distribution at T = 150K
Dihedral angle (degree)
X_IC
X_IM
X_OC
X_OM

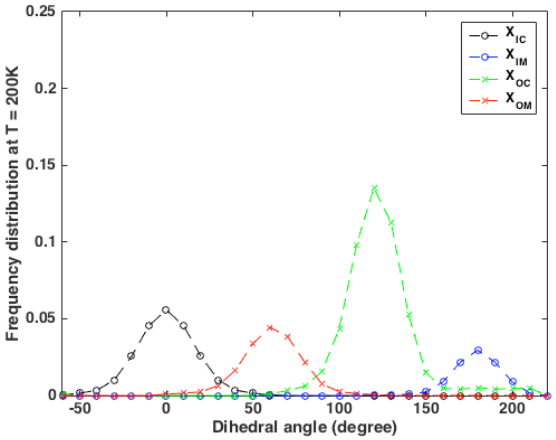
Frequency distribution at T = 200K
Dihedral angle (degree)
X_IC
X_IM
X_OC
X_OM

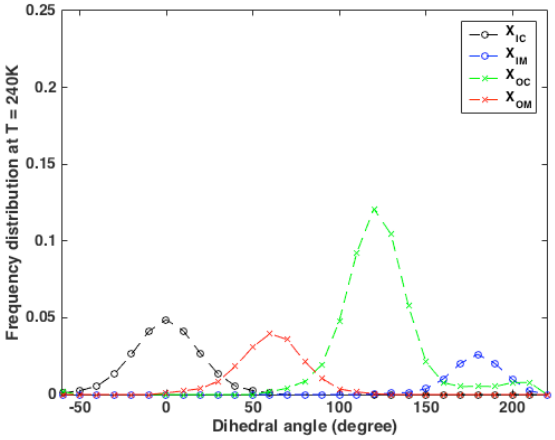
Frequency distribution at T = 240K
Dihedral angle (degree)
X_IC
X_IM
X_OC
X_OM

2.3.2 Dielectric constant calculation for ice Ih

The static dielectric constant can be determined from the dipole fluctuations of the system $\langle \vec{M}^2 \rangle - \langle \vec{M} \rangle \cdot \langle \vec{M} \rangle$ using **Equation 2.1**. In this study, by averaging over the results from 200 configurations, with the non-polarizable TIP4P, TIP4P/Ice and TIP4P/Ewald models at T = 100, 150, 200 and 240 K, the polarizable DC97 model at T = 240 K, the AMOEBA14 model at T = 100, 150, 240 K, and the GEM-DM model at 100 and 240 K, values of dielectric constant were obtained as plotted in **Figure 2.13**, for comparison with experimental values. For each force field considered, the calculated dielectric constant varies as 1/T.

Figure 2.13 Calculated static dielectric constant of ice Ih from different force fields, compared with experimental values over temperatures.

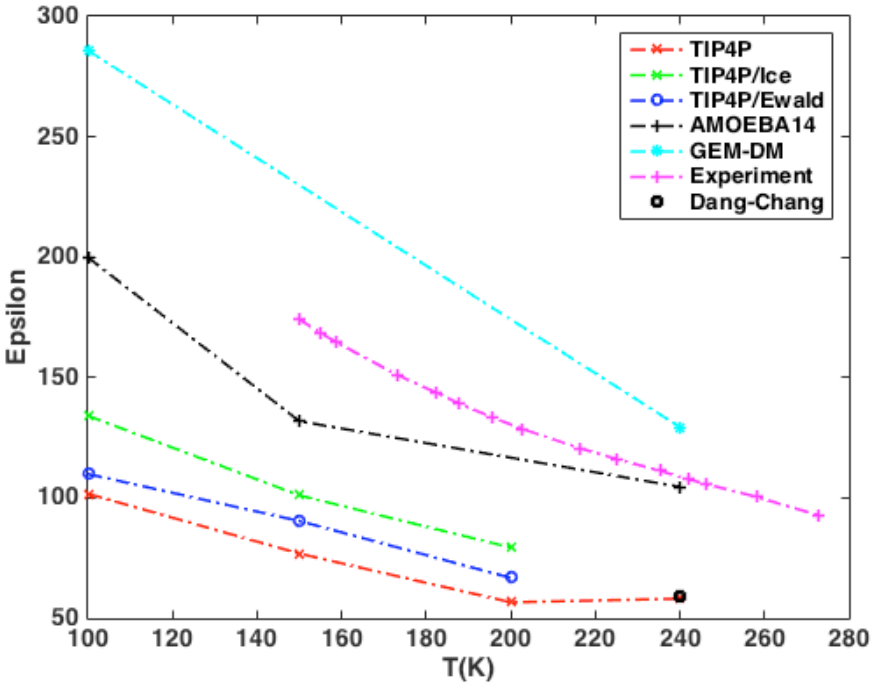

At T = 100, 150 and 200 K, the TIP4P/Ice model gives the best results among all the TIP4P variants. This force field is a re-parametrization designed to better describe the bulk

properties of ice. TIP4P/Ewald model is a re-parametrization of the TIP4P model for better reproduction of bulk properties of liquid water, and it performs better than the original TIP4P model at T =100, 150 and 200 K.

The three polarizable models used in this study (DC97[2], AMOEBA14 and GEM-DM) overall give higher predictions of ε_s compared with the TIP4P models for each temperature. The three models all account for polarization using point induced dipoles $\vec{\mu}_{ind}$[36]:

$$\vec{\mu}_{ind} = \alpha(\vec{E}^0 + \vec{E}^p) \qquad \text{Equation 2.3}$$

where $\vec{E}^0$ is the field due to the permanent atomic charges and $\vec{E}^p$ is the field due to the other induced dipoles. The total field is calculated via a self-consistent way to minimize the polarization energy, or using the extended Lagrangian method[37]. The molecular dipole $\vec{\mu}_i$ for water molecule *i* thus is the sum of the permanent dipole $\vec{\mu}_{perm}$ and the induced dipole $\vec{\mu}_{ind}$, and is evaluated individually for each molecule in the simulation cell:

$$\vec{\mu}_i = \vec{\mu}_{perm} + \vec{\mu}_{ind} \qquad \text{Equation 2.4}$$

The polarization energy part in the intermolecular interaction energy is expressed as the following summation over polarizable centers:

$$E_{pol} = -\frac{1}{2}\sum \vec{\mu}_i \cdot \vec{E}_i \qquad \text{Equation 2.5}$$

For a comparison of the total interaction energies among the AMOEBA force fields, we calculated the cohesive energy of four water hexamer isomers (prism, cage, book, ring) after being fully optimized using different polarizable water models, compared with the CCSD(T) reference values taken from ref[38]. As seen in **Figure 2.14**, among the three versions of AMOEBA force fields and the TTM3-F force field[39], only the TTM3-F model reproduced well both the relative stability as well as the values of energies comparing with the CCSD(T) reference values. The reparametrized AMOEBA14 model actually performs more poorly than

the original AMOEBA model. The inexpensive i-AMOEBA model that omits the expensive iterative evaluation of the mutual polarization is much too repulsive.

Figure 2.14 Binding energy of four isomers of water hexamer (prism, cage, book and ring) with four polarizable force fields: AMOEBA14, AMOEBA03, i-AMOEBA and TTM3-F, compared with the CCSD(T) reference values.

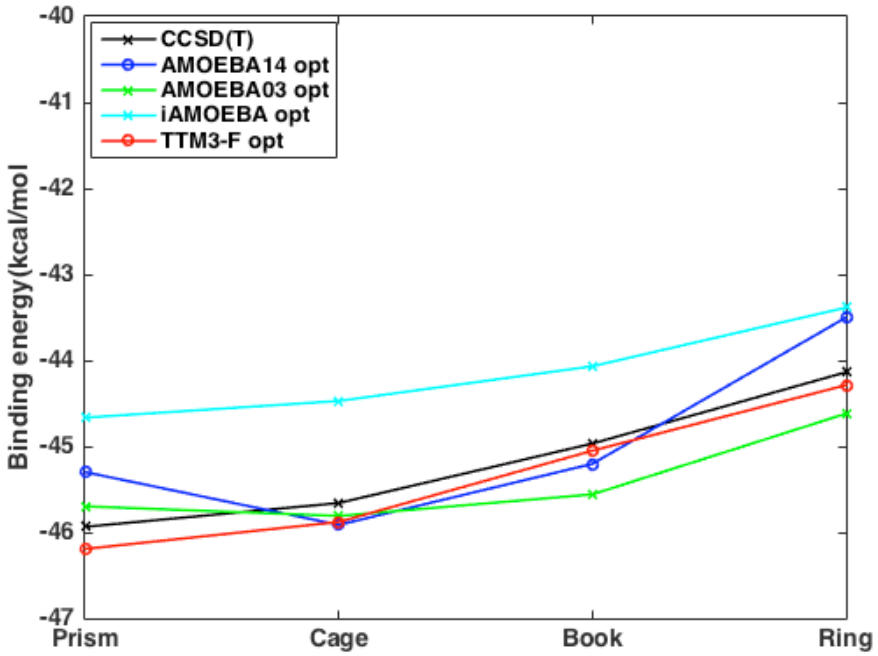

These polarizable force fields differ in the number of polarizable centers per molecule. DC97 and AMOEBAs have one and three polarizable centers per molecule, respectively. While all of the polarizable force fields give better predictions of ε_s of ice Ih than do the TIP4P variants, the two AMOEBA models perform better than the DC97 model overall. While the i-AMOBEA model was aimed at using the inexpensive way to achieve good thermodynamic bulk properties for water, its neglect of the mutual polarization results in lower average molecular dipole moment comparing with the AMOEBA model that include mutual polarization. GEM-DM replaces the distributed atomic multipoles in the AMOEBA model with the ones derived from

the Gaussian electrostatic model (GEM), and it keeps the other parameters as in the original AMOEBA model. However, this led to the over fluctuation of the system.

Table 2.3 Parameters and the molecular dipole moment μ of the force fields used in this study.

Model	q_H (e^-)	r_{OM} (Å)	θ_{HOH} (°)	r_{OH} (Å)	ε (kcal/mol)	σ (Å)	μ (D)
TIP4P[9]	0.520	0.150	104.52	0.9572	0.1550	3.1536	2.177[b]
TIP4P/Ice[28]	0.5897	0.1577	104.52	0.9572	0.2108	3.1668	2.426[b]
TIP4P/Ew[29]	0.5242	0.125	104.52	0.9572	0.1628	3.1634	2.321[b]
DC97[2]	0.5190	0.215	104.52	0.9572	0.1825	3.2340	1.850[c]
AMOEBA03[26]	0.25983	--	108.5	0.9572	0.11/0.0135[a]	3.405/2.655[a]	1.771[c]
i-AMOEBA[27]	0.29701	--	106.48	0.9584	0.1968/0[a]	3.645/0[a]	1.86[c]
AMOEBA14[1]	0.21308	--	107.9	0.9565	0.151/0.0105[a]	3.579/2.117[a]	1.808[c]
GEM-DM[30]	0.471	--	108.5	0.9572	0.11/0.0135[a]	3.405/2.655[a]	1.808
Exp.[40]	0.471	--	108.5	--	--		1.855[c]

[a]parameter for O atom/parameter for H atom;
[b]liquid phase value; [c]gas phase value.

Table 2.4 Dielectric constant and Polarization Factor G for ice Ih for the TIP4P/Ice, TIP4P/Ewald, TIP4P, AMOEBA14, and GEM-DM Models.

Model	T(K)	ε_s	G
AMOEBA14	100	199.9	6.568
AMOEBA14	150	131.8	8.458
AMOEBA14	240	104.6	7.120
GEM-DM	100	285.8	8.860
GEM-DM	240	129.4	9.836

TIP4P/Ice	100	134.1	2.470
TIP4P/Ice	150	101.0	2.796
TIP4P/Ice	200	79.4	2.937
TIP4P/Ewald	100	109.9	2.194
TIP4P/Ewald	150	90.4	2.708
TIP4P/Ewald	200	66.8	2.662
TIP4P	100	101.7	2.322
TIP4P	150	76.8	2.645
TIP4P	200	56.6	2.600
TIP4P	240	58.1	3.203

From **Equation 2.2**, we know that the value of ε_s is also affected by the polarization factor *G*, and I then calculated the *G* factor from each force field, as tabulated together with the results of ε_s in **Table 2.4**. For all water models, the value of *G* increases slowly with temperature, and this trend was observed from an early model of water[41]. The two polarizable models AMOEBA14 and GEM-DM give the *G* values 2-3 times larger than three non-polarizable TIP4P models, and this ratio is nearly correlated with the ratio of predicted ε_s. The GEM-DM model that predicts the highest ε_s also have highest values of *G*. The second component in the equation of ε_s: the molecular dipole moment $|\vec{\mu}|$, is also reflected in the comparison of **Table 2.3** and **Table 2.4**. For the non-polarizable models, the order of $|\vec{\mu}|$ is TIP4P/Ice > TIP4P/Ewald > TIP4P, and same order is observed in the values of ε_s.

2.3.3 Nuclear quantum fluctuations from PIMD

In a recent study, nuclear quantum effects (NQE) were shown to be significantly impacting the hydrogen bond topology in ice Ih, as well as the geometry of the water monomer, which affect the average value of molecular dipole moment[24]. To further study the effect of NQE, I did an initial PIMD simulation at the same temperature (T = 100 K) for ice Ih using a force field specifically parametrized for quantum simulations: q-spcfw[35]. I was wondering about the magnitude of quantum effect in the dipole moment distribution and the molecular geometry.

I first performed the equilibrium simulation under NPT ensemble for 200 ps with the timestep of 0.1 fs, and then examined the fluctuations of the system temperature in each simulation step during a second equilibrium NVT run with the Nose-Hover chain thermostat. PIMD gave wider distributions (100 ± 10 K) of temperature, comparing with the classical MD profile (100 ± 1.5 K), as shown in **Figure 2.15**. The O-H bond length (r_{OH}), from PIMD calculations give wider distribution than of r_{OH} (MD), as shown in **Figure 2.16**. As tabulated in **Table 2.5**, the magnitude of the average r_{OH} is shifted towards longer bond lengths in quantum distributions. This is because when quantum effect is taken into account, the anharmonicity of the O-H stretch in the potential energy surface is included. The zero-point energy allows the proton involved in the hydrogen bond to extend in the direction of the acceptor oxygen to form stronger hydrogen bond, and therefore makes the O-H bond longer[42].

Table 2.5 Mean values of the molecular angle H-O-H (degree), the bond length r(O-H) (Å), the molecular dipole moment μ (debye) and the dipole fluctuation of ice Ih from classical MD simulation and PIMD with 24 replicas at T = 100 K. The unit cell of ice Ih contains 288 water molecules.

Method	r_{OH} (Å)
PIMD	1.143
Classical MD	0.887
PIMD in ref[24]	1.030±0.003
Classical MD in ref[24]	1.0072±0.0002

Figure 2.15 Distribution of the temperature during classical MD and PIMD simulations using q-spcfw model for ice Ih at T = 100 K.

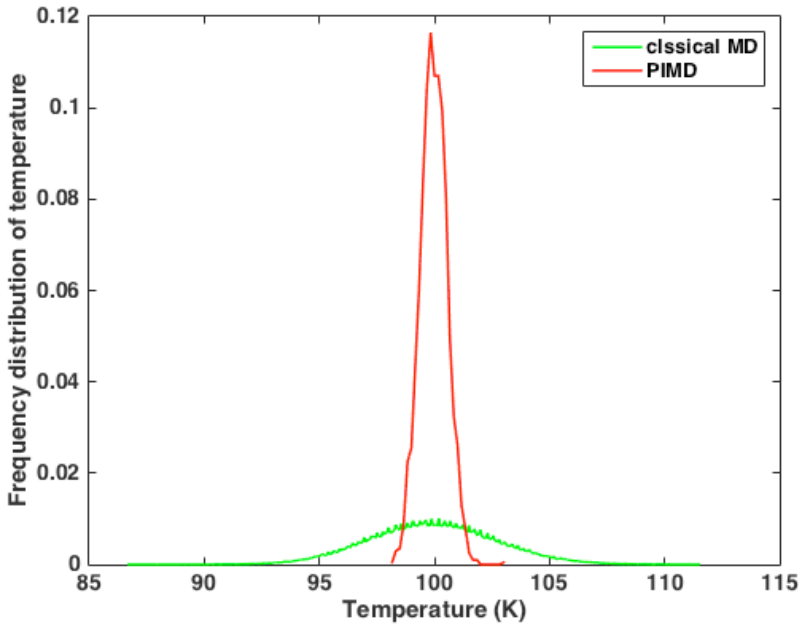

Figure 2.16 Distribution of the bond length r_{OH} (Å) during classical MD and PIMD simulations using q-spcfw model for ice Ih at T = 100 K.

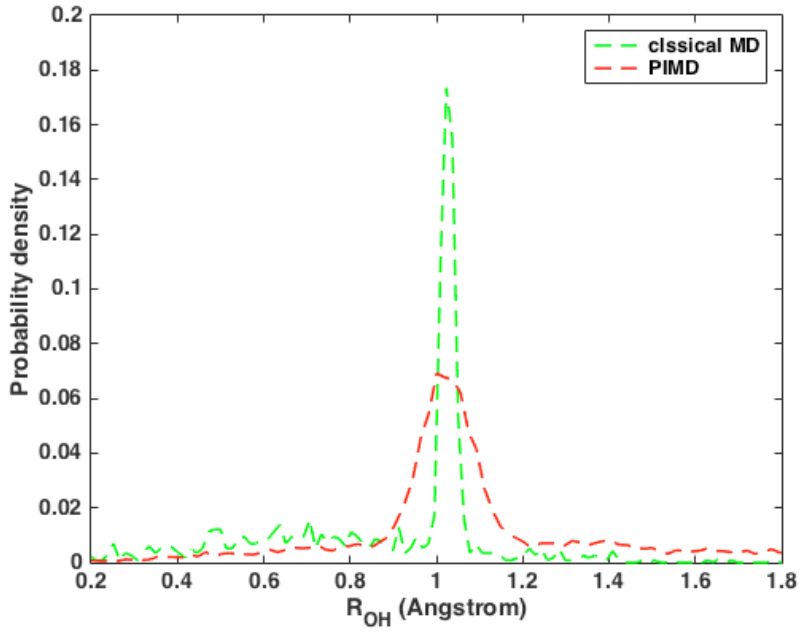

At the current stage, I only performed PIMD simulations on a single configuration of ice Ih. It would be interesting to perform PIMD simulations of different ice Ih configurations that are sampled with electrostatic switching or MC-based methods, to obtain the quantum effect in the dielectric constant. I would expect that due to the elongation of O-H bond length, the mean value of the molecular dipole moment from multiple PIMD simulations would increase as well. In terms of dielectric constant, assuming the polarization factor *G* is not affected by quantum effects, then the higher average molecular dipole moment in quantum simulations would probably lead to a higher dielectric constant than that in classical simulations.

2.4 CONCLUSIONS

To summarize, different proton-disordered ice Ih structures were generated, using a molecular dynamics procedure introduced by Lindberg and Wang. I employed both non-polarizable force fields TIP4Ps and several polarizable force fields with point inducible dipoles. I first examined the structural properties of sampled ice Ih configurations, including RDFs, VDOS and distribution of their configurational energies. Then, I determined the static dielectric constant ε_s of ice Ih from these force fields. The results showed that:1) all polarizable models give better predictions of dielectric constant of ice Ih comparing with non-polarizable models; 2) Polarizable models with three polarizable sites per molecule gave better results than the Dang Chang model with a single polarizable site per molecule. This will guide the development of polarizable force fields in the future for achieving better reproduction of condensed phase water properties in MD simulations. 3) The polarization factor *G* values in each force field are almost linearly related with the value of their predicted ε_s of ice Ih. 4) our initial PIMD calculations of ice Ih at 100 K showed the elongated O-H bond length in quantum simulations, and further investigation of the nuclear quantum effect on the ε_s of ice Ih is under way. The better prediction of ε_s for ice Ih using AMEOBA models is due to two reasons corresponding to the two factors in Equation 2.2: 1) calculations of the molecular dipole moment from AMOEBA models give better accuracy by taking into account the mutual polarization from the neighboring water molecules; 2) The polarization factor *G* from these models is higher than the value predicted by the TIP4P models, which means the relative orientations of water molecules in ice Ih are more accurate in AMOEBA models.

2.5 OPEN QUESTIONS

Based on the graph invariant enumeration technique proposed by Kuo and coworkers in 2001[14], the full set of ice-rule-allowed ice Ih structures can be reduced to a much smaller set, as tabulated in **Table 2.6**. Each of the symmetry distinct cells represents a deep local minimum, with the physical properties such as energy and dipole being "invariants", shared by all the ice-rule-allowed configurations that are symmetry-related by this cell. The canonical partition function Q for a specific type of cell is calculated as[43]:

$$Q = \sum_{i=1}^{M} f_i e^{-\beta(E_i + A_{vib,i})} \qquad \text{Equation 2.6}$$

where f_i is the number of symmetry-related configurations that are represented by one symmetry distinct configuration, $\beta = \frac{1}{k_B T}$, E_i is the potential energy of the isomer, M is the number of symmetry distinct structures, $A_{vib,i}$ is the vibrational energy of the isomer.

Table 2.6 Enumeration of ice Ih configurations based on the graph invariant technique. N represents the number of water molecules in each cell; Symm. represents the symmetry of each cell (hex is short for hexagonal and orth is short for orthorhombic); $N_{symm\text{-}distinct}$ represents the number of symmetry distinct structures enumerated from graph invariant; $N_{ice\text{-}rule\text{-}allowed}$ represents the number of ice-rule-allowed cells corresponding to each cell.

N	Symm.	$N_{symm\text{-}distinct}$	$N_{ice\text{-}rule\text{-}allowed}$
4	hex	2	18
8	orth	16	114
12	hex	14	552
16	hex	139	2970
24	orth	2275	98466
48	hex	8360361	2404144962

Since the graph invariants in small unit cells are a subset of the graph invariants of larger unit cells, the energies of the substantial amount of hydrogen bond patterns in larger supercells can be parametrized from the high level calculation of energies and dipoles in small unit cells with 50-60 water molecules. Therefore, in the future, it would be interesting to obtain *ab initio* energies and dipoles of the symmetry distinct supercells of ice Ih from periodic calculations with sufficient k-point sampling, and to extrapolate to larger supercells to calculate the dielectric constant of ice Ih.

3.0 ENERGETIC STUDY OF ICE IH AND VIII FROM DISPERSION CORRECTED DFT METHODS

3.1 INTRODUCTION

3.1.1 Overview of previous energetics studies of ice phases

There are 15 known phases of ice, which are identified by the Roman numerals I through XV, with each phase being stable over a limited range of temperature and pressure[3b]. Phase I ice with hexagonal symmetry, denoted as ice Ih, is the most common phase of ice, and is the most widely studied. On the ice Ih lattice, the hydrogen atoms can adopt different positions, as long as the "Bernal-Fowler" ice rules[4] are satisfied, to form the hydrogen bond (H-bond) network. This leads to the proton-disordered nature of ice Ih at T > 72 K. However, at temperatures below 72 K, a phase transition from ice Ih to ferroelectric ice XI is observed, provided dopants (for example, KOH) are present to allow for the formation of defects on the ice Ih lattice. Unlike ice Ih, the structure of ice XI is proton-ordered, with symmetry $Cmc2_1$. The hydrogen bonds along the *c*-axis of ferroelectric ice XI lattice align in the same direction, leading to a large magnitude of the dipole moment in the bulk phase with the "percolating loops" spanning the hydrogen bonds crossing the unit cell, as illustrated in **Figure 3.1(b)**.

Ice Ih can also be connected to a proton-ordered anti-ferroelectric ice with symmetry *Pna2₁* and designated ice VIII. In contrast to the high-dipole ferroelectric ice XI, the hydrogen bonds along the *c*-axis of anti-ferroelectric ice result in a near-zero dipole moment along this direction, and a closed loop is formed as shown in **Figure 3.1(a)**. On the lattice of the proton-disordered ice Ih, both of these *Cmc2₁* and *Pna2₁* "sub-" structures can be found. Ice VIII is stable at low temperatures over the pressure range of 2 to 60 GPa[44].

Figure 3.1 Proton arrangements in the crystal of ice Ih for the a) ferroelectric $Cmc2_1$ and b) anti-ferroelectric $Pna2_1$ structures.

a) Ferroelectric $Cmc2_1$, with the eight atoms forming a percolating loop labeled;

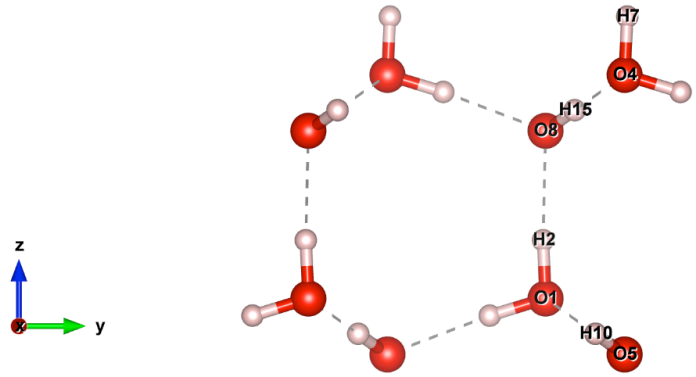

b) Anti-ferroelectric $Pna2_1$, with the twelve atoms forming a closed loop labeled;

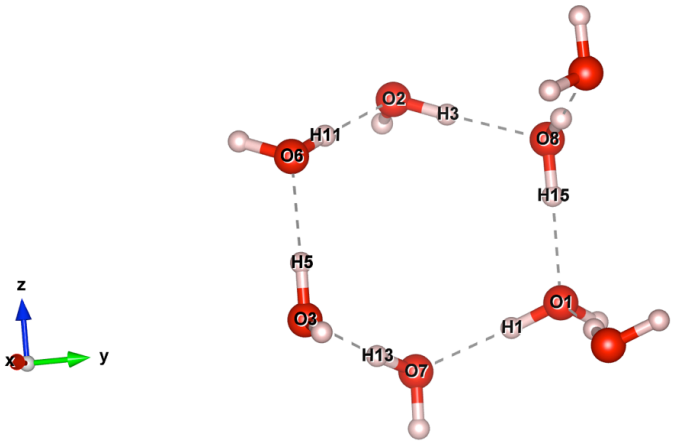

There has been controversy over the relative stabilities of the different orientations of hydrogen bonds of ice, given the subtle energetic differences between different hydrogen-bonded pairs. Of the four possible H-bonded dimer configurations shown in **Figure 3.3**, that with *trans*-H-bonded adjacent water molecules, which minimize the repulsions from vdW interaction and electrostatic interactions, is favored. Of the previous studies of ice Ih from the molecular mechanics approach, only a modified polarizable KW-pol model[45] by Buch and coworkers in 1998 and a study by Nada and coworkers in 2003 using their rigid six-site NvdW model[46] proved to be able to predict the ferroelectric-ordered ice to be most stable[46].

Figure 3.2 The four possible H-bonded dimer configurations in ice Ih: a) h-cis, b) h-trans, c) c-cis and d) c-trans.

a) h-cis;

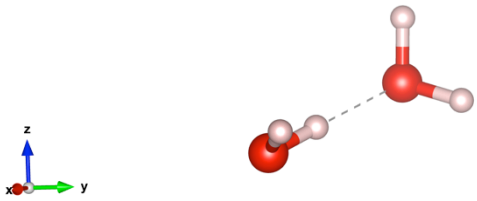

b) h-trans;

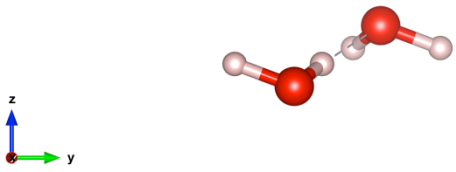

c) c-cis;

d) c-trans;

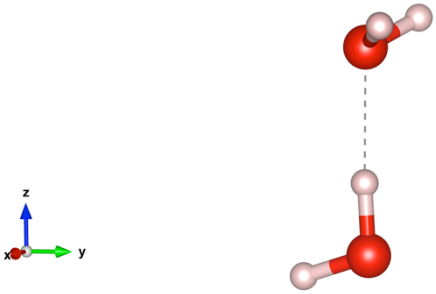

Density-functional theory (DFT) has been widely used to study water and ice[38], especially with generalized gradient approximations (GGA) functionals. The reliability of different semi-local GGA exchange-correlation functionals for ice remains a subject of debate, due to two problems: 1) the self-interaction error that leads to extra delocalization of protons in the H-bond; 2) their neglect of non-local correlations that are responsible for van der Waals (vdW) dispersion interactions. The first problem can be alleviated by including exact exchange via a hybrid functional, and to solve the second problem, dispersion corrections are needed in the functional to describe the vdW interactions in condensed phase systems.

Previous studies have used different dispersion correction schemes to calculate cohesive energy, and relative stabilities of different phases of ice, including both ambient pressure phases and high-pressure phases[47]. There are also studies discussing the equilibrium volumes of different structures and the role of zero-point energy for the cohesive energies and equilibrium volumes[48]. Among the previous DFT studies, there remains controversy over the relative

cohesive energies and densities of the different ice phases, as well as the role of nuclear quantum effects on the structural properties of ice[38]. In Ref. 9, it was shown that the nonlocal van der Waals functional vdW-DF2 used with PBE substantially overestimates the strength of hydrogen bonding in ice VIII, while underestimating it at low pressure for ice XI and Ih[49].

3.1.2 Motivation of this study

Motivation: Recently, our group reported two-channel dispersion-corrected atom-centered potentials (DCACP2) for use with semilocal GGA BLYP and PBE functionals[50]. For the water dimer and hexamer isomers, it was shown that the DCACP2-BLYP functional gives interaction energies that more closely reproduced the high-level CCSD(T) binding energy curves of these water clusters, than did the single-channel DCACP-corrected BLYP potential or Grimme's D3 corrected BLYP functional. Therefore, I wanted to analyze the performance of uncorrected and dispersion-corrected semilocal GGA BLYP functional at predicting the lattice parameters of fully optimized ice Ih cells, the cohesive energies, equilibrium volumes, and bulk modulus. I also compared the role of dispersion interactions and strength of hydrogen bonds between the ambient pressure phase ice Ih and the high-pressure proton-ordered ice VIII.

3.2 COMPUTATIONAL METHODS

3.2.1 Structures of ice used in this study

1. Proton-disordered ice Ih:

The proton-disordered hexagonal ice Ih unit cell used in this study contains 12 water molecules and was proposed by Hamann[51] with the initial lattice parameters equal to the experimental values: $a = b = 7.78$ Å, $c = 7.33$Å, $\alpha = \beta = 90°, \gamma = 60°$. This cell is replicated from the primitive 4-water hexagonal cell by 3*1*1. The oxygen atoms lie on the hexagonal lattice, while the hydrogen atoms are disordered such that each oxygen atom is hydrogen-bonded to two hydrogen atoms, and is covalently-bonded to two hydrogen atoms, and the net dipole moment of the system is near-zero, as presented in **Figure 3.3.**

Figure 3.3 12-water hexagonal ice Ih cell, with |a|=|b|, α = β = 90°, γ = 60°.

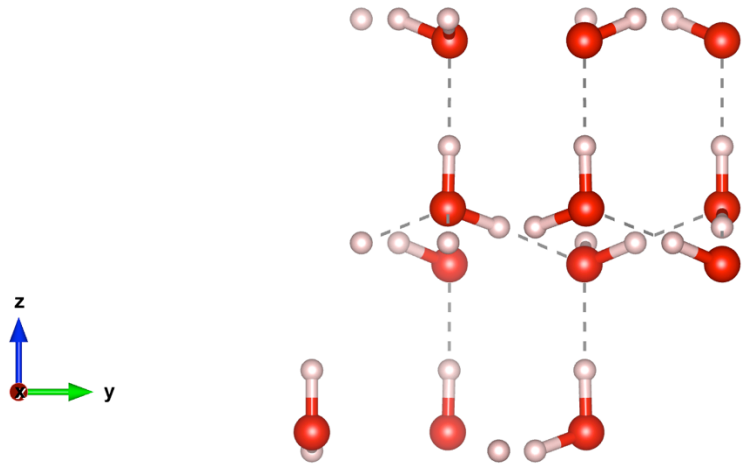

2. Proton-ordered ice VIII:

To model the anti-ferroelectric ordered phase ice VIII, a tetragonal unit cell with eight water molecules was obtained from experiment[52], and the tetragonal supercell with 64 water molecules used in the calculations replicated by 2x2x2 from the 8-water cell is shown in **Figure 3.4.** The lattice parameters are $a = b = 9.32$ Å, $c = 13.42$ Å.

Figure 3.4 64-water tetragonal ice VIII cell with |a|=|b|, α = β = γ = 90º.

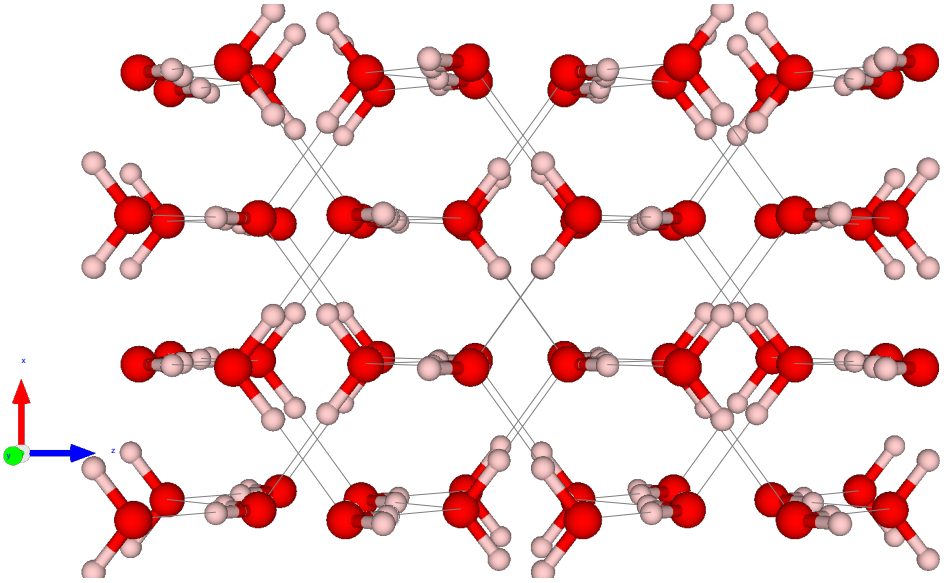

3.2.2 Calculation procedure

In this study, we have calculated the optimized structure, cohesive energy, equilibrium volumes, and bulk modulus of ice Ih and VIII. The CP2K code[53] was used to perform cell optimization and energy calculations with the generalized gradient approximation (GGA) BLYP[54] functional, as well as with the BLYP functional with different dispersion corrections: Grimmes' D3-correction scheme (BLYP-D3)[55], Grimmes' D3 correction with three-body interactions (BLYP-D3(3b))[55], dispersion-corrected-atom-centered potential (DCACP-BLYP)[56], and the two-channel version (DCACP2-BLYP)[50]. The calculations were performed using the Gaussian triple-ς TZV3P basis sets[57] with three sets of polarization functions and a plane-wave energy cutoff of 1200 Ry for the electronic density. Norm-conserving Goedecker-Teter-Hutter (GTH) pseudopotentials[58] were used for both hydrogen and oxygen.

Full geometry optimization including relaxation of the atomic coordinates and the cell lattice parameters was performed under periodic boundary conditions at zero external pressure using an

analytical stress tensor, with the Broyden–Fletcher–Goldfarb–Shanno (BFGS) optimizer for optimizing the cell parameters and the conjugate gradient (CG) method for optimizing the wave function.

3.3 RESULTS AND DISCUSSION

3.3.1 Lattice structures after cell optimization

The cell dimensions of ice Ih after optimization with different DFT methods are summarized in **Table 3.1**.

Table 3.1 Optimized cell dimensions (Å), Mean nearest-neighbor oxygen distance R_{OO} (Å), Mean of the intramolecular O-H bond lengths r_{OH} (Å) and HOH angles θ_{HOH} (degree) of the hexagonal ice-Ih cell with 12 water molecules with various DFT methods (|a|=|b|, $\alpha = \beta = 90^o$, $\gamma = 60^o$).

Method	|a|	|c|	c/a	R_{OO}	r_{OH}	θ_{HOH}
BLYP	7.81	7.59	0.97	2.79	0.995	107.03
BLYP-D3(2b)	7.68	7.49	0.97	2.75	0.997	107.31
BLYP-D3(2b+3b)	7.69	7.49	0.97	2.75	0.997	107.29
BLYP-DCACP1	7.58	7.50	0.99	2.72	0.999	107.16
BLYP-DCACP2	7.68	7.47	0.97	2.75	0.998	107.20
Exp.[3b]	7.78	7.33	0.94	2.76	0.985	106.6±1.5

All functionals give greater values of the *c/a* ratio than the experimental value of 0.94216. Comparing the H-O-H angles after optimization, the performance ordering from the best to worst

is BLYP-D3(2b)≈BLYP-D3(2b+3b)> DCACP2-BLYP > DCACP-BLYP > BLYP, and the same ordering is observed in the prediction of the nearest neighboring oxygen-oxygen distance R_{OO}. Therefore, the inclusion of dispersion corrections in the BLYP exchange-correlation functional is essential for obtaining the correct water molecule geometry in ice Ih. Incorporating the three-body energy term in Grimmes' D3 scheme does not further improve the calculated geometry. The lattice dimension, however, was found to be less affected by the dispersion correction compared with the molecular geometry.

3.3.2 Cohesive energy

The cohesive energy E_{coh} is defined as the energy per molecule in forming a crystal from the vacuum. After removing the zero-point energy (ZPE), E_{coh} is given by:

$$E_{coh} = \frac{E^{ice} - N_{molecules} * E^{monomer}}{N_{molecules}} \qquad \text{Equation 3.1}$$

where in DFT calculations, E^{ice} and $E^{monomer}$ are Kohn-Sham energies of ice and of one water molecule. To take the zero-point vibrational energy into account, $E_{vib}^{monomer}$, defined under quasi-harmonic approximation (QHA)[59] as $\sum_i \frac{\hbar\omega_i}{2}$, needs to be subtracted, where ω_i are the phonon frequencies of mode *i*.

Table 3.2 The cohesive energies (kcal/mol per water), equilibrium volume V (Å^3/water) and their relative errors as comparing with experimental values, and density ρ (g/ml) from the 12-water hexagonal ice Ih cell using different DFT methods.

Method	$E_{cohesive}$	Error% of $E_{cohesive}$	V_0	Error% of V_0	ρ
BLYP	-12.47	11.35	34.72	8.32	1.08
BLYP-D3(2b)	-15.39	-9.42	32.71	2.05	1.01
BLYP-D3(2b+3b)	-15.25	-8.38	32.53	1.49	1.01
BLYP-DCACP1	-15.89	-12.96	31.54	-1.60	0.98
BLYP-DCACP2	-15.44	9.73	31.80	-0.78	0.98
Exp.[60]	-14.07	---	32.05	---	0.99

Table 3.2 tabulates the cohesive energies of ice Ih, obtained from different methods, with ZPE removed. Among the original and modified BLYP functionals, the Grimme's D3 correction with the three-body contributions to the interaction energy gave the best agreement with the experimental value of -14.067 kcal/mol per molecule, while the D3-correction that only involves the two-body interaction slightly overbinds by about 0.085 kcal/mol per water molecule. In **Table 3.2**, the relative errors in the calculated values of the cohesive energy are also reported. The magnitude of the relative errors of cohesive energy compared with the experimental value falls in the range of 9.0% to 13.4%. All the dispersion corrected BLYP functionals overestimate the cohesive energies of ice Ih.

Table 3.3 The cohesive energies (kcal/mol per water), equilibrium volume V (Å^3/water) and their relative errors as comparing with experimental values, and density ρ (g/ml) from the 64-water tetragonal ice VIII cell using different DFT methods.

Method	$E_{cohesive}$	Error% of $E_{cohesive}$	V_0	Error% of V_0	ρ
BLYP	-8.55	35.73	22.34	14.84	1.34
BLYP-D3(2b)	-15.60	-20.18	18.48	-4.99	1.62
BLYP-D3(2b+3b)	-15.68	-17.87	19.28	-0.87	1.55
Exp.[60]	13.30	---	19.45	---	1.66

For the high-density ice phase, as displayed in **Table 3.3**, the original BLYP functional correctly predicts that ice VIII is less stable than ice Ih, while BLYP-D3 gives the incorrect ordering. Furthermore, the percent of error in E_{coh} for ice VIII was increased by 2 times for each method compared with the percent of error in E_{coh} for ice Ih. This trend was observed in a previous study by Galli using PBE and vdW-DF on these two phases[49]. To clarify the change of vdW interactions upon compression of ice, and to enable quantifying the nature of intermolecular interactions of water molecules in different phases of ice with different densities, it would be interesting to calculate the percent of contribution from vdW interactions in the two phases of ice in the future.

3.3.3 Equilibrium volumes

The equilibrium volume V_0, which is a measure of the density of the phases, is another important property of ice to evaluate the performance of different theoretical methods. **Table 3.2** shows the

values of calculated V_0 in ice Ih using different DFT methods compared with experimental value. The results for high-density phase ice VIII from BLYP, BLYP-D3 and BLYP-D3(3b) are tabulated in **Table 3.3**. For the BLYP and BLYP-D3 methods, the error of the calculated values of V_0 of ice VIII was by about 2 times greater than that for ice Ih. However, adding three-body interaction energy contributions into BLYP-D3 reduced the error from 1.5% in ice Ih to 0.8% in ice VIII. In addition, both the BLYP-D3 and BLYP-D3(3b) functionals reverse the sign of error of V_0 and E_{coh} in ice VIII, which means the hydrogen bond environment in ice VIII is more sensitive to the dispersion force than in ice Ih.

3.3.4 Bulk modulus

Having observed the difference between the behaviors of these DFT methods for ice Ih and VIII, we further evaluate the performance of these functionals, by calculating their isothermal bulk modulus B_0, which is a measure of the dependence (or "resistance") of the system volume on the external pressure. In a second-order Taylor series around V_0, the energy can be expressed using the Birch-Murnaghan equation of state as[48]:

$$E_0(\mathrm{V}) = E_0(V_0) + \frac{B_0}{2V_0}(V\text{-}V_0)^2 \qquad \text{Equation 3.2}$$

where B_0 is the bulk modulus, omitting the vibrational correction, and the energy E_0 was obtained for each optimized structure by keeping the volume V fixed. It was shown by Pamuk and coworkers that this equation provides a good description of the E vs. V behavior of Ice Ih[48]. **Figure 3.5** plots the zero-pressure molecular volumes that minimize the Kohn-Sham cohesive energy E_{coh} in each method. These results were fit using **Equation 3.2** to obtain B_0, and the fitted quadratic curves are plotted together in **Figure 3.5,** with the expressions as well as calculated

values of B_0 listed in **Table 3.4.** For ice Ih, the original BLYP functional gives a value B_0 in close agreement with the experiment value of 13.8 GPa, and the role of dispersion correction is not clear in the prediction of the compressibility of ice Ih.

Figure 3.5 Cohesive energy per water molecule as a function of the molecular volume for ice Ih evaluated with different density functionals. (a) BLYP, (b) BLYP-D3, c) BLY-D3 (3b); (d) BLYP-DCACP1, (e) BLYP-DCACP2.

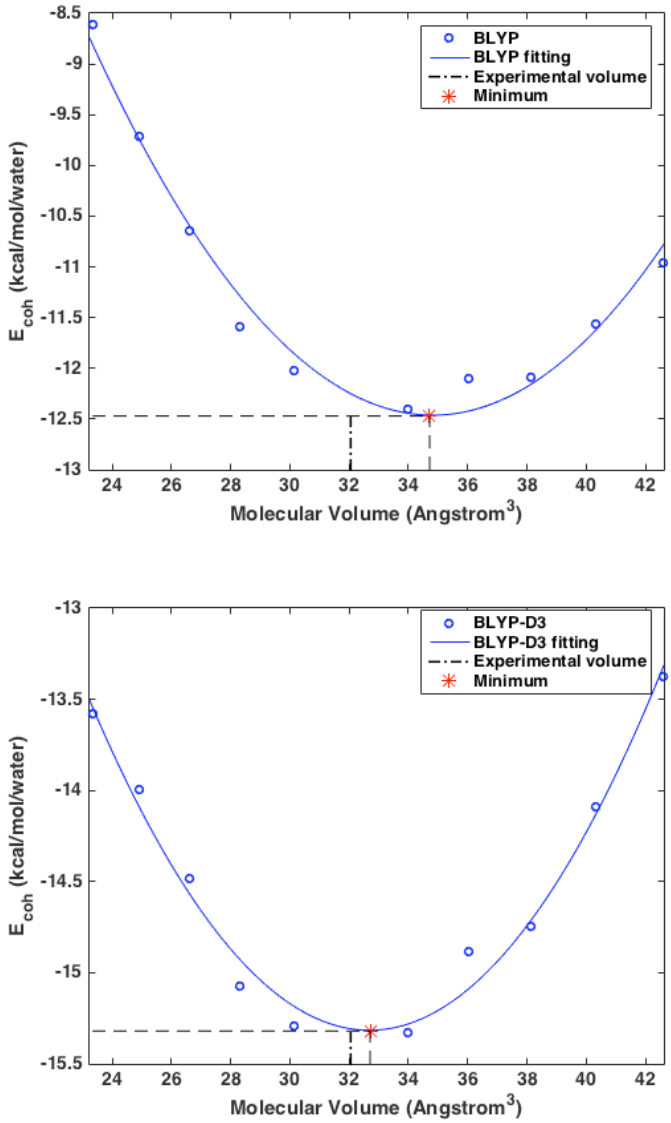

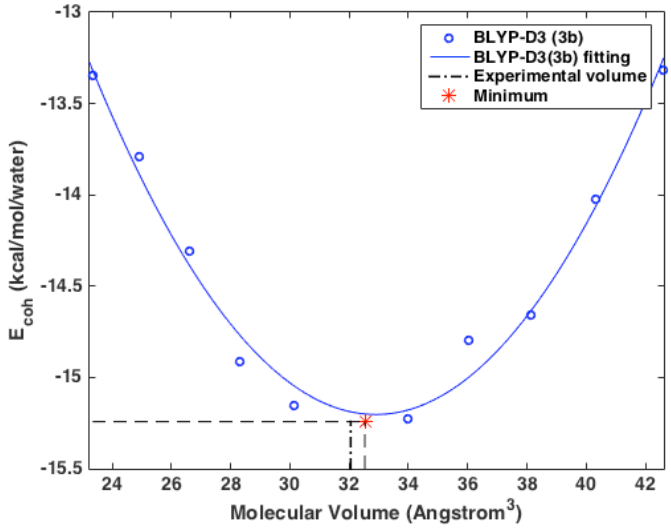
BLYP-D3 (3b)
BLYP-D3(3b) fitting
Experimental volume
Minimum
E_coh (kcal/mol/water)
Molecular Volume (Angstrom^3)
-13
-13.5
-14
-14.5
-15
-15.5
24
26
28
30
32
34
36
38
40
42

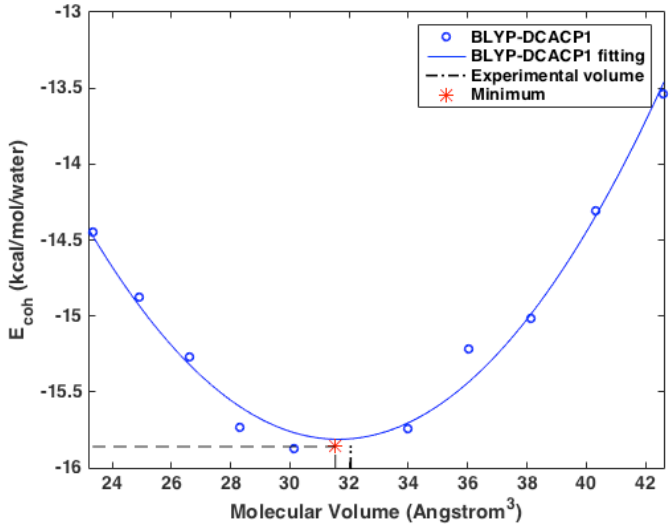
BLYP-DCACP1
BLYP-DCACP1 fitting
Experimental volume
Minimum
E_coh (kcal/mol/water)
Molecular Volume (Angstrom^3)
-13
-13.5
-14
-14.5
-15
-15.5
-16
24
26
28
30
32
34
36
38
40
42

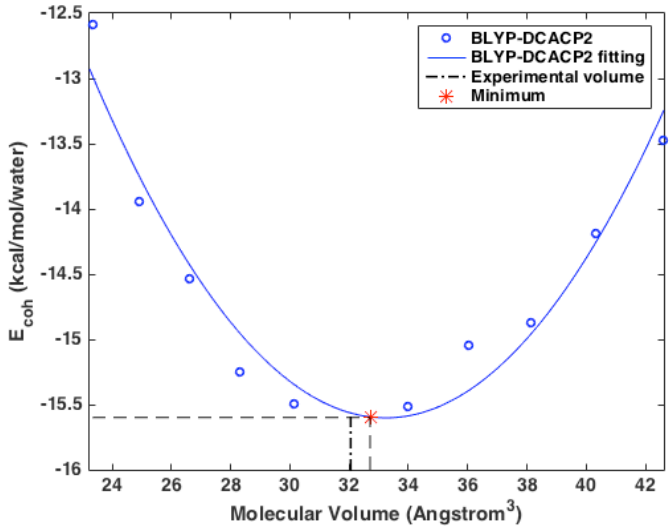

Table 3.4 The fitted curves using the second-order the Birch-Murnaghan equation of state and the calculated bulk modulus B_0 (in GPa) of the 12-water hexagonal ice Ih cell (in kcal/mol per molecule), the error bar of B_0 is displayed in the parenthesis (calculated from the error of the fitted curve).

Ice	Method	Fitted curve	B_0
Ih	BLYP	$0.0286V^2$-1.9857V + 21.99	13.8 (0.55)
Ih	BLYP-D3(2b)	$0.0212V^2$-1.3868V + 7.2875	9.6 (0.32)
Ih	BLYP-D3(2b+3b)	$0.024V^2$-1.5614V + 10.15	10.8 (0.32)
Ih	BLYP-DCACP1	$0.0215V^2$-1.3561V + 5.4938	9.4 (0.72)
Ih	BLYP-DCACP2	$0.0275V^2$-1.8281V + 14.713	12.2 (0.71)
Ih	Exp.[60]	---	13.8[61]

3.4 CONCLUSION

A detailed study of ice Ih and the high-density proton-ordered phase ice VIII was performed using the BLYP functional as well as several dispersion-corrected BLYP functionals. The properties considered include the monomer geometry, lattice structures, cohesive energies, equilibrium volumes, and bulk modulus. We have made the following conclusions:

1. The obtained optimized cell parameters of ice Ih and XI using different DFT functionals showed that dispersion-corrected BLYP functionals all gave greater values of HOH angles and shorter nearest O-O distance, resulting in stronger hydrogen bonds;
2. For the cohesive energy and equilibrium volumes, the overall performance of these functionals are: BLYP-D3 (2b+3b) > BLYP-D3(2b) ≈ DCACP2-BYLP > DCACP-BLYP > BLYP.
3. The original BLYP functional was able to accurately predict the bulk modulus of ice Ih, and adding dispersion corrections worsened agreement with experiment. It was not clear why this was the case.

4.0 ROLE OF DISPERSION ON THE PROPERTIES OF LIQUID WATER FROM AB INITIO MOLECULAR DYNAMICS SIMULATIONS

4.1 INTRODUCTION

Water is unquestionably the most common yet most unique liquid in the world. The directional hydrogen bonds in liquid water results in many anomalous properties of liquid water. Atomic simulations of liquid water have been performed with molecular mechanics (MM) force fields, or with DFT, in so-called *ab initio* molecular dynamics (AIMD). The MM force fields are parametrized by fitting to experimental or *ab initio* data, and they cannot capture the quantum nature of dispersion force, but simply include them in Lennard Jones pair potentials and electrostatic/Coulomb interactions in general. Also, force fields fail to describe processes where electronic degrees of freedom are important. AIMD simulations are an improvement over MM methods, and they can be performed by Born-Oppenheimer MD (BOMD)[62] approximation using density functional theory, in which the Kohn-Sham orbitals are optimized to the ground state self-consistently at every simulation time step; or by Car-Parinello MD (CPMD)[25] that includes the electrons as active degrees of freedom, via (fictitious) dynamical variables[38].

Over the years, researchers have carried out AIMD simulations of liquid water and ice using different statistical-mechanical ensembles and different system sizes to resolve the discrepancies in calculated thermodynamic properties compared with experimental data, such as

the radial distribution functions, self-diffusion coefficients, and vibrational properties. While MM simulations that can be carried out for 100 ps or longer, AIMD are limited to a timescale of 2-10 ps. A system size of 50-64 molecules is large enough to eliminate finite-system effects in the prediction of these structural properties such as RDFs in the simulation[63].

Pure GGA functionals give over-structured liquid water and makes water diffuse more slowly than experiment by one order of magnitude. Hybrid functionals with exact exchange only improve the predictions slightly[64]. This is probably due to the neglect of zero-point energy that "activate" the motion. Value of CPMD simulations with dispersion-corrected GGA functionals using different approaches such as Grimme's scheme or effective dispersion-corrected atom-centered potentials (DCACP) are more promising, especially the corrections to the BLYP functional[65]. Recently, our group has reported two-channel DCACP pseudopotentials: DCACP2 for correcting BLYP and PBE density functionals for long-range dispersion, and our cluster studies showed that binding energies of water dimer and hexamers were significantly improved compared to the one-channel DCACP approach[50]. As described in Chapter 4, the energetics and equilibrium volumes of ice Ih and VIII were also improved by the DCACP2 approach.

Therefore, I was wondering if the success of DCACP2 can be transferred from cluster and ice energetics to the thermodynamic properties of water, and we wanted to see if equivalent results can be achieved from BOMD simulations. I performed BOMD simulations of liquid water under ambient conditions, and treat the vdW interactions in BLYP functional by including either DCACPs or Grimmes' D3 correction scheme. Besides structural properties, i.e., radial and angular distribution functions and coordination number, and dynamical properties, e.g., mean-squared displacement, self-diffusion coefficients, orientational-autocorrelation functions of liquid water. I also calculated the dipole moment distributions of liquid water.

4.2 COMPUTATIONAL METHODS

The simulations in this study were carried out using the CP2K program utilizing Born-Oppenheimer MD with periodic boundary conditions with electronic ground state iteratively found in each step, and with the nuclei treated classically. The QUICKSTEP module in CP2K employs a Gaussian basis set for the orbitals while the auxiliary plane wave basis used for the electron density[66]. To represent core electrons, the norm-conserving Goedecker-Teter-Hutter pseudopotentials are used[58]. The plane wave cutoff was chosen to be 400 Ry, determined to be give converged results from AIMD of liquid water[67]. As noted in a previous AIMD study of liquid water, the basis set TZV2P (the Gaussian basis set with a triple-zeta valence basis set augmented with double (two sets) of d-type or p-type polarization functions) should be suitable for calculating the diffusivity of liquid water[67]. Therefore, we employed this basis set throughout this study. The convergence on the wave functions was 10^{-7} hartree. Calculations were performed with the generalized gradient approximation (GGA) functional BLYP[54], as well as the modified BLYP functional with different dispersion corrections: Grimmes' D3-correction scheme (BLYP-D3)[55], Dispersion-corrected-atom-centered potential (DCACP-BLYP)[56], and the two-channel version (DCACP2-BLYP)[50]. We refer to ref [56] and ref [50] for the parameters of DCACP and DCACP2, respectively.

I started with a cubic simulation box with 64 water molecules, with the cell dimension of 12.423 Å, formed using the Packmol[68] package. This keeps the density of the liquid water at 1.0 g/cm^3 during the canonical (NVT) ensemble simulations. It has been proven that 64 water molecules are sufficient to eliminate finite-size effects in simulations[69]. During the BOMD simulations, the nuclear equations of motion have been integrated using a standard velocity Verlet algorithm[32] with a 0.5 fs time step. For the calculations of dynamical properties (radial

distribution functions, dipole, and mean square displacements), the trajectories were stored every step. The temperature was adjusted by generalized Langevin equation (GLE) thermostats[70], which was shown to accelerate the convergence or properties. For all methods used in this study, the system was equilibrated under NVT ensemble for 10 ps, and then the production run for data collection was carried out for another 10 ps.

The self-diffusion coefficient D_s is calculated from the slope of the mean-square displacement (MSD) versus time using the Einstein diffusion equation[32]:

$$2tD_s = \frac{1}{n}\langle \Delta \boldsymbol{r}(t)^2 \rangle = \frac{1}{n}\langle |\boldsymbol{r}(t)\text{-}\boldsymbol{r}(0)|^2 \rangle \qquad \text{Equation 4.1}$$

where t is time, n is the dimensionality chosen to be 3, $r(t)$ is the position of a water molecule at time t, and $\Delta \boldsymbol{r}(t)$ is the displacement of a water molecule after time lag t. Least-squares fitting can be applied to estimate the slope.

The orientational relaxation time of liquid water used the definition proposed by Yeh and Mou[71] to describe how fast water molecules are changing their directions:

$$C_{\boldsymbol{u}}(\tau) = \langle P_2[\vec{u}(t_0) \cdot \vec{u}(t_0 + \tau)] \rangle \qquad \text{Equation 4.2}$$

where $P_2 = \frac{(3x^2\text{-}1)}{2}$ is the second-order Legendre polynomial, and $\vec{u}$ is the unit vector along HH,OH or dipole vector of a water molecule.

The dipole moment of system at time t $\vec{\mu}(t)$ is defined as the sum of molecular dipole moment of water $\vec{\mu}(t) = \sum_i \overrightarrow{\mu_i}(t)$, each calculated every step from the maximally-localized Wannier Function Center[72] as displayed in **Figure 4.1**.

For extracting information from trajectories, we used the TRAVIS analyzer[73].

Figure 4.1 Graphical representation of the Wannier Function Center (WFC) used for calculating the dipole moment of each water molecule, with the gray balls representing the positions of four Wannier centers and red-white stick representing two O-H covalent bonds in a water molecule.

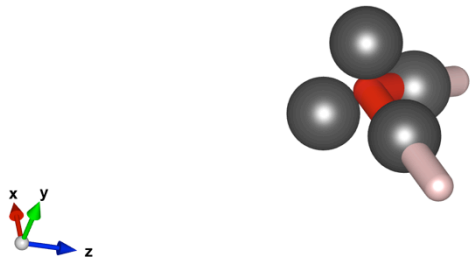

4.3 RESULTS AND DISCUSSION

4.3.1 Radial distribution functions

The radial distribution functions serve as a fingerprint of local structure in condensed phase of water. The oxygen-oxygen (g_{OO}), oxygen-hydrogen (g_{OH}), and hydrogen-hydrogen (g_{HH}) radial distribution functions obtained from the BLYP-based simulations are plotted in **Figure 4.2**. We are most interested in g_{OO}, since it is least sensitive to nuclear quantum effects, and some of characteristics from these RDFs are tabulated in **Table 4.1**.

Figure 4.2 Oxygen-Oxygen(g_{OO}), oxygen-hydrogen(g_{OH}), and hydrogen-hydrogen(g_{HH}) RDF of liquid water obtained from AIMD simulations with a 64-water box using BLYP, BLYP-D3, BLYP-DCACP1, BLYP-DCACP2 functionals.

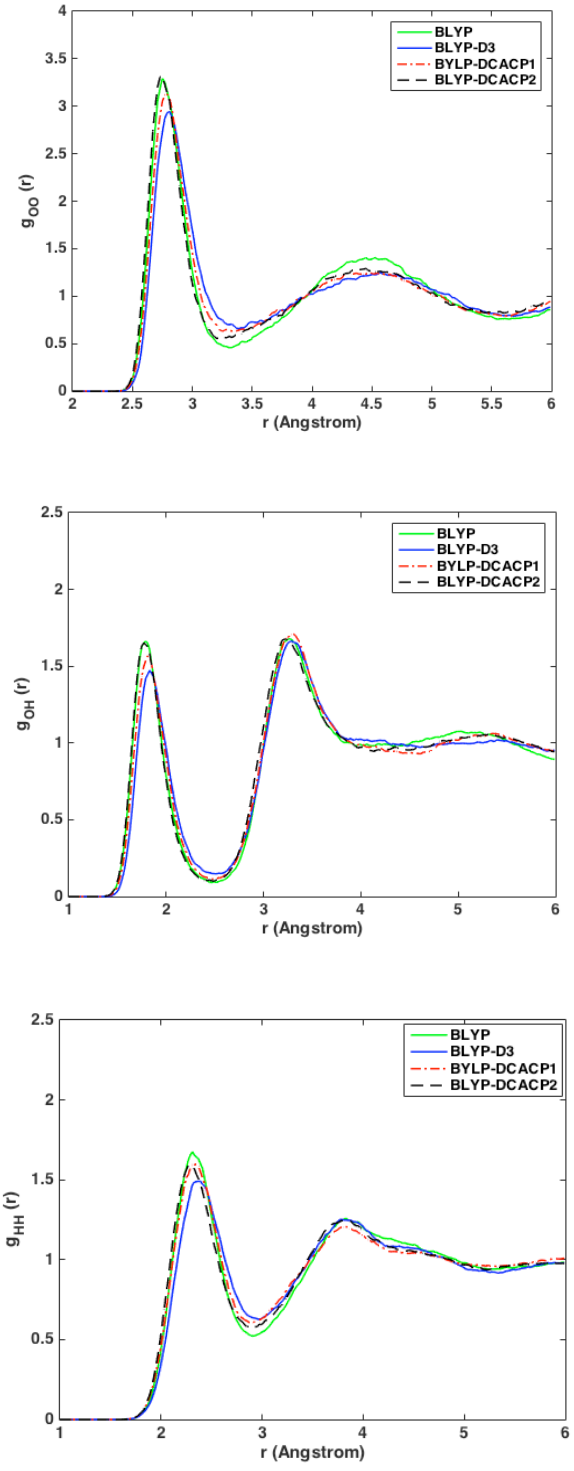

Table 4.1 Positions r (Å) and heights (g_{OO}) of the first peak and minimum of the Oxygen-oxygen radial distribution functions and the calculated coordination number n_{OO} (r) of liquid water from four BLYP-based methods from AIMD simulations of 10 ps at T=300 K, compared with the neutron scattering experimental data at T = 298 K.

Method	r_{max}	g_{OO}^{max}	r_{min}	g_{OO}^{min}	$n_{OO}(r)$
BLYP	2.75	3.29	3.31	0.46	4.12
BLYP-D3	2.81	2.93	3.39	0.66	4.54
BLYP-DCACP1	2.79	3.11	3.40	0.65	4.56
BLYP-DCACP2	2.77	3.23	3.21	0.55	4.02
Exp.[74]	2.74	2.76	3.39	0.79	4.6[75]

The vdW-corrected BLYP functionals including BLYP-D3 and BLYP-DCACP methods predict less structured liquid water than BLYP, with the positions of the first peak at around 2.8 Å shifting toward longer distance and with a lowering of the peak. DCACP2 gives almost no change for the first peak compared with the original BLYP curve, and it gets the higher first minimum compared with the BLYP curve, but not as much. From the first peak of BLYP-D3 and BYLP-DCACP, a longer oxygen-oxygen distance r_{OO} between the center molecule with the nearest neighbor molecule is observed. The looser structure from the vdW-corrected BLYP-D3 and DCACP2-BLYP simulations are also manifested in the increase of the local minimum of g_{OO} at around 3.3 Å. The second peak at around 4.5 Å, shows the r_{OO} between the center molecule and its second-coordinate shell water molecules. The DCACPs and D3-corrected BLYP functional gives the position of the second peak slightly further than the radius of pure BLYP water, indicating that the second shell is pushed outward from the vdW corrections. Overall, uncorrected BLYP water has a stronger first peak, and deeper first minimum with respect to the

neutron scattering data, and the dispersion corrected functionals give softer structures, and better reproduction of the experimental peaks of g_{OO}. The two-channel DCACP2 does not give better local structure of liquid water as seen from the oxygen-oxygen RDFs data.

For the oxygen-hydrogen RDF g_{OH}, as shown in **Figure 4.2 (b)**, the difference of the g_{OH} resulting from dispersion corrections are not as significant as shown in g_{OO}, but the first peak at around 1.87 Å which represents the hydrogen bonds are modified by dispersion correction. Both the D3 and the DCACP corrections shift the position of the first peak towards longer distance, as also observed in their first peak in g_{OO}. Their height of g_{OH} is also lower compared with the BLYP value. This indicates the formation of weaker hydrogen bonds in liquid water as described by the dispersion-corrected functionals.

4.3.2 Coordination numbers and H-bond analysis

To further characterize the local structure in liquid water, we calculated the coordination number $n_{ij}(r)$, obtained by integrating g_{OO} up to the first minimum r_{min} of g_{OO}:

$$n_{ij}(r) = 4\pi\rho \int_0^{r_{min}} r^2 g_{ij}(r) dr \qquad \text{Equation 4.3}$$

As tabulated in **Table 4.1**, the BLYP-D3 and DCACP-BLYP methods give higher values of the average coordination number, in good agreement with the experimental $n_{OO}(r)$= 4.6 up to r_{min} =3.4 Å, and $n_{OO}(r)$= 4.3 up to r_{min} =3.3 Å by Skinner and coworkers[75]. Adding one more channel to the DCACP, however, worsens the results. The coordination number of 4.02 from DCACP2 method resemble an ice-like structure, where each water molecule is tetra-coordination: each oxygen atom is covalently bonded with two hydrogen atoms, and form hydrogen bonds with two other hydrogen atoms.

Figure 4.3 Snapshots of penta-coordinated water molecules taken from the trajectory of AIMD simulations using the BLYP-D3 functional. The fifth water molecule in the first coordination shell stays non-hydrogen-bonded.

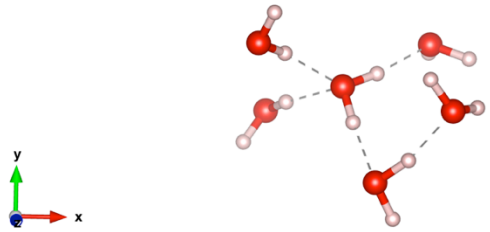

In **Figure 4.3**, we show snapshots of such penta-coordinated water molecules from the BLYP-D3 simulations. Besides the two-covalently bonded and two hydrogen-bonded water molecules, the fifth coordinated water molecule is non-hydrogen-bonded to the center water molecule. The occurrence of the fifth molecule at 3.0 Å < R_{OO} <4.0 Å, does not show up in ice Ih, since there are no neighbors for tetra-coordinated water throughout this region. The higher coordination number of water is related with the phenomenon of cross-shell penetration (CSP)[76], an effect that occurs by collapse of the second shell into the region of the first shell, especially when external pressure is raised, without significant breaking of H-bonds. This give rise to the higher coordination numbers of molecules liquid water, as compared with the tetra-coordinated water in ice Ih. A higher coordination number explains the higher density of liquid water compared with that of ice Ih. Therefore, the prediction of values of $n_{oo}(r)$ from the BLYP-D3 and DCACP-BLYP are consistent with the high-density of liquid water. CSP is also crucial in liquid water's diffusion behavior[38], which requires molecules to cross the region 3.0 < R_{OO} < 4.0 Å. The correlation between CSP and diffusion will be expanded in the next future sections.

4.3.3 Orientational self-correlation

The rotational dynamics of liquid water can be characterized by the orientational auto-correlation function given by **Equation 4.2**. The direction of a water molecule is chosen to be that of its dipole vector. In **Table 4.2**, we show the values for the time constants together with the experimental times[77] at T = 300 K. The predicted value of the second order relaxation time $\tau_{l=2}$ from the BLYP method is slower by about 56% compared with experimental relaxation time of 1.92 ps. I expect that the trend of the time constants be consistent with the radial distribution functions: pure BLYP functional gives "harder" structures from RDFs, and it also gives higher values of time constant for water reorientation, leading to slower rotation dynamics. On contrary, vdW-corrected BLYP functionals give rise to faster water rotations.

Table 4.2 Time constants τ (ps) of liquid water from orientational autocorrelation function predicted by AIMD simulations using different functionals at T = 300 K.

Method	$\tau_{l=2}$
BLYP	3.00
BLYP-DCACP1[a]	1.71
Exp.[77]	1.92

[a]Value taken from reference[65];

4.3.4 Self-diffusion coefficient

Whereas the RDFs are characteristics of time-averaged local structures, the self-diffusion coefficient D_s is an important dynamical property to describe the diffusion mobility of water molecules. In computer simulations, either the Green-Kubo method or the Einstein method can

be used to obtain D_s. In the Green-Kubo method, D_s is calculated from the integral of velocity auto-correlation function to infinite time. In the Einstein method, D_s is the 1/6 of the slope of mean-square displacement (MSD) versus time curve. The two methods should give consistent results, and we employ the Einstein method in our calculations, following computational methods stated in section 7.2. In **Figure 4.4**, we plot the MSD versus time curves from the four methods at T = 300 K. MSD from pure BLYP functional is considerably smaller whereas BLYP-D3 and BLYP-DCACPs gives about 2-fold to 2.5 fold improvement, although still smaller than the experimental curve. The corresponding D_s values are tabulated in **Table 4.3**, with all calculated values being smaller than the experimental value of 0.23 $Å^2/ps$. Based on the relaxation time scale of hydrogen bonds (as fast as ~1.0 ps) in liquid water as calculated in section 4.3.3, the diffusion of water involves frequent cross-shell penetration, or the reorientation of hydrogen bonds.

Figure 4.4 MSDs as obtained for AIMD simulations with the BLYP-D3, PBE-D3, BLYP-DCACP1, BLYP-DCACP2 functionals at T = 300 K indicated by solid, dotted, dashed, and long dashed lines, respectively.

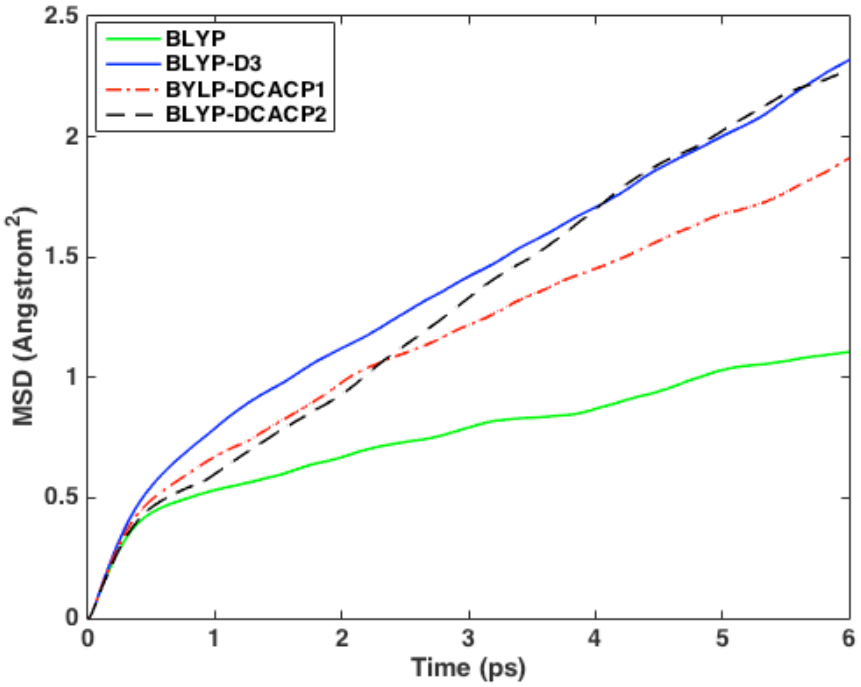

Table 4.3 Calculated self-diffusion coefficients D_s of liquid water, in $Å^2$/ps from an AIMD simulation of 10 ps at T = 300 K.

Method	D_s
BLYP[a]	0.0186
BLYP-D3[a]	0.05
BLYP-DCACP1[a]	0.054
BLYP-DCACP1[b]	0.15
BLYP-DCACP2[a]	0.056
Exp.[c]	0.23

[a]Simulations carried out at T = 300K.
[b]Value taken from reference[65], and simulations of the liquid water were carried out under NVE ensemble with hydrogen replaced by deuterium of mass=2.0 amu, the average temperature during the simulation was 308 K.
[e]Experimental measurement carried out at T =298 K.

As noted by Gillan and coworkers that the value of D_s correlates with the height of $g_{OO}(r)$ at the first minimum: g_{OO}^{min} [38]. This is also observed in my study. The experimental $g_{OO}(r)$ minimum g_{OO}^{min} at ambient condition (at Roo = 3.4 Å) is 0.79, and this gives the D_s of 0.23 $Å^2/ps$. The pure BLYP functional give the smallest value of g_{OO}^{min}: 0.46, and it also predict the smallest value of D_s. When dispersion corrections are added, the g_{OO}^{min} is increased, and liquid water is more diffusive as predicted from the dispersion-corrected methods, compared with the BLYP results. In our study, the improvement afforded by DCACP-BLYP is not as much as the a previous calculation of D_s using BLYP-DCACP[65]. Therefore, besides the conclusion that dispersion corrections give better description of the dynamical properties of liquid water at ambient conditions, it is also possible that protonic quantum effects play a significant role under this temperature. This may explain the difference between our results using DCACP-BLYP and a higher value obtained by Lin and coworkers that use deuterated hydrogen for the DCACP-BLYP method[65].

4.3.5 Distribution of molecular dipole moment

The value of dipole moment of a water molecule in the liquid phase has long been controversial, since there is no method to measure it directly. Accurate theoretical predictions are therefore quite helpful, and previously reported values from calculations ranged from 2.6 to 3.0 D[78], either using QM or MM methods. Based on an x-ray measurement of the structure factor for water, Badyal and coworkers suggested the dipole moment of a liquid-phase water molecule to be 2.9±0.6 D[79]. In **Figure 7.10**, we presented the distributions of the total dipole moment of the water molecules in the liquid phase from the four BLYP-based methods. Pure BLYP water gives a distribution centered at 3.23 D, spanning from 1.44 to 5.52 Debye. After correcting for

dispersion forces, both BLYP-D3 and DCACP-BLYP methods give smaller average value of 3.04 D. However, BLYP-D3 gives a wider distribution of 4.07 D, comparing with the range of 3.62 D from DCACP-BLYP method, owing to the larger monomer geometry fluctuation. DCACP2-BLYP method gives a sharper distribution with mean value of 3.11 D, therefore only slightly improving the value of average molecular dipole moment of liquid water.

Table 4.4 Statistics of molecular dipole moment μ (in Debye) of liquid water from AIMD simulations at T = 300 K, using BLYP, BLYP-D3, BLYP-DCACP1 and BLYP-DCACP2 functionals, comparing with an experimental value at T = 300 K from X-ray diffraction measurement[79].

Method	Mean	Stdev	Min	Max
BLYP	3.23	0.334	1.44	5.52
BLYP-D3	3.04	0.337	1.35	5.42
BLYP-DCACP1	3.04	0.309	1.62	5.24
BLYP-DCACP2	3.11	0.270	2.04	4.44
Exp.[79]	2.9	0.6		

Figure 4.5 Distribution of molecular dipole moment of liquid water obtained from AIMD simulations using a 64-water cubic box with density of 1.0 g/cm3, with the BLYP-D3, BLYP-DCACP1 and BLYP-DCACP2 functionals.

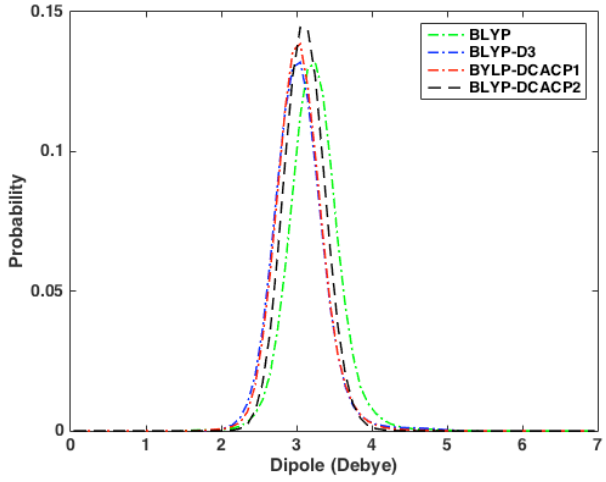

As the DCACPs do not affect the electronic structure, including multipoles of the monomers[56], the improvement of molecular dipole moment comes from the influence on the liquid water structure from the DCACPs. All the values are greater than the experimental value, consistent with the overestimation of polarizability by semi-local density functionals, which is not eliminated by dispersion corrections. Indeed, in a previous study of ice Ih, the molecular dipole of water molecules from D3-corrected and original GGA functionals were in qualitative agreement[69]. Furthermore, comparing with predictions of 2.67 D from a recent SCS-MP2/aug-cc-pvDZ BOMD simulation[80], the experimental value 2.9 D seems overestimated.

4.4 CONCLUSION

To summarize, I have carried out BOMD simulations of liquid water at ambient conditions under canonical ensemble, using density functional theory with the GGA BLYP functional. The empirical DCACPs approach, and Grimmes' vdW corrections based on pairwise-potential are employed to correct for the BLYP functional that fails to describe the dispersion force.

The radial distribution functions of liquid are improved by including vdW corrections. The predicted value of the height of the first minimum in $g_{OO}(r)$ are correlated with the calculated self-diffusion coefficient. This is consistent with previous observations. VdW-corrected functionals also give higher average coordination number $n_{OO}(r)$, that are related with the higher density of liquid water compared with that of tetra-coordinated ice Ih. The over-polarization of GGA functional which leads to higher molecular dipole moment of water in the liquid, is only slightly improved by including vdW corrections.

Future studies calculating the role of nuclear quantum effects (NQE) and tunneling in hydrogen bond of liquid water and ice Ih, from AIMD simulations using these dispersion-corrected functionals would be quite helpful. It is desirable to assess these functionals on their accuracy for describing both liquid water and small clusters.

5.0 CORRECTING FOR DISPERSION WITH PSEUDOPOTENTIALS FOR INERT GAS DIMERS

5.1 INTRODUCTION

5.1.1 Dispersion corrections in DFT

The London dispersion force arises from long-range correlated charge fluctuations between electrons. It plays a critical role in intermolecular interactions, such as the adsorption of molecules on surfaces (physisorption), the cohesion of solids and liquids, and in establishing the tertiary and quaternary structures of biomolecules[81]. Kohn-Sham density functional theory (DFT) serves as a popular method to study the electronic structure of many-electron systems since it provides a good balance between the accuracy and computational cost. However, the C_6R^{-6} asymptotic behavior of long-range dispersion energies is not described by local and semi-local approximations in DFT. Many strategies have been suggested to overcome this shortcoming[55, 82]. Roughly, these methods can be classified into three categories:

1) vdW-DF methods.

These methods incorporate the long-range correlation interactions $E_C^{non\text{-}local}$ via a non-local correlation kernel $\Phi(\boldsymbol{r}, \boldsymbol{r}')$ and integrate over the electron densities at two points ($\boldsymbol{r}$ and $\boldsymbol{r}'$) as shown in Equation 5.1[82m, 83]:

$$E_C^{non\text{-}local} = \iint \rho(\boldsymbol{r})\Phi(\boldsymbol{r},\boldsymbol{r}')\rho(\boldsymbol{r}')d\boldsymbol{r}d\boldsymbol{r}' \qquad \text{Equation 5.1}$$

The vdW-DF non-local functionals represent the exchange-correlation energy (E_{xc}) functional as

$$E_{xc}[\rho] = E_x^{GGA} + E_c^{LDA} + E_C^{non\text{-}local} \qquad \text{Equation 5.2}$$

where E_x^{GGA} represents the exchange energy from a GGA functional, E_c^{LDA} represents the short-range correlation energy from an LDA functional. The non-local correlation kernel $\Phi(\boldsymbol{r},\boldsymbol{r}')$ is a functional of the density and its gradient (vdW-DF2). The downside of vdW-DF functionals is that they are computationally expensive.

2) DFT+D methods.

These methods add atom-atom $C_6^{ij}R_{ij}^{-6}$ (and possibly also $C_8^{ij}R_{ij}^{-8}$) corrections to the DFT energy. The most recognized such procedure is the DFT-D scheme being that of Grimme[55, 82e, 82h, 84]. In DFT+D methods, the total KS energy from an exchange-correlation functional is augmented with a simple dispersion correction in the form of

$$E_{disp} = -s_6 \sum_{i=1}^{N-1}\sum_{j=i+1}^{N}(C_6^{ij}R_{ij}^{-6})f_d(R_{ij}) \qquad \text{Equation 5.3}$$

where N is the number of atoms, R_{ij} is the distance between atom i and atom j, C_6^{ij} are pairwise dispersion coefficients, f_d is a damping function to avoid the divergence of dispersion energy at short range, and s_6 is a global scaling factor depending on the density functional used. Besides this, Tkatchenko and coworkers' vdW-TS scheme employs the environment dependent C_6^{ij} terms evaluated from reference atomic polarizabilities and reference atomic C_6 coefficients[82j]:

$$C_6^{AB} = \frac{2C_6^{AA}C_6^{BB}}{\left[\frac{\alpha_B^0}{\alpha_A^0}C_6^{AA} + \frac{\alpha_A^0}{\alpha_B^0}C_6^{BB}\right]} \qquad \text{Equation 5.4}$$

The free-atom reference values of α_A^0 and C_6^{AA} are taken from a self-interaction corrected time-dependent DFT (TDDFT) calculations of Chu and coworkers[85]. Their recent fully self-consistent implementation was shown to affect molecular multipoles for polarizable fragments[86].

3) Atom-centered potential-based methods (DCACP).

These methods correct the long-range electron density by use of atom-centered pseudopotentials. This approach was initiated by Rothlisberger and co-workers[56, 87], using atom-centered potentials calibrated against MP2 binding energies to describe effects of dispersion in DFT calculations using GGA functionals. The original implementation of the DCACP method employed a single angular momentum channel (generally the $l = 3$ channel) and was implemented for the PBE[88], BLYP[54] and Becke-Perdew[89] functionals. Although the approach has proven to be quite successful at predicting equilibrium geometries and binding energies for a wide range of weakly bound complexes, the energy correction due to the inclusion of DCACPs falls off much faster than R^{-6} at large distances[56, 87a].

5.1.2 Multi-channel DCACP

The DCACP approach was extended to use more than one angular momentum channel by Tarvernelli and coworkers in 2009[90]. Their results showed for the case of $(H_2)_2$ that the large R behavior of DCACP calculations can be vastly improved by employing three angular momentum channels (*p, d* and *f*) rather than one. More recently, our group introduced for both BLYP and PBE functionals two channel (*d* and *f*) DCACPs for C, N and O atoms, as well as for H[50]. These were referred to as DCACP2 potentials and were demonstrated to give significantly improved interaction potentials for the S22x5 set[91] of dimers compared to the results of one-channel DCACP calculations, therefore motivating the study in this paper.

The DCACP2 potential are implemented via the non-local part of the Goedecker-Teter-Hutter (GTH) pseudopotentials[58] as is the case for the original DCACP potential:

$$Y_l^{(nl)}(\boldsymbol{r},\boldsymbol{r}') = \sum_{m=-l}^{+l} Y_{lm}(\hat{\boldsymbol{r}}) p_l(r;\sigma_2)\sigma_1 p_l(r';\sigma_2) Y_{lm}^*(\hat{\boldsymbol{r}'})$$ Equation 5.5

In Equation 6.3, Y_{lm} denotes a spherical harmonic, and p_l is a normalized projector onto the space of each angular moment l defined as

$$p_l(r;\sigma_2) \propto r^l e^{-\frac{r^2}{2\sigma_2^2}}$$ Equation 5.6

The parameter σ_1 scales the amplitude of the pseudopotential, and σ_2 controls the location of the projector's maximum from the atomic center.

In this paper, the DCACP2 method when used with the BLYP functional is parameterized to describe the two-body interaction energies of He, Ne and Ar. The charge density distortions of the rare-gas dimers induced by the DCACP2 potential were examined at long separations. We also calculated the atomic dipole moment induced by DCACP2, and it compared it with the dispersion dipole moment of two interacting Drude oscillators parametrized to Ar recently studied in our group[92]. Finally, for investigating the origin of the success of the DCACP2 method, analysis of the interaction energy of Ar_2 was performed.

5.2 COMPUTATIONAL METHODS

5.2.1 Setup for CP2K calculations

The DFT calculations used in the fitting and testing of the DCACP2 method were carried out using the CP2K 2.6/QUICKSTEP program[66, 82l]. The hybrid Gaussian and plane-wave (GPW) approach implemented in CP2K was employed for all calculations in this study. In this approach, the Kohn-Sham orbitals were expanded in Gaussian-type functions, and an augmented plane-

wave-type approach was used to represent the electronic density[93]. Corrections for basis set superposition error (BSSE) were applied using the Boys and Bernardi counterpoise procedure[94] to the two-body interaction energies. The DFT calculations used the GTH pseudopotentials reported in ref [58]. The calculations used the Gaussian quadruple-ξ valence QZV3P basis sets[57] generated for use with the GTH pseudopotential, augmented by three polarization functions taken from the all-electron correlation-consistent cc-pVQZ basis set of Dunning[95]. The supplemenetal polarization functions were chosen as the lowest angular momentum not occupied by the atom (p-channel for helium and d-channel for neon and argon). Then, a set of diffuse functions taken from aug-cc-pVQZ basis set were added. The diffuse functions of *s*, *p*, and *d* channels were chosen for helium and argon, and of *d* channel was chosen for neon, as used in the original Dunning basis set[95].

The calculations on the helium and neon dimers were carried out in a box of *10*10*15* $Å^3$, and for the argon dimer the box was *10*10*25* $Å^3$ with the two atoms locating symmetrically with respect to the center of the box along the z-axis. The threshold for the SCF convergence was chosen to be 10^{-9} Hartree. The plane wave cutoff E_{cut} was chosen to be 2000 Rydberg to guarantee convergence of the energy. The convergence of the interaction energies with respect to box sizes and cutoffs was confirmed. The dimer systems were computed under non-periodic conditions, and the reciprocal space-based method by Martyna and Tuckerman[96] was used for solving the Poisson equation when treating the long-range forces in the molecules.

5.2.2 DFT-SAPT calculations

The symmetry-adapted intermolecular perturbation theory interaction energy using density functional theory orbitals (DFT-SAPT)[97] interaction energy is decomposed into separate terms defined by various physical effects:

$$E_{int}^{SAPT} = E_{pol}^{(1)} + E_{exch}^{(1)} + E_{ind}^{(2)} + E_{exch-ind}^{(2)} + E_{disp}^{(2)} + E_{exch-disp}^{(2)} + \delta(HF) \quad \text{Equation 5.7}$$

where $E_{pol}^{(1)}$ and $E_{exch}^{(1)}$ are the first-order electrostatic and exchange energies, $E_{ind}^{(2)}$ and $E_{disp}^{(2)}$ are the second-order induction and dispersion energies, $E_{exch-ind}^{(2)}$ and $E_{exch-disp}^{(2)}$ are their exchange counterparts[98]. Higher order induction interactions are described by $\delta(HF)$. The second-order DFT-SAPT calculations were carried out using the MOLPRO[99] program version 2012.1. The calculations use the aug-cc-pVQZ basis set. Density-fitting (DF) using Weigend's cc-pVQZ JK-fitting basis set[100] was employed for the first-order terms, the induction as well as the exchange-induction contributions. For the dispersion and exchange-dispersion contributions, Weigend and co-worker's aug-cc-pVTZ MP2-fitting basis set[101] was used.

5.2.3 Parametrization of DCACP2-BLYP

In determining the parameters in the DCACP2-BLYP potentials, the potential energy curves of the homonuclear dimers were fit to interaction energies at several bond lengths from CCSD(T)[102] calculations. For the parametrization, the genetic algorithm (GA)[103] was implemented. GA is a heuristic solution-search technique, that evolves a best set of parameters by mimicking the process of natural selection[103b]. We chose to use GA because the optimization of the parameter set involving four parameters ($\{\sigma_1(l=2), \sigma_2(l=2), \sigma_1(l=3), \sigma_2(l=3)\}$ implies multiple

possible local minima, and the genetic operations (mutations and crossover) in GA sometimes led to a different local minima, therefore helping search a wider range of space on the 4-dimensional grid. When converged result is achieved, the following fitness function along the one-dimensional potential-energy surface (PES) is minimized:

$$\text{fitness} = \sum_{i=1}^{N} \left[\frac{BE_i^{DCACP2-BLYP} - BE_i^{CCSD(T)}}{BE_i^{CCSD(T)}} \right] \qquad \text{Equation 5.8}$$

where N_j is the number of data points associated with each interaction energy in the fitting set, and M is the number of entries in the fitting set. A flowchart describing the sequence of steps employed in this work for optimization of parameters in DCACP2-BLYP functional is depicted in **Figure 5.1.** For the optimization of DCACP2-BLYP parameters of these dimers, it took around 20 generations to achieve converged results.

The reference CCSD(T) calculations were carried out with the aug-cc-pV5Z basis set[95, 104] using the MOLPRO program[99]. The optimization of the DCACP2-BLYP parameters was carried out in the CP2K 2.6/Quickstep program[105]. All optimizations were performed using a set of Python scripts that handle job submissions and data processing.

Figure 5.1 Flowchart describing the sequence of steps employed in this work for optimization of DCACP2-BLYP parameters.

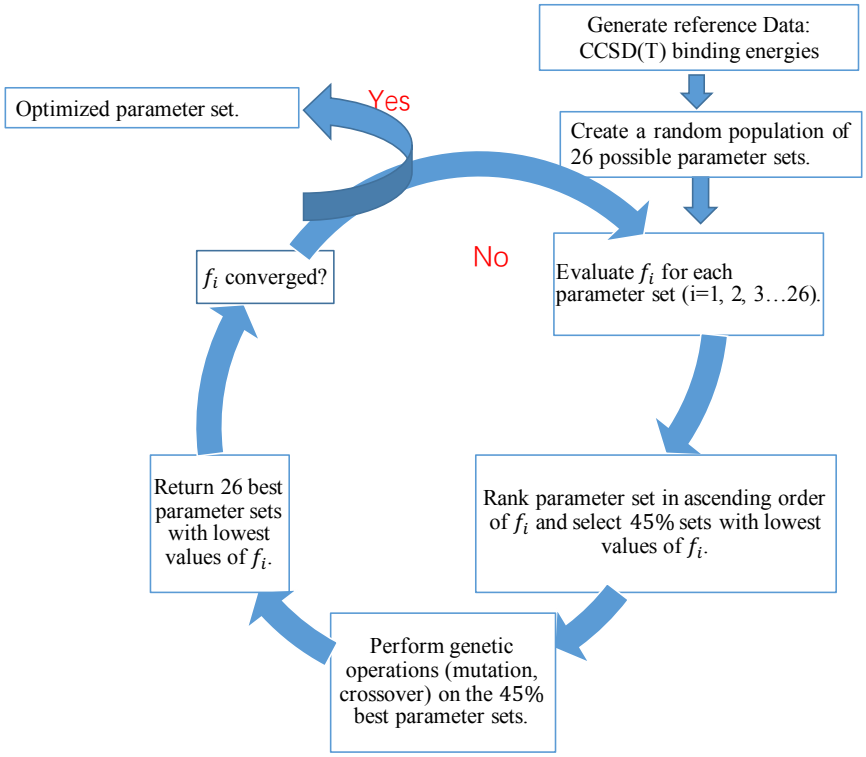

5.3 RESULTS AND DISCUSSIONS

5.3.1 Optimized DCACP2-BLYP parameters

For He_2 and Ar_2, the DCACP2 potentials were fit to CCSD(T) interaction energies at distances from 0.8*equilibrium distances (R_{eq}) to $2.0*R_{eq}$ in steps of 0.2 Å. In the case of Ne_2, difficulty was encountered in converging the optimization using the genetic algorithm, and the parameters in the DCACP2 were determined from a 4-dimensional grid of the four parameters. In this case, the fitting was to CCSD(T) interaction energies at $1.0*R_{eq}$, $1.5*R_{eq}$ and $2.0*R_{eq}$. The parameters

generated for helium, neon and argon for use with the GGA functional BLYP are listed in **Table 5.1**, and the corresponding parameters for the original single-channel DCACP are given in **Table 5.2,** for comparison.

Table 5.1 DCACP2-BLYP parameters in atomic units.

Channels	σ_1 [10^{-4}]	σ_2
$He_{l=2}$	-0.487	7.726
$He_{l=3}$	-3.975	2.368
$Ne_{l=2}$	-6.600	2.728
$Ne_{l=3}$	-2.400	3.400
$Ar_{l=2}$	-3.776	4.820
$Ar_{l=3}$	-13.084	2.590

Table 5.2 DCACP-BLYP parameters in atomic units[56].

	σ_1 [10^{-4}]	σ_2
He	-3.916	2.395
Ne	-6.412	2.481
Ar	-12.960	2.775

The radial terms in the DCACPs are plotted in the form of $-|\sigma_1|^{\frac{1}{2}}p_l(r)$ in **Figure 5.2**. Compared with the single-channel DCACP ($l = 3$) parameters, the addition of the $l=2$ channel in DCACP2 causes the potential to decay more slowly as R increases.

Figure 5.2 Plot of the radial terms-$|\sigma_1|^{\frac{1}{2}}p_l(r)$ of the DCACP-BLYP and DCACP2-BLYP methods for the argon dimer.

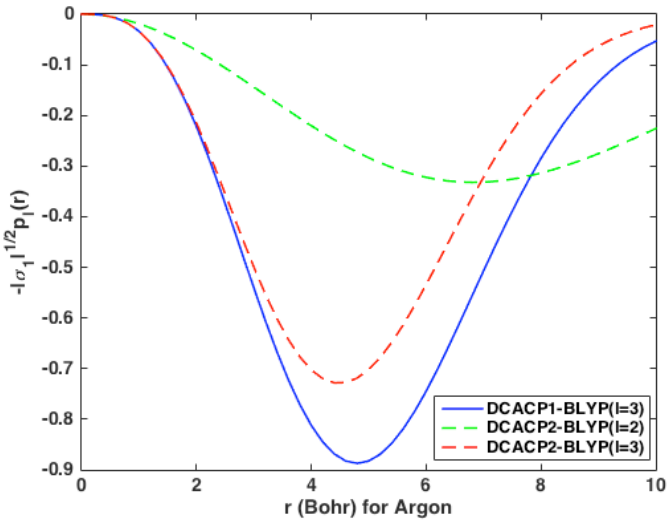

5.3.2 Binding energy curves for dimers

The improvements afforded by the DCACP2-BLYP method for the three homonuclear dimers used in the fitting of pseudopotentials is illustrated in **Figures 5.3**, **5.3** and **5.4.** As a comparison, the equilibrium bond lengths R_{eq} and binding energies at the equilibrium distances E_{min} from different methods are also tabulated in **Table 5.3**.

Figure 5.3 Interaction energy of the argon dimer as function of the interatomic distance

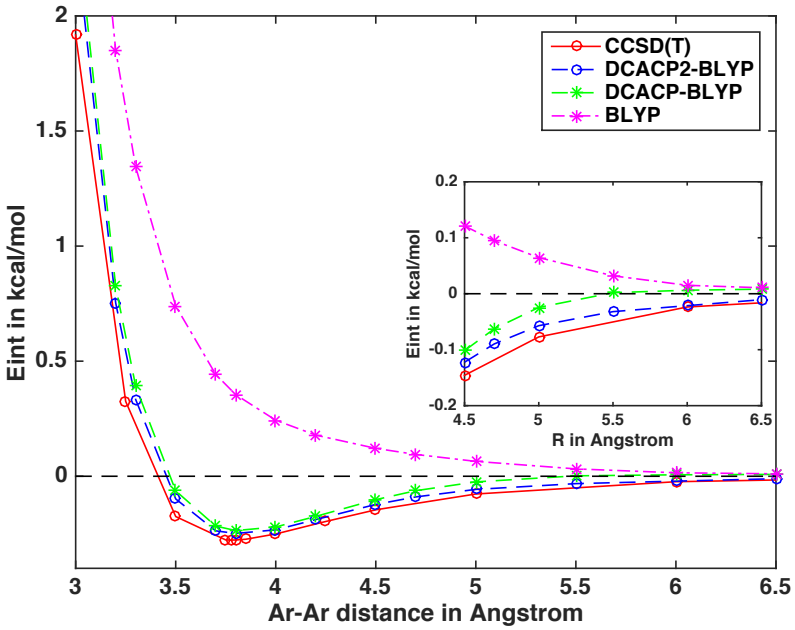

Figure 5.4 Interaction energy of the helium dimer as function of the interatomic distance.

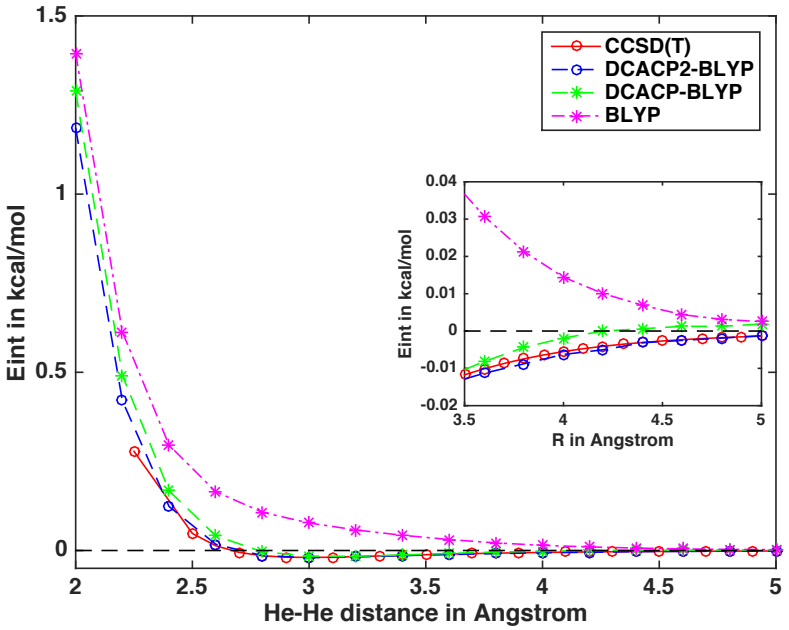

Figure 5.5 Interaction energy of the neon dimer as function of the interatomic distance.

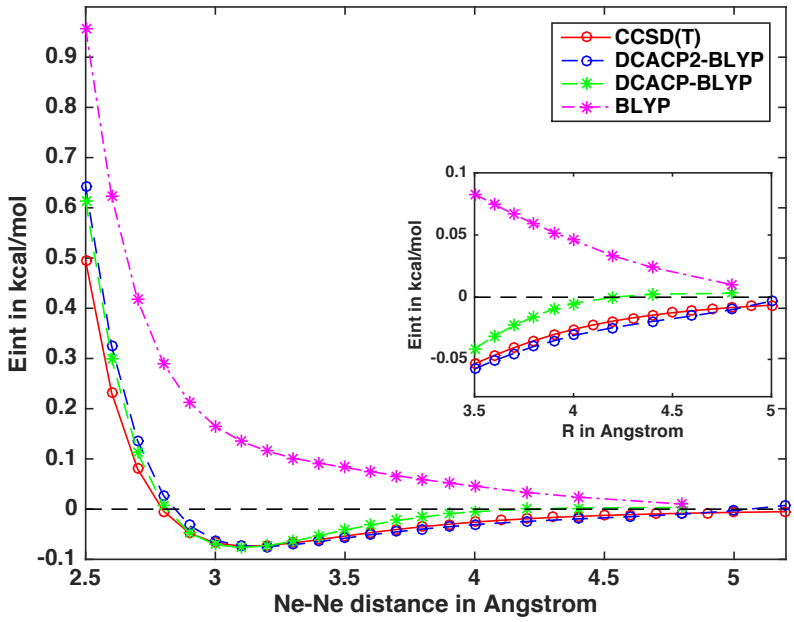

Table 5.3 Bond-lengths R_{eq} (in Å) and binding energies E_{min} (in kcal/mol) of rare gas dimers.

Method	He_2		Ne_2		Ar_2		HeNe		HeAr		NeAr	
	E_{min}	R_{eq}	E_{min}	R_{eq}	E_{min}	R_{eq}	E_{min}	R_{eq}	E_{min}	R_{eq}	E_{min}	R_{eq}
Reference	0.020	3.00	0.082	3.20	0.249	3.80	0.041	3.03	0.057	3.48	0.134	3.49
PBE	0.073	2.75	0.111	3.11	0.127	4.00	0.095	2.94	0.085	3.44	0.125	3.55
BLYP	--	--	--	--	--	--	--	--	--	--	--	--
DCACP-BLYP	0.017	3.08	0.076	3.10	0.237	3.85	0.040	3.05	0.072	3.45	0.123	3.48
DCACP-PBE	0.019	3.05	0.070	3.18	0.239	3.83	0.039	3.10	0.080	3.45	0.137	3.50
DCACP2-BLYP	0.020	3.00	0.082	3.15	0.248	3.80	0.034	3.10	0.060	3.50	0.170	3.48

The potential energy curves calculated using the DCACP2-BLYP method more closely reproduce those from the CCSD(T) calculation than do those obtained using the original DCACP approach. Particularly noticeable is the improvement at distances between ~ R_{eq} and 1.5*R_{eq}.

In order to assess the transferability of the DCACP2-BLYP potential to mixed inert gas dimers, we calculated the binding energy curves for the three heteronuclear dimers, displaying the results in **Figures 5.6, 5.6 and 5.7**. As in the homonuclear dimers, the DCACP2-BLYP method more closely reproduces the CCSD(T) curves of the helium-neon, helium-argon and neon-argon at longer distances than does the DCACP-BLYP method.

Figure 5.6 Interaction energy of the helium-neon dimer as function of the interatomic distance.

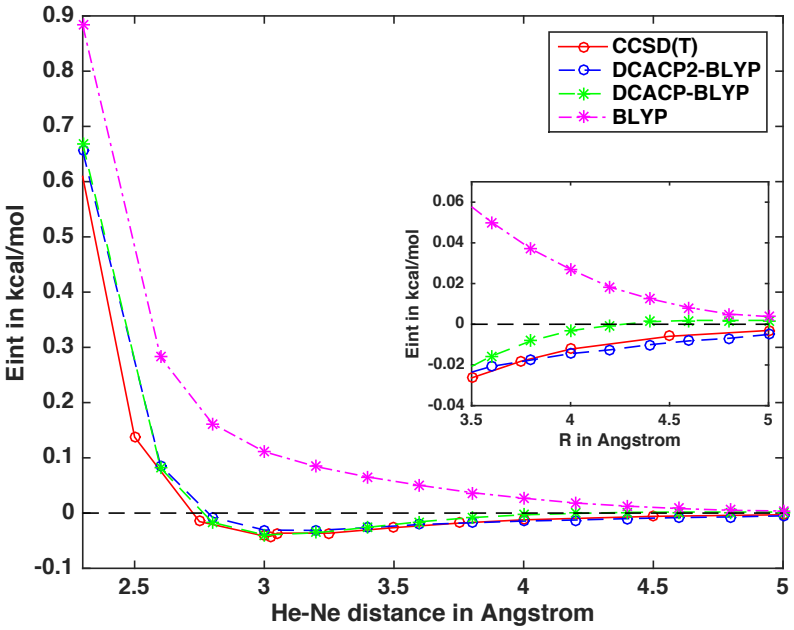

Figure 5.7 Interaction energy of the helium-argon dimer as function of the interatomic distance.

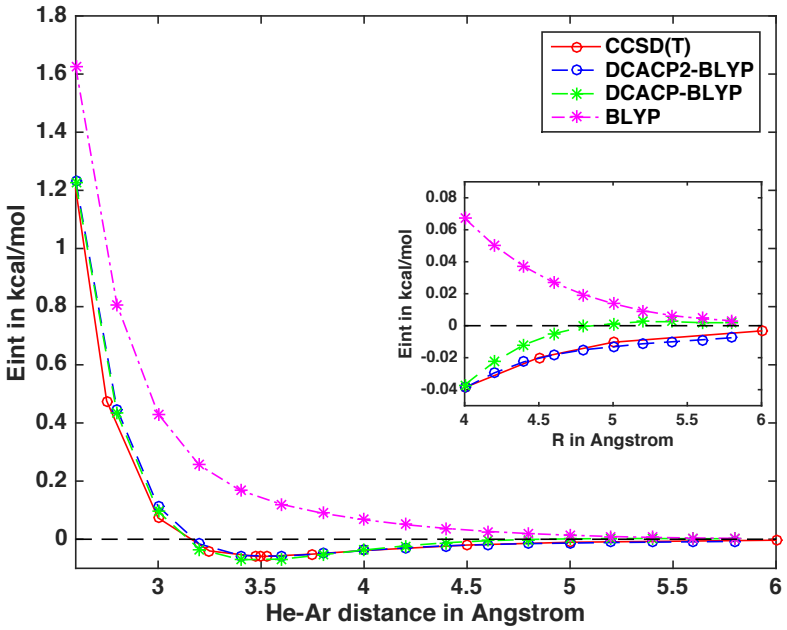

Figure 5.8 Interaction energy of the neon-argon dimer as function of the interatomic distance.

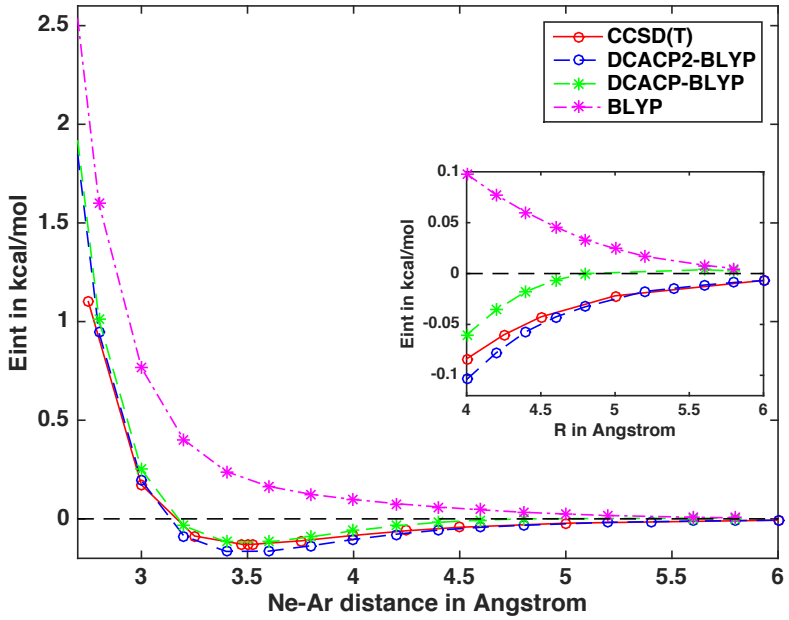

5.3.3 Reproducing the long range R^{-2n} behavior

Because the dispersion force is relatively weak, we can describe it using perturbation theory. The long-range dispersion energy $E_{disp}(R)$ between two neutral atoms or molecules A and B in their ground states can be expressed as the function of their inter-atomic distance *R*:

$$E_{disp}(R) = -\frac{C_6}{R^6} - \frac{C_8}{R^8} - \frac{C_{10}}{R^{10}} - \cdots \qquad \text{Equation 5.9}$$

where C_6, C_8 and C_{10} are the leading-order molecular dispersion coefficients, describing dipole-dipole interactions, dipole-quadrupole interactions, dipole-octupole and quadrupole-quadrupole interactions, respectively. The $\frac{C_6}{R^6}$ term dominates for sufficiently large *R*. The C_n coefficients for helium, neon and argon, taken from the literature[106], are tabulated in **Table 5.4**.

Table 5.4 The experimentally determined C_6, C_8 and C_{10} coefficients for helium, neon and argon (in atomic units units)[106].

Element	C_6	C_8	C_{10}
He	1.4610	14.118	183.69
Ne	6.4470	96.500	1520.0
Ar	63.500	1510.0	48,000

To further examine if the behavior of DCACP2-BLYP accurately reproduces the correct $\frac{C_6}{R^6}$ behavior at distances longer than R_{eq}, the interaction energies are compared with the experimentally determined dispersion contribution from the C_6, C_8 and C_{10} terms, as displayed in **Figures 5.9, 5.10** and **5.11**.

Figure 5.9 Correction to BLYP interaction energy by the DCACP methods compared to experimental C_6R^{-6}, $C_6R^{-6}+C_8R^{-8}$, $C_6R^{-6}+C_8R^{-8}+C_{10}R^{-10}$ terms, as well as dispersion energy from DFT-SAPT calculations for argon dimer.

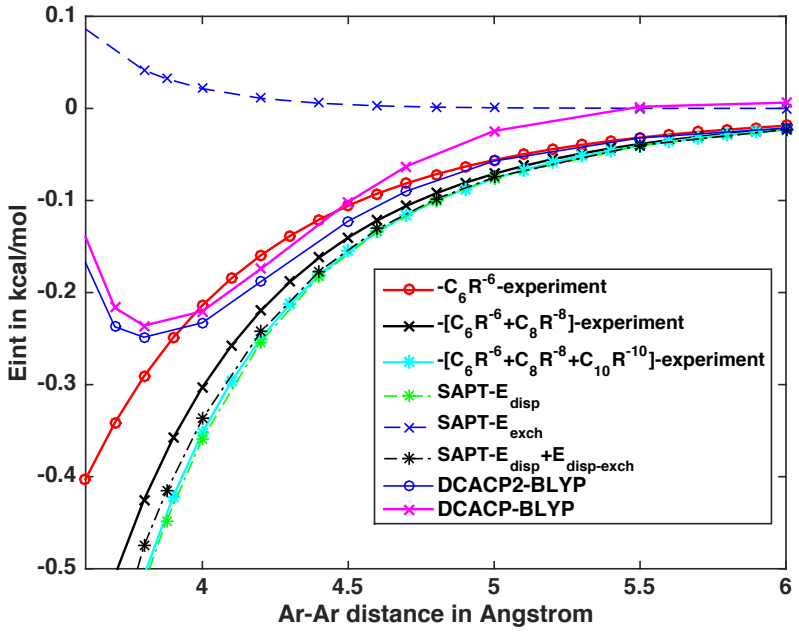

Figure 5.10 Correction to BLYP interaction energy by the DCACP methods compared to experimental C_6R^{-6}, $C_6R^{-6}+C_8R^{-8}$, $C_6R^{-6}+C_8R^{-8}+C_{10}R^{-10}$terms, as well as dispersion energy from DFT-SAPT calculations for neon dimer.

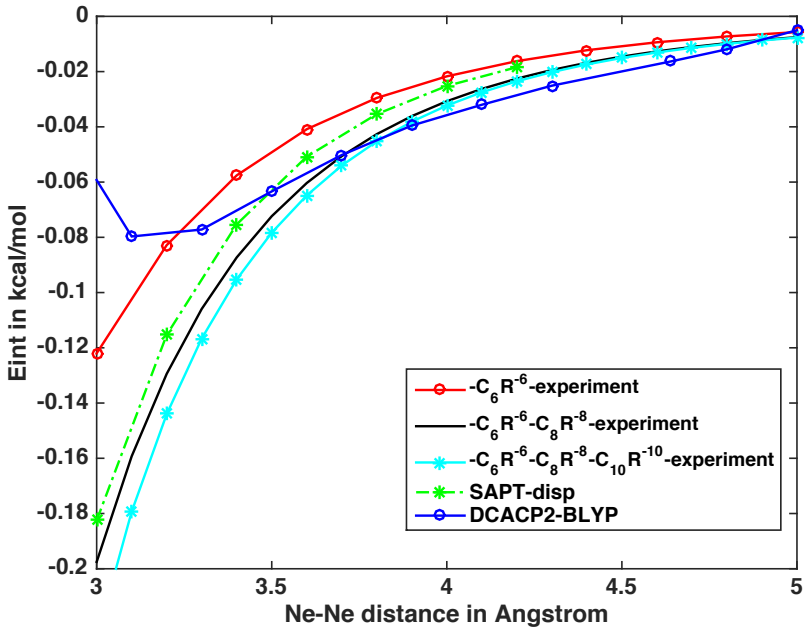

Figure 5.11 Correction to BLYP interaction energy by the DCACP methods compared to experimental C_6R^{-6}, $C_6R^{-6}+C_8R^{-8}$, $C_6R^{-6}+C_8R^{-8}+C_{10}R^{-10}$ terms for helium dimer.

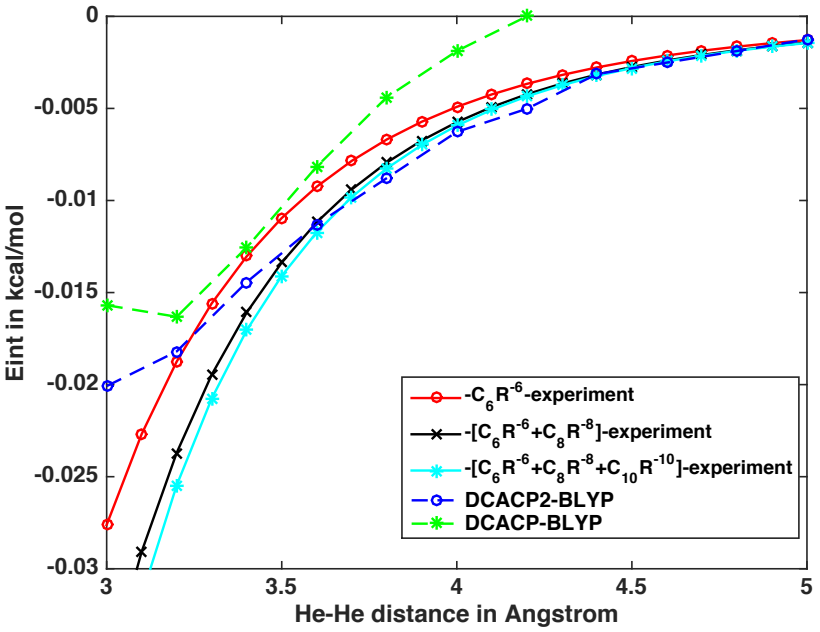

Take argon as an example, as shown in **Figure 5.9**, the interaction energy contribution of argon dimer is shown for both the DCACP and DCACP2-corrected BLYP functional, as well as the $\frac{C_6}{R^6}$ and plus the higher-order terms calculated using the experimentally determined C_n (n=6, 8, 10) coefficients in **Table 5.4** and the dispersion energies obtained from the DF-DFT-SAPT

calculations. It is observed that for distances of the two atoms less than equilibrium distance at 3.8 Å, the DCACP and DCACP2 methods yield similar interaction energy contributions, while starting from about 4.0 Å, the interaction energy curves of the two methods start to differ. In the case of DCACP, an exponential decrease of the argon-argon interaction energy is observed, while the DCACP2 interaction energy curve decays approximately as $\frac{1}{R^6}$ for distances between 4.0 and 6.0 Å, and reproduces the dispersion energy contribution from the DF-DFT-SAPT energies. Then I checked the binding energy curve of DCACP2-BLYP at distances greater than 6.0 Å for argon dimer, and compared it with the $\frac{C_6}{R^6}$ curve.

As shown in the magnified plot in **Figure 5.12**, the binding energy curve of DCACP2-BLYP potential in the range of 6.0-10.0 Å falls more rapidly than $\frac{C_6}{R^6}$. Therefore, the DCACP2-BLYP potential for argon can only accurately reproduce the $\frac{C_6}{R^6}$ dispersion energy for interatomic separation up to 6.0 Å, and falls off more rapidly at longer distances.

Figure 5.12 Binding energy curve of DCACP2-correced BLYP potential for argon dimer, its exponential fitted curve as well as the $\frac{C_6}{R^6}$ curve as a function of the interatomic distance R in the region of 6.0-10.0 Å.

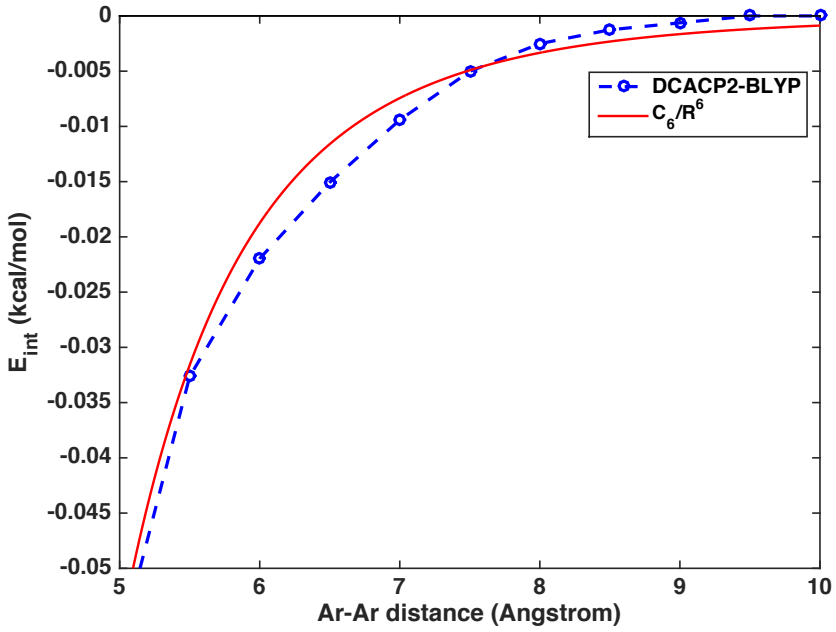

5.3.4 Electron density distortions

To evaluate the electron density distortion due to the inclusion of the DCACP2 terms, we considered electron density differences for a dimer separated along the z-axis as a function of the interatomic distance z by integrating over the corresponding orthogonal x-y planes, i.e.:

$$\Delta n_{DCACP2-BLYP}(z) = \iint dxdy[n_{DCACP2}(\boldsymbol{r})\text{-}n_{BLYP}(\boldsymbol{r})] \qquad \text{Equation 5.10}$$

In **Figure 6.11**, we computed this integrated electron density difference of argon dimer with the atoms separated by 17.0 Bohr, a distance long enough that the dispersion energy dominates the interaction energy. The locations of the two argon atoms are represented by the blue vertical lines. When the DCACP2-BLYP potential to atom A only (located at z = 15.0 Bohr) as shown in **Figure 5.13 (a)**, the electron density on atom B with uncorrected BLYP potential (located at z = 32.0 Bohr) is distorted compared with that of the original dimer without the DCACP2 correction, with the accumulation of charge pointing toward atom A. In **Figure 5.13 (b),** both of the argon atoms have the DCACP2 terms, and this gives rise to the redistribution of $n(\boldsymbol{r})$ on each atom caused by the DCACP2 potential centered the other one. Two accumulative peaks are developed in the region between the two atoms due to the inclusion of DCACP2 potential. This accumulation of charges(δ-) reflects a dipole moment on each atom is formed, with the negative end pointing toward the other atom. Therefore, there is an attraction between each displaced nuclei ($\delta+$) and its own distorted density(δ-), as depicted in Figure 5.14.

Figure 5.13 Integrated electron density differences $\Delta\rho(\boldsymbol{r}) = \int dxdy[n^{DCACP2_{BLYP}}(\boldsymbol{r})\text{-}\, n^{BLYP}(\boldsymbol{r})]$ in atomic units (a.u.) along the *z*-axis for the argon dimer with the atoms separated by 17.0 Bohr. The vertical blue lines show the positions of the argon atoms, locating at $z = 15.0$ bohr and $z = 32.0$ bohr, respectively. a) the DCACP2-BLYP potential only exerts on argon atom A. b) both argon atoms have been added the DCACP2-BLYP potential.

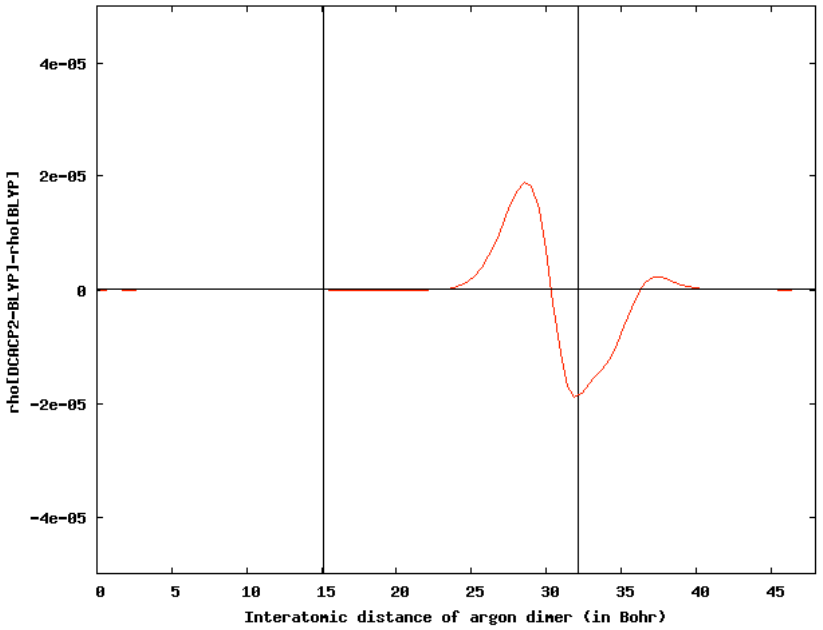

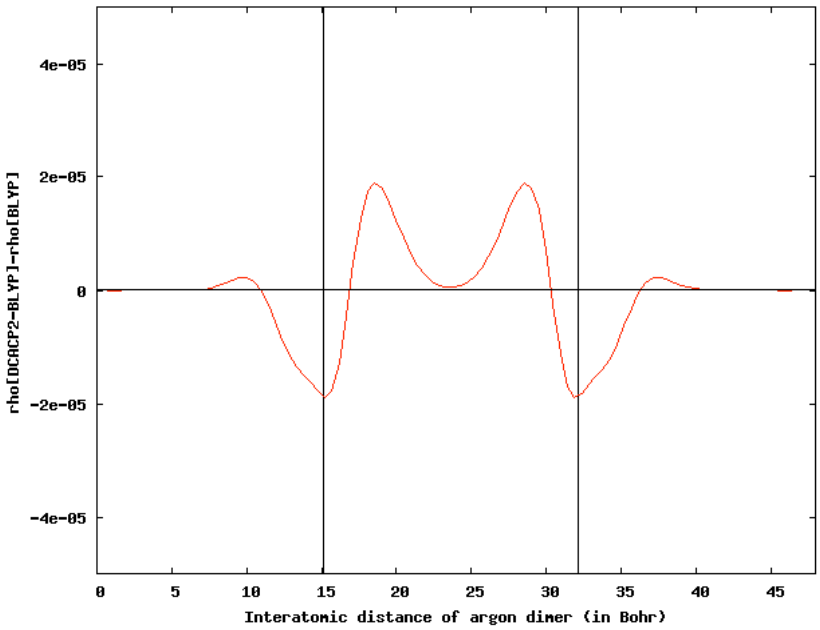

In Feynman's famous 1939 paper[107], he predicted that the long-range dispersion interaction between two atoms leads to a permanent dipole moment on each atom, with the negative end of the dipole pointing toward each other; and that it is the attraction between the displaced nuclei with its own distorted electron density that give rise to net attraction of dispersion. This Feynman picture is depicted in **Figure 5.14**.

Figure 5.14 Depiction of Feynman's observation for the attraction between the nuclei and its own distorted electron density that give rise to the dispersion between two atoms at long separation R.

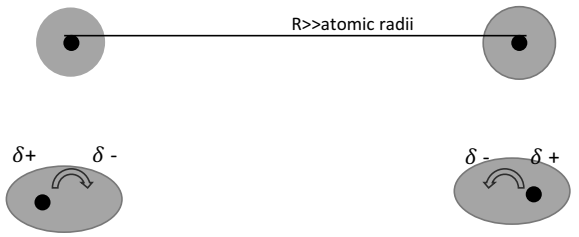

Feynman also observed that the permanent dipole acquired by each atom due to dispersion display an R^{-7} dependence on the internuclear distance R. Therefore, we calculated the dispersion-induced dipole from DCACP2 for argon, and compared it with the expression of the dispersion dipole for coupled Drude oscillators from a recent study of our group[92]. The expression of dispersion-induced dipole moment of atom B induced by atom A is calculated to be (retaining terms through R^{-7}):

$$\mu^B = -\frac{\alpha^A B^B_{zzzz} \omega_0}{R^7} \qquad \text{Equation 5.11}$$

where α^A is the static dipole polarizability of atom A, and B^B_{zzzz} is the *zzzz* component of the static dipole-dipole-quadrupole hyperpolarizability of B, and the value of ω_0 is calculated to be *1.036 a.u.* as from α and the dispersion coefficients C_6 with the equation $C_6 = \frac{1}{2}\alpha^2\omega_0$. Plugging the value $\alpha = 11.07\ a.u.$ and $B_{zzzz} = -167.5\ a.u.$ for argon[108], an R^{-7} curve of the dipole

beyond the overlap region of argon dimer can be obtained, and it matches quite well with the dispersion-induced dipole on atom *B* calculated from DCACP2, depicted in **Figure 6.13**. The induced dipole d_{ind} on atom B results from the DCACP2 potential on atom A.

Figure 5.15 Dispersion-induced permanent atomic dipole moment on a single argon atom of argon dimer by the inclusion of the DCACP2-BLYP potential, as function of atomic separation.

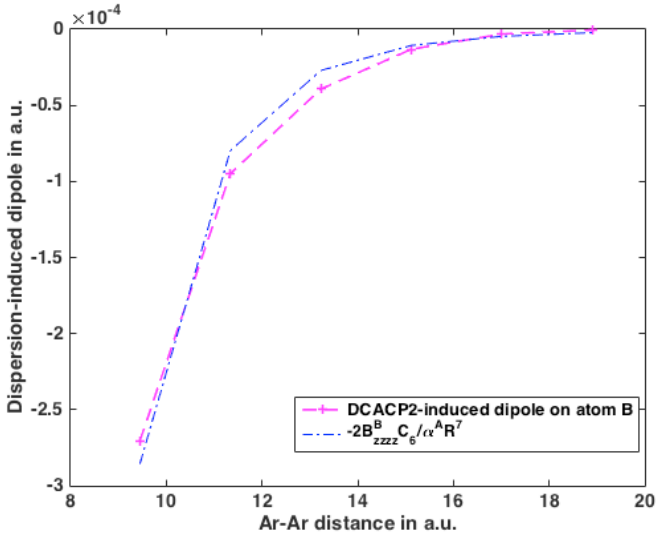

5.3.5 Analysis of argon dimer interactions

Given the change in the charge distribution, one can calculate the dispersion energy by use of the electrostatic Hellmann-Feynman theorem[107]. However, DFT calculations do not involve this step, leading one to ask why the electron density distortion induced by the atom-centered empirical potential gives an energy correction that closely mimics the dispersion energy. We explored two possibilities:1) That this gives a change in the atom-atom interactions that goes approximately as $1/R^6$; 2) That it is the result of the lowering of the energy of one atom due to the additional long-range attraction from the other atom. Our calculations show that the electrostatic interactions resulting from the coupling of the atomic multipoles is orders of magnitudes smaller than the

energy changes due to dispersion correction, and we only display the multipoles in **Table 5.5** and **Table 5.6**. Therefore, we have ruled out the first possibility and we are now going to test the second possibility that the extra binding afforded by DCACP2 comes mainly from the fact that the terms in the DCACPs exert an attractive potential on remote atoms.

Table 5.5 The permanent distributed multipole moments (in atomic units) for argon dimer at different separations, from GDMA2 program using MP2 densities calculated with Gaussian09 program.

R (Å)	*q*	Q_{10}	Q_{20}
5.0	0.0E-05	-0.03517	-0.33084
6.0	0.0E-05	-0.01802	-0.20343
7.0	0.0E-05	-0.00929	-0.12266
8.0	1.0E-05	-0.00491	-0.07436
9.0	1.0E-05	-0.00269	-0.04588
10.0	0.0E-05	-0.00154	-0.02906

Note: The spherical tensor representation of the quadrupole is employed. For conversion into Cartesian representation: $Q_{10} = \mu_Z$, $Q_{20} = \Theta_{zz}$.

Table 5.6 The induced atomic dipole (d_{ind}), induced quadrupole moment from induced dipoles ($Q_{d\text{-}d}$), and the net induced quadrupoles (Q_{ind}) of dimers with and without DCACP2-corrected BLYP functionals in atomic units.

R(Å)	d_{ind}	$Q_{d\text{-}d}$	Q_{ind}
5	2.7045E-04	0.01022	-0.003237
6	9.4898E-05	0.0043	-0.001357
7	3.9349E-05	0.0021	-6.4349E-04
8	1.3173E-05	0.0008	-2.4741E-04
9	3.1280E-06	2.1280E-04	-6.7028E-05
10	5.1543E-07	3.8961E-05	-1.2027E-05

To check this, we calculated the interaction energies of the BLYP and DCACP2-BLYP argon dimers separated at long ranges *5.0*, *6.0*, *7.0*, *8.0*, *9.0* and *10.0* Å, region where electron overlap between the two argon atoms is negligible. As tabulated in **Table 5.7**, DCACP2-BLYP value of the binding energy of Ar2 decay slower at these distances, compared with the single-channel DCACP-corrected binding energies. Both the original BLYP functional and single-channel BLYP-DCACP method give repulsive values in this region, and our two-channel DCACP2 method corrects the binding energies much better in this region. This leads to a lowering of the binding energy of argon dimer due to the additional long-range attraction from the DCACP2-BLYP method.

Table 5.7 The binding energy of argon dimer with and without DCACP2 correction, in kcal/mol.

R(Å)	E_{BLYP}	$E_{DCACP2\text{-}BLYP}$	$E_{DCACP\text{-}BLYP}$
5	0.06463	-0.05710	-0.02447
6	0.01443	-0.02196	0.00565
7	0.00188	-0.00941	0.00188
8	0.00000	-0.00251	0.00000
9	0.00000	-0.00063	0.00000
10	0.00000	0.00000	0.00000

5.4 CONCLUSIONS

We have parametrized two-channel dispersion-corrected atom-centered potentials for He, Ne and Ar, expanding the DCACP2 library from our previous work. The implementation has been made for the BLYP density functional through the addition of terms to the Goedecker-Teter-Hutter type pseudopotentials. The DCACP2 approach performs much better than does the single-

channel DCACP method for describing the interaction energies of the inert gas dimers, at distances appreciably greater than R_{eq}. We also examined the atomic density distortion caused by the DCACP2-BLYP potential, and charge accumulation in the region between the two atoms is observed. Work is in progress to i) test the DCACP2 in combination with exchange correlation functionals other than BLYP, ii) to explicitly include in the Hamiltonian three-body interaction energies in the penalty functional, and iii) to establish a comprehensive library of DCACP2 potentials for wider range of elements.

6.0 CONCLUSIONS AND FUTURE WORK

6.1 MAIN CONCLUSIONS OF THIS WORK

In this thesis, to better understand the structural, energetic, and dynamics properties of condensed phases of water including the proton-disordered ice phase ice Ih and liquid water, I have employed classical molecular dynamics as well as periodic DFT calculations in the calculations of several key properties of ice Ih and liquid water.

The main conclusions of this work are:

1) The role of polarizability is important for determining of dielectric constant of ice Ih. In addition, polarizable water force fields that employs three polarizable sites per molecule perform better than those with a single polarizable site; An initial PIMD simulation showed that nuclear quantum effects at T = 100 K cause an average elongation of the O-H bond length in ice Ih by 29 %, and thus should not be neglected.
2) I found that several dispersion-corrected BLYP functionals give better descriptions than the original BLYP functional of monomer geometry, lattice dimensions, cohesive energies, equilibrium volumes as well as of the bulk modulus of the ice Ih unit cell.
3) I found that AIMD simulations using several dispersion-corrected BLYP functionals give structural properties and rotational dynamics of liquid water in better agreement with experiment than do simulation with the BLYP functional.

4) By parametrizing against high-level CCSD(T) calculations, two-channel dispersion-corrected atom-centered potentials for correcting long-range dispersion corrections for three rare gas dimers: He_2, Ne_2 and Ar_2 are optimized. The DCACP2 approach significantly improves of long-range binding energy of these dimers compared to the results obtained with one-channel potentials. I also analyzed the success of DCACP2.

6.2 POSSIBLE FUTURE DIRECTIONS

As reviewed in section 2.1.3, simulation of ice Ih using DFT methods greatly overestimate the value of the dielectric constant. Because the graph invariant enumeration technique[14] gives a complete set of ice Ih configurations, obtaining *ab initio* energies and dipole moments of symmetry distinct ice Ih configurations would probably give rise to better prediction of the ε_s of ice Ih. Also, it would enable the extrapolation of results to larger cells. Based on our knowledge, no prior work of predicting ε_s of ice Ih using this approach has been carried out before.

To describe the binding energy of systems where many-body interactions are important, developing a new version of the DCACP2 method based on fitting three-body energies would help more correctly describe the binding energies of such chemical systems.

Also, considering the contributions of the zero-point energy (ZPE) to both the cohesive energy of ice and the rotational dynamics of liquid water are non-negligible, future work taking the ZPE into account in the calculation of condensed phases of water would possibly get more accurate predictions of their energetics and dynamics, especially under low temperatures.

BIBLIOGRAPHY

1. Laury, M. L.; Wang, L. P.; Pande, V. S.; Head-Gordon, T.; Ponder, J. W., Revised Parameters for the AMOEBA Polarizable Atomic Multipole Water Model. *J Phys Chem B* **2015,** *119* (29), 9423-37.
2. Dang, L. X.; Chang, T.-M., Molecular dynamics study of water clusters, liquid, and liquid–vapor interface of water with many-body potentials. *The Journal of Chemical Physics* **1997,** *106* (19), 8149-8159.
3. (a) Salzmann, C. G.; Radaelli, P. G.; Slater, B.; Finney, J. L., The polymorphism of ice: five unresolved questions. *Physical Chemistry Chemical Physics* **2011,** *13* (41), 18468-18480; (b) Petrenko, V. F.; Whitworth, R. W., *Physics of Ice*. Oxford University Press: Oxford, 2002; p 392.
4. Bernal, J. D.; Fowler, R. H., A Theory of Water and Ionic Solution, with Particular Reference to Hydrogen and Hydroxyl Ions. *The Journal of Chemical Physics* **1933,** *1* (8), 515-548.
5. Pauling, L., The Structure and Entropy of Ice and of Other Crystals with Some Randomness of Atomic Arrangement. *Journal of the American Chemical Society* **1935,** *57* (12), 2680-2684.
6. http://www1.lsbu.ac.uk/water/water_anomalies.html.
7. Bjerrum, N., Structure and Properties of Ice. *Science* **1952,** *115* (2989), 385-390.
8. Lindberg, G. E.; Wang, F., Efficient Sampling of Ice Structures by Electrostatic Switching. *The Journal of Physical Chemistry B* **2008,** *112* (20), 6436-6441.
9. Jorgensen, W. L., Revised TIPS for simulations of liquid water and aqueous solutions. *The Journal of Chemical Physics* **1982,** *77* (8), 4156-4163.
10. Berendsen, H. J. C.; Grigera, J. R.; Straatsma, T. P., The missing term in effective pair potentials. *The Journal of Physical Chemistry* **1987,** *91* (24), 6269-6271.
11. Johari, G. P.; Whalley, E., The dielectric properties of ice Ih in the range 272–133 K. *The Journal of Chemical Physics* **1981,** *75* (3), 1333-1340.
12. Debye, P., *Polare Molekeln*. Leipzig: S. Hirzel: 1929.
13. Tyagi, M.; Murthy, S. S. N., Dielectric Relaxation in Ice and Ice Clathrates and Its Connection to the Low-Temperature Phase Transition Induced by Alkali Hydroxides as Dopants. *The Journal of Physical Chemistry A* **2002,** *106* (20), 5072-5080.
14. Kuo, J.-L.; Coe, J. V.; Singer, S. J.; Band, Y. B.; Ojamäe, L., On the use of graph invariants for efficiently generating hydrogen bond topologies and predicting physical properties of water clusters and ice. *The Journal of Chemical Physics* **2001,** *114* (6), 2527-2540.
15. (a) Rick, S. W.; Haymet, A. D. J., Dielectric constant and proton order and disorder in ice Ih: Monte Carlo computer simulations. *The Journal of Chemical Physics* **2003,** *118* (20), 9291-

9296; (b) Rahman, A.; Stillinger, F. H., Proton Distribution in Ice and the Kirkwood Correlation Factor. *The Journal of Chemical Physics* **1972,** *57* (9), 4009-4017.
16. MacDowell, L. G.; Vega, C., Dielectric Constant of Ice Ih and Ice V: A Computer Simulation Study. *The Journal of Physical Chemistry B* **2010,** *114* (18), 6089-6098.
17. Aragones, J. L.; MacDowell, L. G.; Vega, C., Dielectric Constant of Ices and Water: A Lesson about Water Interactions. *The Journal of Physical Chemistry A* **2011,** *115* (23), 5745-5758.
18. Rick, S. W., Simulations of proton order and disorder in ice Ih. *The Journal of Chemical Physics* **2005,** *122* (9), 094504.
19. Shi, L.; Ni, Y.; Drews, S. E. P.; Skinner, J. L., Dielectric constant and low-frequency infrared spectra for liquid water and ice Ih within the E3B model. *The Journal of Chemical Physics* **2014,** *141* (8), 084508.
20. Liu, H.; Wang, Y.; Bowman, J. M., Transferable ab Initio Dipole Moment for Water: Three Applications to Bulk Water. *The Journal of Physical Chemistry B* **2016,** *120* (8), 1735-1742.
21. Rusnak, A. J.; Pinnick, E. R.; Calderon, C. E.; Wang, F., Static dielectric constants and molecular dipole distributions of liquid water and ice-Ih investigated by the PAW-PBE exchange-correlation functional. *The Journal of Chemical Physics* **2012,** *137* (3), 034510.
22. Batista, E. R.; Xantheas, S. S.; Jónsson, H., Molecular multipole moments of water molecules in ice Ih. *The Journal of Chemical Physics* **1998,** *109* (11), 4546-4551.
23. Schönherr, M.; Slater, B.; Hutter, J.; VandeVondele, J., Dielectric Properties of Water Ice, the Ice Ih/XI Phase Transition, and an Assessment of Density Functional Theory. *The Journal of Physical Chemistry B* **2014,** *118* (2), 590-596.
24. Moreira, P. A. F. P.; de Koning, M., Nuclear quantum fluctuations in ice Ih. *Physical Chemistry Chemical Physics* **2015,** *17* (38), 24716-24721.
25. Car, R.; Parrinello, M., Unified Approach for Molecular Dynamics and Density-Functional Theory. *Physical Review Letters* **1985,** *55* (22), 2471-2474.
26. Ren, P.; Ponder, J. W., Polarizable Atomic Multipole Water Model for Molecular Mechanics Simulation. *The Journal of Physical Chemistry B* **2003,** *107* (24), 5933-5947.
27. Wang, L.-P.; Head-Gordon, T.; Ponder, J. W.; Ren, P.; Chodera, J. D.; Eastman, P. K.; Martinez, T. J.; Pande, V. S., Systematic Improvement of a Classical Molecular Model of Water. *The Journal of Physical Chemistry B* **2013,** *117* (34), 9956-9972.
28. Abascal, J. L. F.; Sanz, E.; García Fernández, R.; Vega, C., A potential model for the study of ices and amorphous water: TIP4P/Ice. *The Journal of Chemical Physics* **2005,** *122* (23), 234511.
29. Horn, H. W.; Swope, W. C.; Pitera, J. W.; Madura, J. D.; Dick, T. J.; Hura, G. L.; Head-Gordon, T., Development of an improved four-site water model for biomolecular simulations: TIP4P-Ew. *The Journal of Chemical Physics* **2004,** *120* (20), 9665-9678.
30. Cisneros, G. A., Application of Gaussian Electrostatic Model (GEM) Distributed Multipoles in the AMOEBA Force Field. *Journal of Chemical Theory and Computation* **2012,** *8* (12), 5072-5080.
31. *DL_POLY*, 2006.
32. Allen, M. P.; Tildesley, D. J., *Computer simulation of liquids*. Clarendon Press: 1989; p 385.
33. Ponder, J. W. *TINKER – Software Tools for Molecular Design*, 7.1.2; 2015.
34. Case, D. A.; Darden, T. A.; Cheatham, T. E.; Simmerling, C. L.; Wang, J.; Duke, R. E.; Luo, R.; Walker, R. C.; Zhang, W.; Merz, K. M.; Roberts, B.; Hayik, S.; Roitberg, A.; Seabra, G.; Swails, J.; Goetz, A. W.; Kolossváry, I.; Wong, K. F.; Paesani, F.; Vanicek, J.; Wolf, R. M.; Liu, J.; Wu, X.; Brozell,

S. R.; Steinbrecher, T.; Gohlke, H.; Cai, Q.; Ye, X.; Wang, J.; Hsieh, M. J.; Cui, G.; Roe, D. R.; Mathews, D. H.; Seetin, M. G.; Salomon-Ferrer, R.; Sagui, C.; Babin, V.; Luchko, T.; Gusarov, S.; Kovalenko, A.; Kollman, P. A., AMBER 12. University of California, San Francisco: 2012.
35. Paesani, F.; Zhang, W.; Case, D. A.; Cheatham, T. E.; Voth, G. A., An accurate and simple quantum model for liquid water. *The Journal of Chemical Physics* **2006,** *125* (18), 184507.
36. Halgren, T. A.; Damm, W., Polarizable force fields. *Current Opinion in Structural Biology* **2001,** *11* (2), 236-242.
37. Van Belle, D.; Froeyen, M.; Lippens, G.; Wodak, S. J., Molecular dynamics simulation of polarizable water by an extended Lagrangian method. *Molecular Physics* **1992,** *77* (2), 239-255.
38. Gillan, M. J.; Alfe, D.; Michaelides, A., Perspective: How good is DFT for water? *J Chem Phys* **2016,** *144* (13), 130901.
39. Fanourgakis, G. S.; Xantheas, S. S., Development of transferable interaction potentials for water. V. Extension of the flexible, polarizable, Thole-type model potential (TTM3-F, v. 3.0) to describe the vibrational spectra of water clusters and liquid water. *The Journal of Chemical Physics* **2008,** *128* (7), 074506.
40. Clough, S. A.; Beers, Y.; Klein, G. P.; Rothman, L. S., Dipole moment of water from Stark measurements of H2O, HDO, and D2O. *The Journal of Chemical Physics* **1973,** *59* (5), 2254-2259.
41. Barkema, G. T.; Boer, J. d., Properties of a statistical model of ice at low temperatures. *The Journal of Chemical Physics* **1993,** *99* (3), 2059-2067.
42. Ceriotti, M.; Fang, W.; Kusalik, P. G.; McKenzie, R. H.; Michaelides, A.; Morales, M. A.; Markland, T. E., Nuclear Quantum Effects in Water and Aqueous Systems: Experiment, Theory, and Current Challenges. *Chemical Reviews* **2016,** *116* (13), 7529-7550.
43. Kuo, J.-L.; Singer, S. J., Graph invariants for periodic systems: Towards predicting physical properties from the hydrogen bond topology of ice. *Physical Review E* **2003,** *67* (1), 016114.
44. Wong, P. T. T.; Whalley, E., Raman spectrum of ice VIII. *The Journal of Chemical Physics* **1976,** *64* (6), 2359-2366.
45. Buch, V.; Sandler, P.; Sadlej, J., Simulations of H2O Solid, Liquid, and Clusters, with an Emphasis on Ferroelectric Ordering Transition in Hexagonal Ice. *The Journal of Physical Chemistry B* **1998,** *102* (44), 8641-8653.
46. Nada, H.; van der Eerden, J. P. J. M., An intermolecular potential model for the simulation of ice and water near the melting point: A six-site model of H2O. *The Journal of Chemical Physics* **2003,** *118* (16), 7401-7413.
47. (a) Santra, B.; Klimeš, J.; Tkatchenko, A.; Alfè, D.; Slater, B.; Michaelides, A.; Car, R.; Scheffler, M., On the accuracy of van der Waals inclusive density-functional theory exchange-correlation functionals for ice at ambient and high pressures. *The Journal of Chemical Physics* **2013,** *139* (15), 154702; (b) Shirkov, L.; Makarewicz, J., Does DFT-SAPT method provide spectroscopic accuracy? *J Chem Phys* **2015,** *142* (6), 064102.
48. Pamuk, B.; Allen, P. B.; Fernández-Serra, M. V., Electronic and nuclear quantum effects on the ice XI/ice Ih phase transition. *Physical Review B* **2015,** *92* (13).
49. Murray, É. D.; Galli, G., Dispersion Interactions and Vibrational Effects in Ice as a Function of Pressure: A First Principles Study. *Physical Review Letters* **2012,** *108* (10), 105502.
50. Karalti, O.; Su, X.; Al-Saidi, W. A.; Jordan, K. D., Correcting density functionals for dispersion interactions using pseudopotentials. *Chemical Physics Letters* **2014,** *591*, 133-136.
51. Hamann, D. R., ${\mathrm{H}}_{2}$O hydrogen bonding in density-functional theory.

Physical Review B **1997,** *55* (16), R10157-R10160.
52. Kuhs, W. F.; Finney, J. L.; Vettier, C.; Bliss, D. V., Structure and hydrogen ordering in ices VI, VII, and VIII by neutron powder diffraction. *The Journal of Chemical Physics* **1984,** *81* (8), 3612-3623.
53. Hutter, J.; Iannuzzi, M.; Schiffmann, F.; VandeVondele, J., cp2k:atomistic simulations of condensed matter systems. *Wiley Interdisciplinary Reviews: Computational Molecular Science* **2014,** *4* (1), 15-25.
54. (a) Becke, A. D., Density-functional exchange-energy approximation with correct asymptotic behavior. *Physical Review A* **1988,** *38* (6), 3098-3100; (b) Lee, C.; Yang, W.; Parr, R. G., Development of the Colle-Salvetti correlation-energy formula into a functional of the electron density. *Physical Review B* **1988,** *37* (2), 785-789.
55. Grimme, S.; Antony, J.; Ehrlich, S.; Krieg, H., A consistent and accurate ab initio parametrization of density functional dispersion correction (DFT-D) for the 94 elements H-Pu. *The Journal of Chemical Physics* **2010,** *132* (15), 154104.
56. Lin, I. C.; Coutinho-Neto, M. D.; Felsenheimer, C.; von Lilienfeld, O. A.; Tavernelli, I.; Rothlisberger, U., Library of dispersion-corrected atom-centered potentials for generalized gradient approximation functionals: Elements H, C, N, O, He, Ne, Ar, and Kr. *Physical Review B* **2007,** *75* (20).
57. VandeVondele, J.; Hutter, J., Gaussian basis sets for accurate calculations on molecular systems in gas and condensed phases. *The Journal of Chemical Physics* **2007,** *127* (11), 114105.
58. Goedecker, S. a. T., M and Hutter, J, Separable dual-space Gaussian pseudopotentials. *Physical Review B* **1996,** *54* (3), 54.
59. Dove, M., *Introduction to Lattice Dynamics*. Cambridge University Press: 1993.
60. Whalley, E., Energies of the phases of ice at zero temperature and pressure. *The Journal of Chemical Physics* **1984,** *81* (9), 4087-4092.
61. Herrero, C. P.; Ramirez, R., Isotope effects in ice Ih: a path-integral simulation. *J Chem Phys* **2011,** *134* (9), 094510.
62. (a) Barnett, R. N.; Landman, U.; Nitzan, A.; Rajagopal, G., Born‐Oppenheimer dynamics using density‐functional theory: Equilibrium and fragmentation of small sodium clusters. *The Journal of Chemical Physics* **1991,** *94* (1), 608-616; (b) Wentzcovitch, R. M.; Martins, J., First principles molecular dynamics of Li: Test of a new algorithm. *Solid State Communications* **1991,** *78* (9), 831-834.
63. English, N., Structural Properties of Liquid Water and Ice Ih from Ab-Initio Molecular Dynamics with a Non-Local Correlation Functional. *Energies* **2015,** *8* (9), 9383.
64. Todorova, T.; Seitsonen, A. P.; Hutter, J.; Kuo, I. F. W.; Mundy, C. J., Molecular Dynamics Simulation of Liquid Water: Hybrid Density Functionals. *The Journal of Physical Chemistry B* **2006,** *110* (8), 3685-3691.
65. Lin, I. C.; Seitsonen, A. P.; Tavernelli, I.; Rothlisberger, U., Structure and Dynamics of Liquid Water from ab Initio Molecular Dynamics—Comparison of BLYP, PBE, and revPBE Density Functionals with and without van der Waals Corrections. *Journal of Chemical Theory and Computation* **2012,** *8* (10), 3902-3910.
66. VandeVondele, J.; Krack, M.; Mohamed, F.; Parrinello, M.; Chassaing, T.; Hutter, J., Quickstep: Fast and accurate density functional calculations using a mixed Gaussian and plane waves approach. *Computer Physics Communications* **2005,** *167* (2), 103-128.

67. VandeVondele, J.; Mohamed, F.; Krack, M.; Hutter, J.; Sprik, M.; Parrinello, M., The influence of temperature and density functional models in ab initio molecular dynamics simulation of liquid water. *The Journal of Chemical Physics* **2005,** *122* (1), 014515.
68. Martínez, L.; Andrade, R.; Birgin, E. G.; Martínez, J. M., PACKMOL: A package for building initial configurations for molecular dynamics simulations. *Journal of Computational Chemistry* **2009,** *30* (13), 2157-2164.
69. Head-Gordon, T.; Hura, G., Water Structure from Scattering Experiments and Simulation. *Chemical Reviews* **2002,** *102* (8), 2651-2670.
70. (a) Ceriotti, M.; Bussi, G.; Parrinello, M., Langevin Equation with Colored Noise for Constant-Temperature Molecular Dynamics Simulations. *Physical Review Letters* **2009,** *102* (2), 020601; (b) Ceriotti, M.; Bussi, G.; Parrinello, M., Nuclear Quantum Effects in Solids Using a Colored-Noise Thermostat. *Physical Review Letters* **2009,** *103* (3), 030603.
71. Yeh, Y.-l.; Mou, C.-Y., Orientational Relaxation Dynamics of Liquid Water Studied by Molecular Dynamics Simulation. *The Journal of Physical Chemistry B* **1999,** *103* (18), 3699-3705.
72. Marzari, N.; Vanderbilt, D., Maximally localized generalized Wannier functions for composite energy bands. *Physical Review B* **1997,** *56* (20), 12847-12865.
73. Brehm, M.; Kirchner, B., TRAVIS - A Free Analyzer and Visualizer for Monte Carlo and Molecular Dynamics Trajectories. *Journal of Chemical Information and Modeling* **2011,** *51* (8), 2007-2023.
74. Soper, A. K., The radial distribution functions of water and ice from 220 to 673 K and at pressures up to 400 MPa. *Chemical Physics* **2000,** *258* (2–3), 121-137.
75. Skinner, L. B.; Huang, C.; Schlesinger, D.; Pettersson, L. G. M.; Nilsson, A.; Benmore, C. J., Benchmark oxygen-oxygen pair-distribution function of ambient water from x-ray diffraction measurements with a wide Q-range. *The Journal of Chemical Physics* **2013,** *138* (7), 074506.
76. Strässle, T.; Saitta, A. M.; Godec, Y. L.; Hamel, G.; Klotz, S.; Loveday, J. S.; Nelmes, R. J., Structure of Dense Liquid Water by Neutron Scattering to 6.5 GPa and 670 K. *Physical Review Letters* **2006,** *96* (6), 067801.
77. Mills, R., Self-diffusion in normal and heavy water in the range 1-45.deg. *The Journal of Physical Chemistry* **1973,** *77* (5), 685-688.
78. (a) Silvestrelli, P. L.; Bernasconi, M.; Parrinello, M., Ab initio infrared spectrum of liquid water. *Chemical Physics Letters* **1997,** *277* (5), 478-482; (b) Silvestrelli, P. L.; Parrinello, M., Water Molecule Dipole in the Gas and in the Liquid Phase. *Physical Review Letters* **1999,** *82* (16), 3308-3311; (c) Tu, Y.; Laaksonen, A., The electronic properties of water molecules in water clusters and liquid water. *Chemical Physics Letters* **2000,** *329* (3–4), 283-288.
79. Badyal, Y. S.; Saboungi, M.-L.; Price, D. L.; Shastri, S. D.; Haeffner, D. R.; Soper, A. K., Electron distribution in water. *The Journal of Chemical Physics* **2000,** *112* (21), 9206-9208.
80. Willow, S. Y.; Salim, M. A.; Kim, K. S.; Hirata, S., Ab initio molecular dynamics of liquid water using embedded-fragment second-order many-body perturbation theory towards its accurate property prediction. *Scientific Reports* **2015,** *5*, 14358.
81. (a) Stone, A. J., *The Theory of Intermolecular Forces*. Oxford University Press: 2002; (b) Kaplan, I. G., *Intermolecular Interactions: Physical Picture, Computational Methods and Model Potentials.* Wiley; (c) Parsegian, V. A., *Van der Waals Forces. A Handbook for Biologists, Chemists, Engineers, and Physicists.* Cambridge University Press; (d) Israelachvili, J. N., *Intermolecular and Surface Froces.* Academic.

82. (a) Silvestrelli, P. L., Van der Waals interactions in density functional theory by combining the quantum harmonic oscillator-model with localized wannier functions. *J. Chem. Phys.* **2013,** *139*, 054106; (b) DiStasio, R. A.; von Lilienfeld, O. A.; Tkatchenko, A., Collective many-body van der Waals interactions in molecular systems. *Proceedings of the National Academy of Sciences* **2012,** *109* (37), 14791-14795; (c) Heßelmann, A., Long-range correlation energies from frequency-dependent weighted exchange-hole dipole polarisabilities. *The Journal of Chemical Physics* **2012,** *136* (1), 014104; (d) Heßelmann, A., Assessment of a Nonlocal Correction Scheme to Semilocal Density Functional Theory Methods. *Journal of Chemical Theory and Computation* **2013,** *9* (1), 273-283; (e) Wu, Q.; Yang, W., Empirical correction to density functional theory for van der Waals interactions. *The Journal of Chemical Physics* **2002,** *116* (2), 515-524; (f) Andrinopoulos, L.; Hine, N. D. M.; Mostofi, A. A., Calculating dispersion interactions using maximally localized Wannier functions. *The Journal of Chemical Physics* **2011,** *135* (15), 154105; (g) Grimme, S., Accurate description of van der Waals complexes by density functional theory including empirical corrections. *Journal of Computational Chemistry* **2004,** *25* (12), 1463-1473; (h) Grimme, S., Semiempirical GGA-type density functional constructed with a long-range dispersion correction. *Journal of Computational Chemistry* **2006,** *27* (15), 1787-1799; (i) Johnson, E. R.; Becke, A. D., A post-Hartree-Fock model of intermolecular interactions: Inclusion of higher-order corrections. *The Journal of Chemical Physics* **2006,** *124* (17), 174104; (j) Tkatchenko, A.; Scheffler, M., Accurate Molecular Van Der Waals Interactions from Ground-State Electron Density and Free-Atom Reference Data. *Physical Review Letters* **2009,** *102* (7), 073005; (k) Sato, T.; Nakai, H., Density functional method including weak interactions: Dispersion coefficients based on the local response approximation. *The Journal of Chemical Physics* **2009,** *131* (22), 224104; (l) Zhao, Y.; Truhlar, D. G., The M06 suite of density functionals for main group thermochemistry, thermochemical kinetics, noncovalent interactions, excited states, and transition elements: two new functionals and systematic testing of four M06-class functionals and 12 other functionals. *Theoretical Chemistry Accounts* **2007,** *120* (1), 215-241; (m) Dion, M.; Rydberg, H.; Schröder, E.; Langreth, D. C.; Lundqvist, B. I., Van der Waals Density Functional for General Geometries. *Physical Review Letters* **2004,** *92* (24), 246401; (n) Lee, K.; Murray, É. D.; Kong, L.; Lundqvist, B. I.; Langreth, D. C., Higher-accuracy van der Waals density functional. *Physical Review B* **2010,** *82* (8), 081101.

83. (a) Andersson, Y.; Langreth, D. C.; Lundqvist, B. I., van der Waals Interactions in Density-Functional Theory. *Physical Review Letters* **1996,** *76* (1), 102-105; (b) Langreth, D. C.; Dion, M.; Rydberg, H.; Schröder, E.; Hyldgaard, P.; Lundqvist, B. I., Van der Waals density functional theory with applications. *International Journal of Quantum Chemistry* **2005,** *101* (5), 599-610.

84. Elstner, M.; Hobza, P.; Frauenheim, T.; Suhai, S.; Kaxiras, E., Hydrogen bonding and stacking interactions of nucleic acid base pairs: A density-functional-theory based treatment. *The Journal of Chemical Physics* **2001,** *114* (12), 5149-5155.

85. Chu, X.; Dalgarno, A., Linear response time-dependent density functional theory for van der Waals coefficients. *The Journal of Chemical Physics* **2004,** *121* (9), 4083-4088.

86. Ferri, N.; DiStasio, R. A.; Ambrosetti, A.; Car, R.; Tkatchenko, A., Electronic Properties of Molecules and Surfaces with a Self-Consistent Interatomic van der Waals Density Functional. *Physical Review Letters* **2015,** *114* (17), 176802.

87. (a) von Lilienfeld, O. A.; Tavernelli, I.; Rothlisberger, U.; Sebastiani, D., Optimization of effective atom centered potentials for london dispersion forces in density functional theory.

Phys Rev Lett **2004,** *93* (15), 153004; (b) Vydrov, O. A.; Van Voorhis, T., Improving the accuracy of the nonlocal van der Waals density functional with minimal empiricism. *The Journal of Chemical Physics* **2009,** *130* (10), 104105.
88. Perdew, J. P.; Burke, K.; Ernzerhof, M., Generalized Gradient Approximation Made Simple. *Physical Review Letters* **1996,** *77* (18), 3865-3868.
89. Perdew, J. P., Density-functional approximation for the correlation energy of the inhomogeneous electron gas. *Physical Review B* **1986,** *33* (12), 8822-8824.
90. Tavernelli, I.; Lin, I. C.; Rothlisberger, U., Multicenter-type corrections to standard DFT exchange and correlation functionals. *Physical Review B* **2009,** *79* (4).
91. Gráfová, L.; Pitoňák, M.; Řezáč, J.; Hobza, P., Comparative Study of Selected Wave Function and Density Functional Methods for Noncovalent Interaction Energy Calculations Using the Extended S22 Data Set. *Journal of Chemical Theory and Computation* **2010,** *6* (8), 2365-2376.
92. Odbadrakh, T. T.; Jordan, K. D., Dispersion dipoles for coupled Drude oscillators. *J Chem Phys* **2016,** *144* (3), 034111.
93. (a) Del Ben, M.; Hutter, J.; VandeVondele, J., Second-Order Moller-Plesset Perturbation Theory in the Condensed Phase: An Efficient and Massively Parallel Gaussian and Plane Waves Approach. *J Chem Theory Comput* **2012,** *8* (11), 4177-88; (b) Lippert, B. G.; Parrinello, J. H.; Michele, A hybrid Gaussian and plane wave density functional scheme. *Molecular Physics* **1997,** *92* (3), 477-488.
94. Boys, S. F.; Bernardi, F., The calculation of small molecular interactions by the differences of separate total energies. Some procedures with reduced errors. *Molecular Physics* **1970,** *19* (4), 553-566.
95. (a) Dunning, T. H., Gaussian basis sets for use in correlated molecular calculations. I. The atoms boron through neon and hydrogen. *The Journal of Chemical Physics* **1989,** *90* (2), 1007-1023; (b) Woon, D. E.; Dunning, T. H., Gaussian basis sets for use in correlated molecular calculations. III. The atoms aluminum through argon. *The Journal of Chemical Physics* **1993,** *98* (2), 1358-1371.
96. Martyna, G. J.; Tuckerman, M. E., A reciprocal space based method for treating long range interactions in ab initio and force-field-based calculations in clusters. *The Journal of Chemical Physics* **1999,** *110* (6), 2810-2821.
97. Williams, H. L.; Chabalowski, C. F., Using Kohn−Sham Orbitals in Symmetry-Adapted Perturbation Theory to Investigate Intermolecular Interactions. *The Journal of Physical Chemistry A* **2001,** *105* (3), 646-659.
98. Shirkov, L.; Makarewicz, J., Does DFT-SAPT method provide spectroscopic accuracy? *The Journal of Chemical Physics* **2015,** *142* (6), 064102.
99. Werner, H. J.; Knowles, P. J.; Knizia, G.; Manby, F. R.; Schütz, M.; others, MOLPRO, version 2015.1, a package of ab initio programs. 2015.
100. Weigend, F., A fully direct RI-HF algorithm: Implementation, optimised auxiliary basis sets, demonstration of accuracy and efficiency. *Physical Chemistry Chemical Physics* **2002,** *4* (18), 4285-4291.
101. Weigend, F.; Köhn, A.; Hättig, C., Efficient use of the correlation consistent basis sets in resolution of the identity MP2 calculations. *The Journal of Chemical Physics* **2002,** *116* (8), 3175-3183.
102. (a) Raghavachari, K.; Trucks, G. W.; Pople, J. A.; Head-Gordon, M., A fifth-order

perturbation comparison of electron correlation theories. *Chemical Physics Letters* **1989,** *157* (6), 479-483; (b) Bartlett, R. J.; Watts, J. D.; Kucharski, S. A.; Noga, J., Non-iterative fifth-order triple and quadruple excitation energy corrections in correlated methods. *Chemical Physics Letters* **1990,** *165* (6), 513-522.
103. (a) Solomon, J.; Chung, P.; Srivastava, D.; Darve, E., Method and advantages of genetic algorithms in parameterization of interatomic potentials: Metal oxides. *Computational Materials Science* **2014,** *81*, 453-465; (b) McCall, J., Genetic algorithms for modelling and optimisation. *Journal of Computational and Applied Mathematics* **2005,** *184* (1), 205-222.
104. Woon, D. E.; Dunning, T. H., Gaussian basis sets for use in correlated molecular calculations. IV. Calculation of static electrical response properties. *The Journal of Chemical Physics* **1994,** *100* (4), 2975-2988.
105. Jiang, H.; Myshakin, E. M.; Jordan, K. D.; Warzinski, R. P., Molecular Dynamics Simulations of the Thermal Conductivity of Methane Hydrate. *The Journal of Physical Chemistry B* **2008,** *112* (33), 10207-10216.
106. (a) Aziz, R. A.; Slaman, M. J., The Ne-Ne interatomic potential revisited. *Chemical Physics* **1989,** *130* (1), 187-194; (b) Aziz, R. A., A highly accurate interatomic potential for argon. *The Journal of Chemical Physics* **1993,** *99* (6), 4518-4525.
107. Feynman, R. P., Forces in Molecules. *Physical Review* **1939,** *56* (4), 340-343.
108. Cernusak, I.; Diercksen, G. H. F.; Sadlej, A. J., Multipole polarizabilities of Ar. *Chemical Physics Letters* **1986,** *128* (1), 18-24.